Double Longitudinal Helicity Asymmetries in Pion Production from Proton Collisions, Studies of Relative Luminosity Determination, and the Impact on Determination of the Gluon Spin in the Proton

A Dissertation Presented

by

Andrew Manion

to

The Graduate School

in Partial Fulfillment of the Requirements

for the Degree of

Doctor of Philosophy

in

Physics

Stony Brook University

May 2014

Stony Brook University

The Graduate School

Andrew Manion

We, the dissertation committee for the above candidate for the Doctor of Philosophy degree, hereby recommend acceptance of this dissertation.

Abhay Deshpande – Dissertation Advisor
Professor, Department of Physics and Astronomy

George Sterman – Chairperson of Defense
Professor, Department of Physics and Astronomy

Eden Figueroa
Professor, Department of Physics and Astronomy

Kieran Boyle
Experimental Research Fellow
RIKEN BNL Research Center

Xiaorong Wang
Professor
New Mexico State University

This dissertation is accepted by the Graduate School.

Charles Taber
Dean of the Graduate School

Abstract of the Dissertation

Double Longitudinal Helicity Asymmetries in Pion Production from Proton Collisions, Studies of Relative Luminosity Determination, and the Impact on Determination of the Gluon Spin in the Proton

by

Andrew Manion

Doctor of Philosophy

in

Physics

Stony Brook University

2014

Abhay Deshpande

Polarized proton-proton collisions at RHIC are being used to study the origin of proton spin, which arises from the spin and orbital angular momentum of its constituent quarks and gluons. Measurements at the PHENIX experiment at $\sqrt{s} = 200$ GeV of $A_{LL}^{\pi^0}$, the double longitudinal helicity asymmetry in neutral pion production, are used in global analyses of world polarized scattering data, where they are particularly important in constraining the sector of gluon polarization. These measurements have ruled out maximal gluonic spin contributions and are consistent with a small or zero contribution. In the latest measurements, the statistical precision of the data has reached the systematic limit, prompting investigation into the largest of the systematic uncertainties, the

determination of relative luminosity. Details of the 2009 measurement at PHENIX of $A_{LL}^{\pi^0}$ and its inclusion in the global analysis will be presented along with recent studies on systematic uncertainties, including a 2012 study that varied the angles of the beams in the PHENIX interaction region.

Contents

List of Figures

List of Tables

Acknowledgements

Thanks is due to all of my colleagues, especially to Kieran Boyle for always prodding me to cross every frustrating f and dot every jading j, and for helping me when it was too much. Thanks also to my advisor, Abhay Deshpande for providing security and support, and for lending his authority when needed. Thanks to Paul Kline for sharing the graduate school experience with me and listening to my inane frustrations. I also owe a lot to my excellent family, including my son Zen, who is my complete opposite in many ways and helps bring me out of my shell, and my wife Stephanie, who shows me that she cares about me every day and spent many nights doing my share of the chores when she could tell I was busy.

Chapter 1

Introduction to Spin Structure

Under the valence quark model used to classify hadrons and determine their quantum numbers, the proton is composed of two up quarks and one down quark. This arrangement could also easily explain the half-integer proton spin. A more thoughtful accounting called the naive quark model [33] assumed that due to relativistic effects [56] it was instead the total angular momentum of the quarks that gave rise to the proton spin. In other words, the spin of the proton could be expressed as the total angular momentum of the quarks

$$S_p = \frac{1}{2} = \frac{1}{2}\Delta\Sigma + L_q, \tag{1.1}$$

where $\Delta\Sigma$ is the quark spin contribution and L_q the contribution from the quark orbital angular momentum. In this model, the expectation for $\Delta\Sigma$ was 0.6. However, early experiments sensitive to only the quark content in the proton, such as that by the European Muon Collaboration with the result in Fig. 1.1, showed that the quark spin fell short of 0.6 and in fact the picture was more complicated.

In the more complicated picture, the total proton spin can be classified in terms of quark and gluon spin ($\Delta\Sigma$ and ΔG, respectively) and angular momentum (L_q and L_g, respectively) contributions as

$$S_p = \frac{1}{2} = \frac{1}{2}\Delta\Sigma + \Delta G + L_q + L_g, \tag{1.2}$$

according to the Manohar-Jaffe sum rule[42]. Several more recent global fits [21, 27, 40, 47] of Deeply-Inelastic Scattering (DIS) data have confirmed that the quark spin contribution, $\Delta\Sigma$, falls short of the total, yielding 25-35% of the proton spin depending on the assumptions used (for instance, whether SU(3) symmetry is enforced).

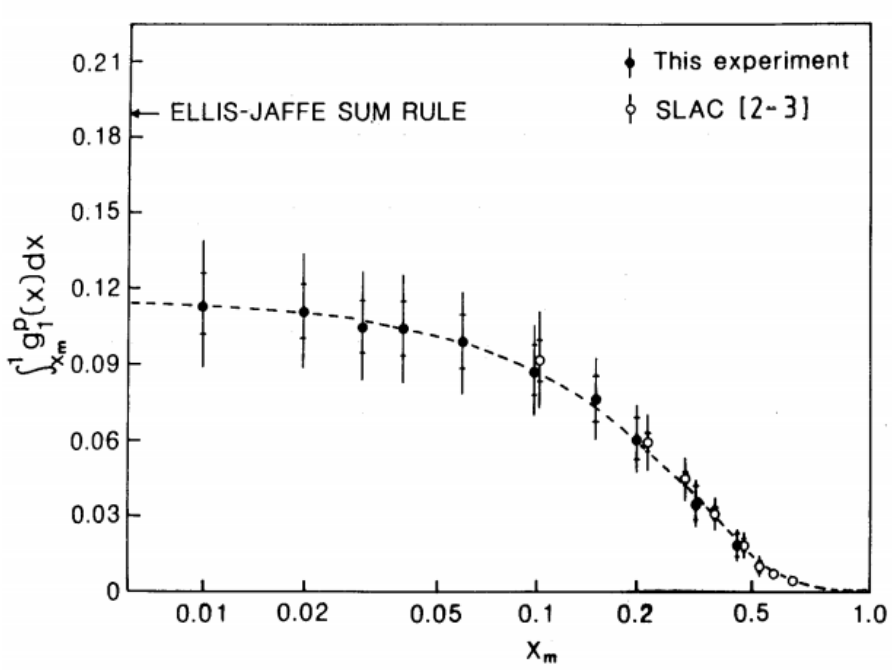

Figure 1.1: Integral of the polarized structure function g_1^p for the proton (see Subsection 1.2.1), which falls short of the expected value if $\Delta\Sigma = 0.6$.

Polarized proton collisions at the Relativistic Heavy Ion Collider (RHIC) at Brookhaven National Laboratory allow access to ΔG through processes directly involving gluons in the context of spin (unlike lepton-hadron scattering experiments which are only sensitive to the gluon via scaling violations and photon-gluon fusion). Recent theoretical work is also proceeding to understand the orbital angular momentum contributions and how they can be measured [39, 46]. The determination of ΔG via global analysis of these data prior to the data presented herein can best be summarized by the result of the 2008 DSSV global analysis. That determination of ΔG is shown in Fig. 1.2, which determined the integral $\Delta G^{[0.05,0.2]}_{\mathrm{DSSV08}} = 0.005^{+0.129}_{-0.164}$ in the Bjorken-x range $[0.05, 0.2]$.

In this thesis, we will discuss the access of ΔG through polarized proton-proton scattering producing a final state neutral pion, including the addition of new data from the PHENIX experiment. There are significant experimental challenges in measurements of proton-proton collisions, chief among them the determination of the luminosity in different collisions, or relative luminosity. Therefore, there will also be significant discussion of and studies into the

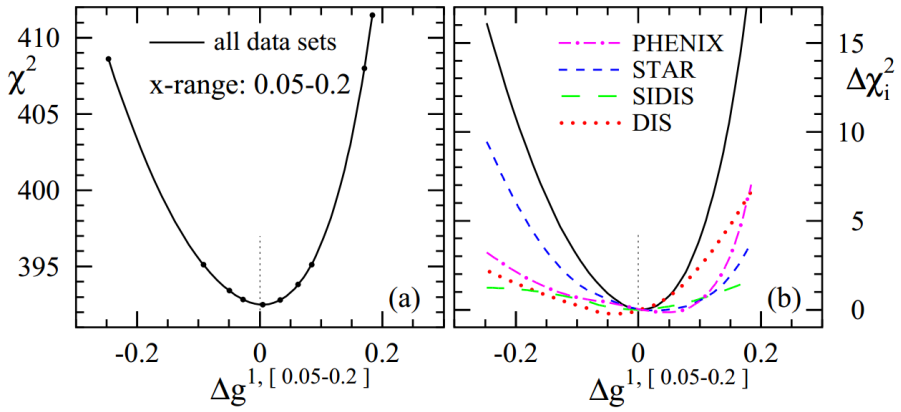

Figure 1.2: 2008 DSSV global analysis determination of the gluon polarization in a limited Bjorken-x range (see Subsection 1.2.1).

systematic uncertainty on relative luminosity.

1.1 Spin Asymmetries Illustrated

Cross-sectional spin asymmetries, whether measured for interactions of fundamental particles or for collections of fundamental particles, are important quantities for accessing spin information experimentally. As a brief introduction, several of these asymmetries are illustrated here in Figs. 1.3 and 1.4.

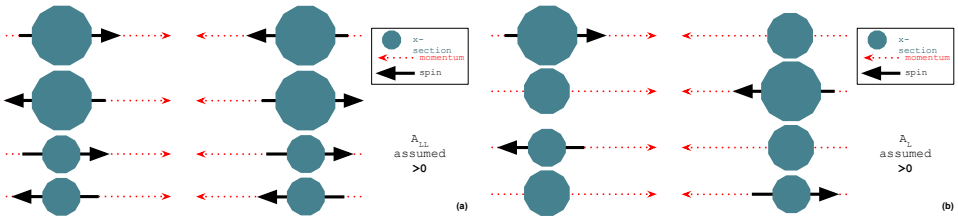

Figure 1.3: Illustration of (a) interactions giving rise to a positive double-spin asymmetry A_{LL}, and (b) interactions giving rise to a positive single-spin asymmetry A_L.

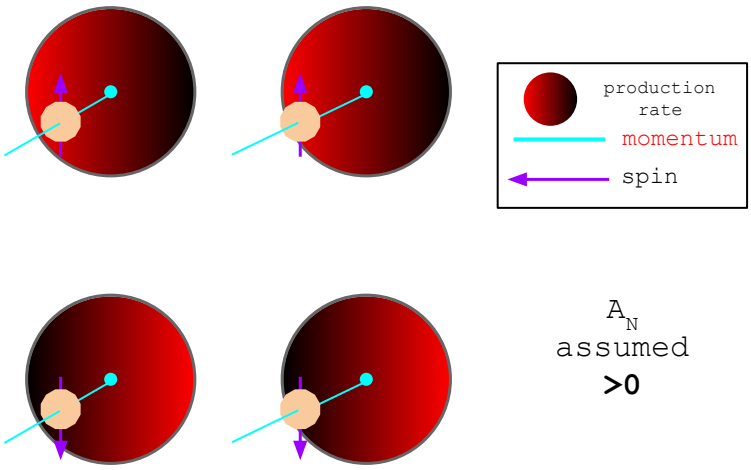

Figure 1.4: Stereoscopic (cross-eyed) illustration of azimuthal asymmetry in forward particle production, or A_N.

1.2 (Polarized) Deeply Inelastic Scattering

Deeply inelastic scattering is the last stage in increasingly fine position and time resolution of nucleon structure via electromagnetic scattering with a lepton. The degree of resolution is approximately determined by the invariant magnitude of the momentum transfer $|\mathbf{q}|$ and the energy transfer ν:

$$\begin{aligned} \Delta x &\sim \frac{\hbar}{|\mathbf{q}|}, \\ \Delta t &\sim \frac{\hbar}{\nu}. \end{aligned} \tag{1.3}$$

With $\nu \approx 0$ and sufficient $|q|$, elastic lepton-nucleon scattering, as in Fig. 1.5, can be used to probe the charge radius of the proton, which is approximately exponentially distributed with a standard deviation 0.88 ± 0.01 fm (although recent muonic hydrogen spectroscopy has given a surprisingly different answer [14]). As $|\mathbf{q}|c$ is increased to order 1 GeV, and, more importantly, ν is on order

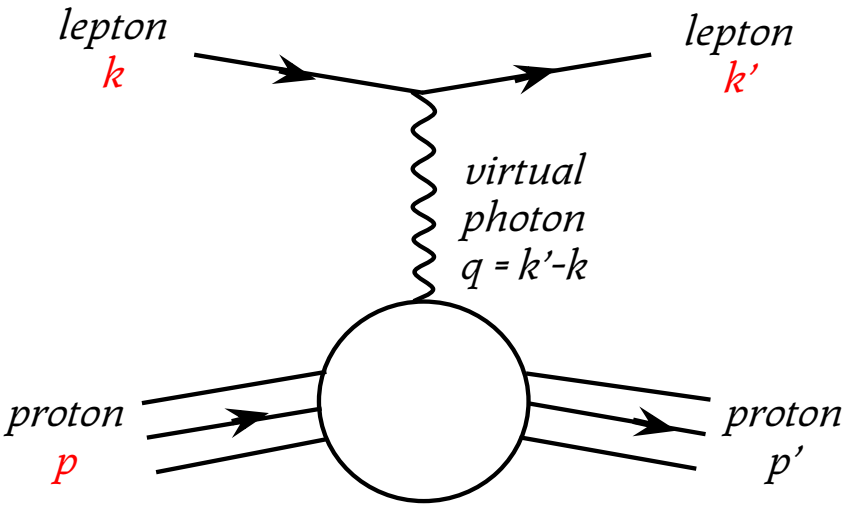

Figure 1.5: Feynman diagram showing the one photon exchange contribution to elastic scattering of a lepton with a proton.

of 100 MeV, nuclear resonances can be excited via inelastic scattering, such as the Δ^+ state as shown in Fig. 1.6. This is the regime of nuclear spectroscopy, and such excitations quickly decay to produce baryons and mesons in what is known as "electroproduction." The existence of such states indicates that nucleons are made up of distinct constituents interacting via some force very

much stronger than the electromagnetic force. When $|q|c$ and ν both exceed

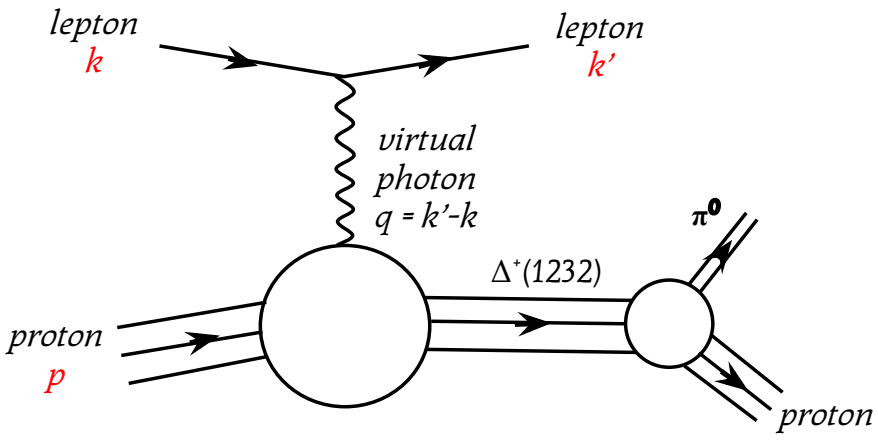

Figure 1.6: Feynman diagram showing the one photon exchange contribution to scattering of a lepton with a proton that produces a resonant $\Delta^+(1232)$ state, which is unstable and will decay, for example, to a proton and a π^0. The entire process is referred to as "meson electroproduction."

$\sim$ 1 GeV, the regime of deeply inelastic scattering is reached, and the substructure of the nucleon is finally resolved. At sufficiently fine position and time resolution, nucleons appear to the lepton as a collection of free quarks, from which the lepton elastically scatters (Fig. 1.7). In the proton rest frame, neglecting the mass of the electron, the differential cross-section for deeply inelastic scattering is given as a function of scattering angle in terms of "proton structure functions" $W_{1,2}$,

$$\frac{d^2\sigma}{dQ^2 d\nu} = \frac{\pi\alpha^2}{4k^2\sin^4(\theta/2)}\frac{1}{kk'}\left[W_2\cos^2(\theta/2) + 2W_1\sin^2(\theta/2)\right] \tag{1.4}$$

with k and k' the initial and final energy of the scattered electron ($k^0 - k'0 \equiv \nu$), and $Q^2 = -q^2$. In the following section we will see how these structure functions can be understood in terms of the simple elastic electron-quark scattering.

1.2.1 Bjorken-x and PDFs

Figure 1.8 depicts to first order the Quantum Electrodynamics (QED) process of elastic scattering between a lepton and a quark. Supposing the quark carries

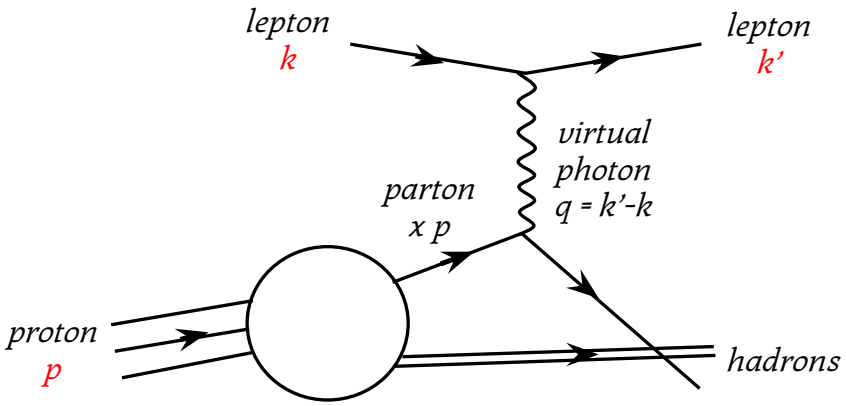

Figure 1.7: Feynman diagram showing the one photon exchange contribution to deeply inelastic scattering of a lepton with a proton, which is actually elastic scattering with a quark contained within the proton.

three momentum $x\mathbf{p}$ and has mass xM (where M is for now just an unidentified constant), and that the quark is free (on shell) before and after the elastic scattering, we have that

$$(x\mathbf{p})^2 = (x\mathbf{p} + \mathbf{q})^2 = (xM)^2, \tag{1.5}$$

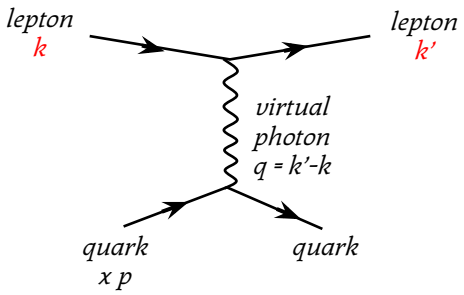

Figure 1.8: Feynman diagram for single photon exchange in elastic lepton quark scattering.

where $\mathbf{q}$ is the four-momentum transfer. Taking the latter equality and expanding the square gives

$$\begin{aligned} (xM)^2 &= (x\mathbf{p})^2 + \mathbf{q}^2 + 2x\mathbf{p}\cdot\mathbf{q} \\ (xM)^2 &= (xM)^2 + \mathbf{q}^2 + 2x\mathbf{p}\cdot\mathbf{q} \\ -\mathbf{q}^2 &= 2x\mathbf{p}\cdot\mathbf{q}. \end{aligned} \tag{1.6}$$

$-\mathbf{q}^2$ is usually redefined as Q^2 to remove the minus sign. Switching to the proton rest frame, we can evaluate the invariant $2x\mathbf{p}\cdot\mathbf{q}$:

$$2x\mathbf{p}\cdot\mathbf{q} = 2xM(k^0 - k'^0) \equiv 2xM\nu. \tag{1.7}$$

Using this with the previous equation, we can solve for x

$$x = \frac{Q^2}{2M\nu} \tag{1.8}$$

This quantity is referred to as "Bjorken x," and is interpreted as the fraction of a proton's momentum $\mathbf{p}$ a free quark within the proton carries. It can then be shown [36] that M is to leading order equal to the proton mass.

Elastic scattering of an lepton with an individual quark of index i in the quark rest frame, neglecting the lepton mass, is given by

$$\frac{d^2\sigma^i}{dQ^2 d\nu} = \frac{\pi\alpha^2}{4k^2\sin^4(\theta/2)}\frac{1}{kk'}\left[e_i^2\cos^2(\theta/2) + e_i^2\frac{Q^2}{4m_i^2}2\sin^2(\theta/2)\right] \times \delta(\nu - Q^2/2m_i), \tag{1.9}$$

where e_i, m_i are the charge and mass of the quark and the delta function enforces the elastic scattering condition $\nu = Q^2/2m_i$. To relate this to the proton structure functions $W_{1,2}$, we must integrate this distribution over the probability $q_i(x)$ to find quark i in the proton with momentum fraction x, called a "parton distribution function" or PDF, and then sum over quark flavors. This results in the relations

$$\begin{aligned} W_2 &= \frac{1}{\nu}\sum_i e_i^2 x q_i(x) \\ W_1 &= \frac{1}{2M}\sum_i e_i^2 q_i(x). \end{aligned} \tag{1.10}$$

These structure functions are often expressed in an alternate version

$$\begin{aligned} F_2 = \nu W_2 &= \sum_i e_i^2 x q_i(x) \\ F_1 = M W_1 &= \frac{1}{2M} \sum_i e_i^2 q_i(x). \end{aligned} \tag{1.11}$$

Measurements of these structure functions allow the extraction of PDFs, such as in Fig. 1.9. Also determined in the extractions is the PDF for gluons, $g(x)$, which can for example be accessed through scaling violations (see Section 1.3.3) and $p + \bar{p}$ scattering.

There are also analogous structure functions in polarized DIS, referred to as g_1 and g_2. There forms are similar to the Fs. For instance,

$$g_1 = \sum_i e_i^2 \Delta q_i(x), \tag{1.12}$$

where Δ denotes a difference between quark polarization with respect to the nucleon spin, referred to as a "polarized parton distribution function," or pPDF. The quark polarization terms in g_1 can be accessed experimentally via production asymmetries, for example the asymmetry in longitudinally polarized lepton scattering on a longitudinally polarized nucleon target

$$A = \frac{d\sigma^{+-} - d\sigma^{++}}{d\sigma^{+-} + d\sigma^{++}}, \tag{1.13}$$

which is differential in the rapidity (η) of the scattered lepton. This asymmetry can be expressed in terms of two virtual photon asymmetries as [16]

$$A = D(A_1 + \eta A_2), \tag{1.14}$$

where D is a depolarization factor for the virtual photon and can be calculated from the kinematics of the interaction and the known ratio of longitudinal to transverse photoabsorption cross sections. If η is sufficiently small in the kinematic range of the experiment, A becomes essentially proportional to A_1, which is the asymmetry between cross-sections for virtual photoabsorption with respect to the total angular momentum of the virtual photon-nucleon system along the incident lepton direction:

$$A_1 = \frac{\sigma_{1/2} - \sigma_{3/2}}{\sigma_{1/2} - \sigma_{3/2}}. \tag{1.15}$$

A_1 can be expressed in terms of the polarized and unpolarized structure func-

tions as

$$A_1 = \frac{g_1 - \left(\frac{2Mx}{\nu}\right) g_2}{F_1}, \tag{1.16}$$

where M is the nucleon mass. With high enough energy transfer ν, A_1 becomes

$$A_1 \approx \frac{g_1}{F_1} = \frac{\sum_i e_i \Delta q_i(x)}{\sum_i e_i q_i(x)} \tag{1.17}$$

Thus measurement of A and knowledge of D allows the extraction of the sum of quark pPDFs relative to the sum of PDFs. If some particle is tagged in the final state in what is referred to as semi-inclusive DIS, or SIDIS, the weighting over and sensitivity to different flavors in the sum can be changed. pPDFs can be extracted from global analyses to such scattering data, including the corresponding pPDF for gluons, $\Delta g(x)$. One such pPDF extraction is shown in Fig. 1.10.

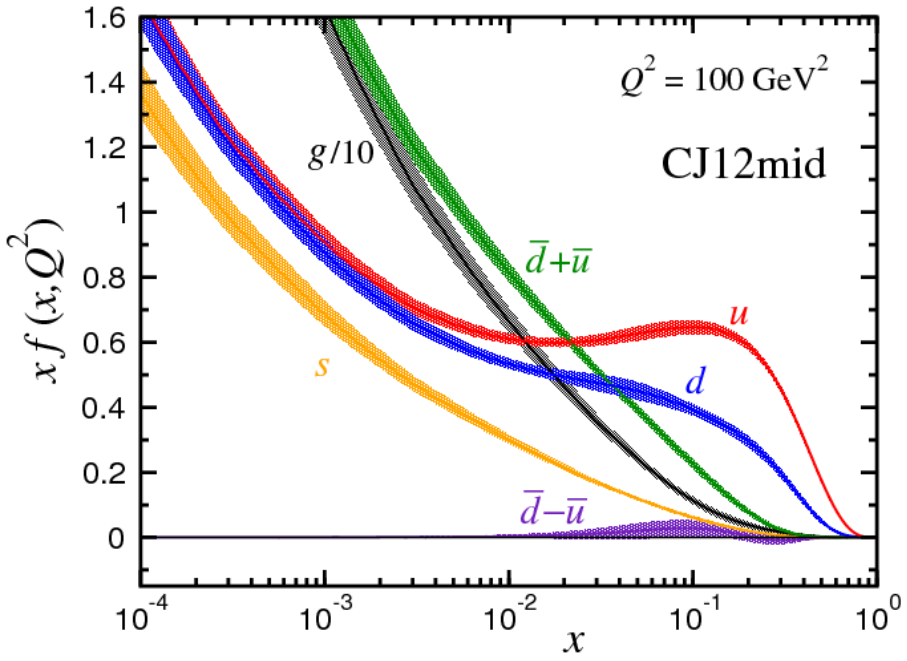

Figure 1.9: From [52]. Parton distribution functions determined from a global analysis of DIS and $p + \bar{p}$ scattering data.

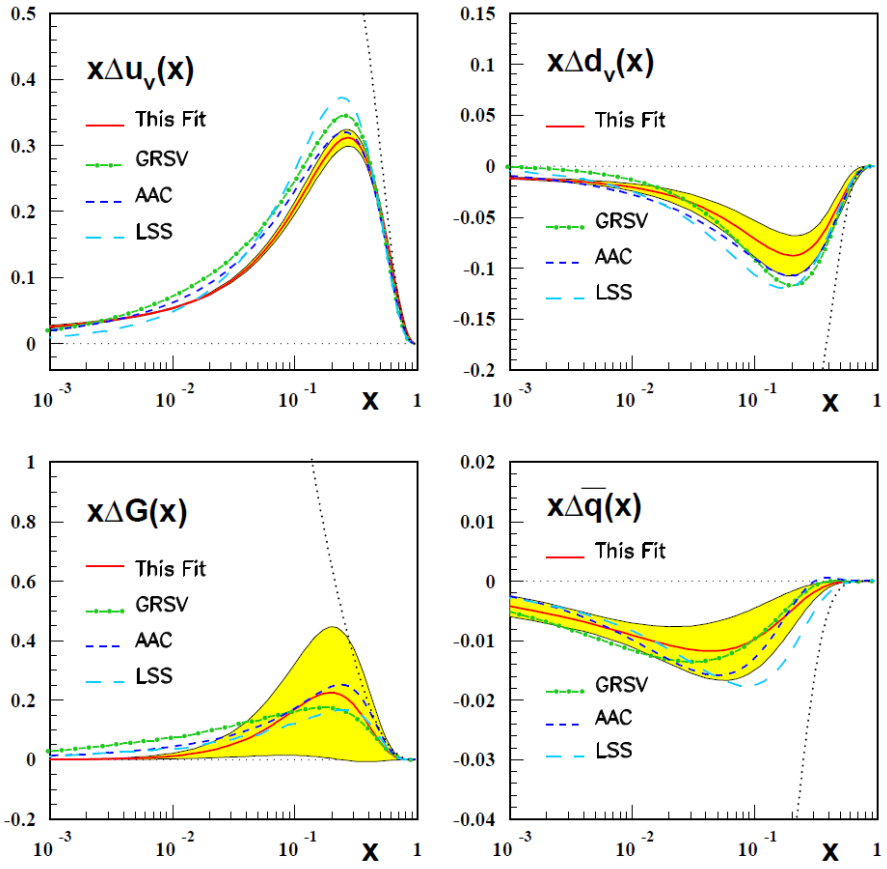

Figure 1.10: From [21]. "This Fit" refers to the BB2010 result from the reference. Polarized parton distribution functions for u-valence quarks, d-valence quarks, gluons and anti-quarks determined from a global analysis of DIS scattering data. The yellow shaded bands are the 1σ uncertainty.

1.3 (Polarized) Proton+Proton Scattering

1.3.1 Asymptotic Freedom and pQCD

The theory of quantum chromodynamics, or QCD, explains the strong force, mediated by gluons, between color charged objects called quarks and, unlike in QED, even between the force mediating gluons themselves. This force confines quarks into inseparable color neutral bound states, and is too strong to be handled with a perturbative approach, unless we probe the bound state at sufficiently high energy and momentum transfer, as in DIS. At these high energies and correspondingly short distances is where asymptotic freedom takes over, and the strong force becomes weak enough to treat with perturbative calculations. Given the strength of the strong force at some scale μ^2, the strength of the strong force at a given Q^2 can be found to first order from the equation

$$\alpha_S(Q^2) = \frac{\alpha_S(\mu^2)}{1 + \alpha_S(\mu^2) b \ln(Q^2/\mu^2)},\ b = \frac{33 - 2N_f}{12\pi} \tag{1.18}$$

which describes the "running" of the strong coupling constant, connecting it between different values of momentum transfer. N_f is the number of active (above threshold) quark flavors. Any $N_f \leq 16$ makes b positive, and as there are only 6 total flavors of quarks in QCD, $\alpha_S(Q^2)$ will decrease with increasing Q^2, as opposed to QED where b is negative. The qualitative reason for this is that while, like electron-positron vacuum pair screening in QED, QCD has screening from quark-antiquark vacuum pairs, QCD also has colored gluons, which produce an antiscreening effect that wins out for $N_f \leq 16$.

1.3.2 Factorization

To make the connection between the parton-level theoretical predictions of pQCD and experimental results for scattering with an extended collection of partons, a scheme called "factorization" is used. In pQCD factorization, partonic cross-sections are convoluted with PDFs. In this way, scattering with a nucleon is treated as a statistical average over scattering with individual partons distributed within that nucleon. For example, the total $p + p$ cross-section can be written as

$$\sigma^{p+p} = \sum_{ab} f_a(\theta_{\mathbf{1}}, \mu_F^2) \otimes f_b(\theta_{\mathbf{2}}, \mu_F^2) \otimes \sigma^{a+b}(\theta_{\mathbf{1}}, \theta_{\mathbf{2}}, \mu_F^2, \mu_R^2), \tag{1.19}$$

where f_a and f_b are the PDFs for parton types a and b in protons 1 and 2, $\theta_{\mathbf{1}}$ and $\theta_{\mathbf{2}}$ describe the kinematics of these partons, and σ^{a+b} is the partonic

cross-section for $a + b$. μ_F^2 is the initial factorization energy scale, and μ_R^2 is the renormalization energy scale of the pQCD calculation.

If a specific final state hadron is probed in the interaction, a final state parton may need to be specified in the parton-level pQCD cross-section, in which case another phenomenological function, called a "fragmentation function" needs to be added to describe the probability for the final state parton to "fragment" into the specified final state hadron. With this addition, the equation for factorization becomes

$$\sigma^{p+p\to h+X} = \sum_{abc} f_a(\theta_{\mathbf{1}}, \mu_F^2) \otimes f_b(\theta_{\mathbf{2}}, \mu_F^2) \otimes \sigma^{a+b\to c+X}(\theta_{\mathbf{1}}, \theta_{\mathbf{2}}, \theta_{\mathbf{3}}, \mu_F^2, \mu_R^2, \mu_{FF}^2) \otimes D_c^h(\theta_{\mathbf{3}}, \theta_{\mathbf{h}}, \mu_{FF}^2). \tag{1.20}$$

A kinematic term for the final state parton c has been added ($\theta_{\mathbf{3}}$), as well as one for the final state hadron h ($\theta_{\mathbf{h}}$). The fragmentation function D_c^h describes the probability for the parton c to fragment into hadron h, and depends on an additional energy scale μ_{FF}^2.

In order to test the applicability of factorization to our A_{LL} results, PHENIX has previously published π^0 cross sections [2, 5]. These cross sections, along with others at $\sqrt{s} = 200$ GeV for η mesons, jets [1] and direct photons [10], are well described by the theory within its uncertainties, based on the method of varying the choice of scales by a factor of two. In the publication [4], the impact of this theoretical scale uncertainty with respect to PHENIX $A_{LL}^{\pi^0}$ results is examined, with the conclusion that it is important and should be considered in future global analyses.

Factorization can also be applied to polarized scattering. In that case, a difference in helicity dependent cross-sections, $\Delta\sigma^{p+p\to h+X}$, would be factorize as

$$\Delta\sigma^{p+p\to h+X} = \sum_{abc} \Delta f_a(\theta_{\mathbf{1}}, \mu_F^2) \otimes \Delta f_b(\theta_{\mathbf{2}}, \mu_F^2) \otimes \Delta\sigma^{a+b\to c+X}(\theta_{\mathbf{1}}, \theta_{\mathbf{2}}, \theta_{\mathbf{3}}, \mu_F^2, \mu_R^2, \mu_{FF}^2) \otimes D_c^h(\theta_{\mathbf{3}}, \theta_{\mathbf{h}}, \mu_{FF}^2), \tag{1.21}$$

where we now have differences in helicity dependent PDFs and helicity dependent cross-sections, the latter still calculable in pQCD. In some cases spin may also need to be taken into account in the fragmentation function, but not in cases where the fragmentation is to a spin-0 state, as in the case of neutral pion production.

1.3.3 QCD Evolution

An important effect needs to be included in the electron-parton scattering of DIS or the parton-parton scattering term of $p + p$ factorization. That effect

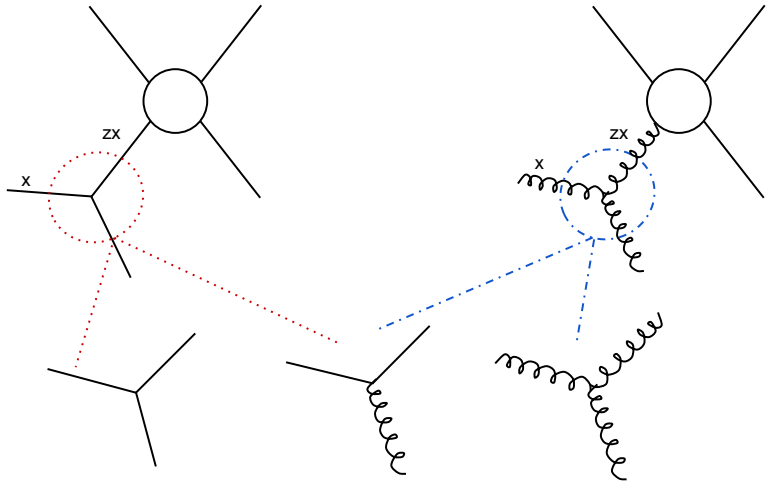

Figure 1.11: Example Feynman diagrams of quark-quark and quark-gluon scattering (the specific interaction is hidden in the blank circle), along with the pieces for collinear radiation that can be substituted in (with appropriate rotation).

is the splitting of the initial state partons into collinear parton pairs that cannot be experimentally distinguished from a single particle. Examples of such "collinear emission" are shown at lowest order in Fig. 1.11. Since we are only interested in the condition in which this extra vertex produces a collinear particle, we attach for each vertex a factor of $\alpha_S ln(Q^2/\mu^2)$, where μ is the momentum scale at which nonperturbative effects are factorized. In practice, this contribution is absorbed into the parton distribution functions instead of being attached to the electron-parton or parton-parton scattering term. With this choice, the extra collinear emission terms act as a kernel for PDF evolution in what are known as the DGLAP (Dokshitzer-Gribov-Lipatov-Altarelli-Parisi) equations:

$$\begin{aligned}
\frac{d}{d\log Q} g(x,Q) &= \frac{\alpha_S(Q^2)}{\pi} \int_z^1 \frac{dz}{z} \left(P_{gq}(z) \sum_f [q(\frac{x}{z},Q) + \bar{q}(\frac{x}{z},Q)] + P_{gg}(z) g(\frac{x}{z},Q) \right) \\
\frac{d}{d\log Q} q(x,Q) &= \frac{\alpha_S(Q^2)}{\pi} \int_z^1 \frac{dz}{z} \left(P_{qq}(z) q(\frac{x}{z},Q) + P_{qg}(z) g(\frac{x}{z},Q) \right) \\
\frac{d}{d\log Q} \bar{q} &= \frac{\alpha_S(Q^2)}{\pi} \int_z^1 \frac{dz}{z} \left(P_{qq}(z) \bar{q}(\frac{x}{z},Q) + P_{qg}(z) g(\frac{x}{z},Q) \right)
\end{aligned} \tag{1.22}$$

$$
\begin{aligned}
P_{qq}(z) &= \frac{4}{3}\left(\frac{1+z^2}{(1-z)_+} + \frac{3}{2}\delta(1-z)\right), \\
P_{gq}(z) &= \frac{4}{3}\left(\frac{1+(1-z)^2}{z}\right), \\
P_{qg}(z) &= \frac{1}{2}\left(z^2+(1-z)^2\right), \text{ and} \\
P_{gg}(z) &= 6\left(\frac{(1-z)}{z} + \frac{z}{(1-z)_+} + z(1-z) + \left(\frac{11}{12} - \frac{n_f}{18}\right)\delta(1-z)\right)
\end{aligned} \tag{1.23}
$$

where n_f is the number of flavors and $\frac{1}{(1-z)_+}$ is defined such that

$$
\int_0^1 dz \frac{f(z)}{(1-z)_+} \equiv \int_0^1 dz \frac{f(z)-f(1)}{(1-z)} \tag{1.24}
$$

This evolution also applies to the polarized PDFs. One of the consequences of these evolution equations is that ΔG, which cannot be accessed at leading order in DIS, can be extracted via comparing quark PDFs at different scales.

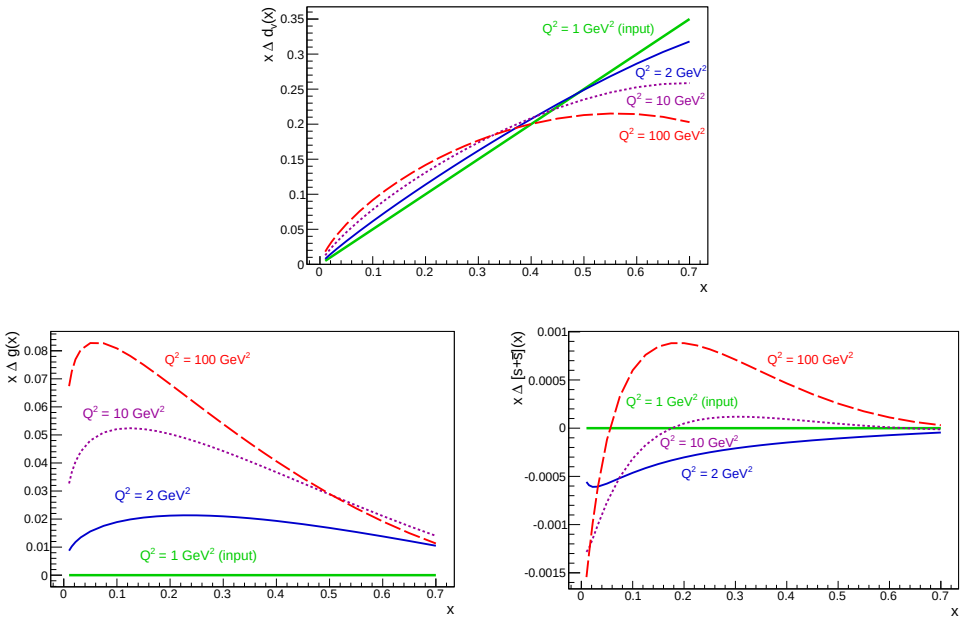

Figure 1.12: Example evolution starting at a scale of 1 GeV^2 with the proton spin entirely due to the down valence quark (i.e. $d_v(x) = \frac{1}{2}$. The effects on the down valence distribution (d_v) are shown as well as those on the gluon ($g(x)$) and strange quark ($[s+\bar{s}](x)$) distributions.

1.3.4 Fragmentation Functions

Final state partons in a DIS or pQCD interaction are not colorless, and so cannot exist unconfined. They instead fragment into hadrons, and this process can be phenomenologically described using "fragmentation functions," which are similar to the parton distribution functions used to describe the probability to find a certain parton within a hadron. A fragmentation function $D_c^h(z, \mu_{FF}^2)$ describes the probability for parton c to fragment into a hadron or hadrons including hadron h, where hadron h carries fraction z of parton c's momentum. μ_{FF}^2 is the fragmentation scale. One way to extract fragmentation functions is through e^+e^- scattering to hadrons, as in Fig. 1.13, although this does not allow quark and antiquark fragmentation functions to be distinguished due to there being both a quark and its anti-quark in the pre-fragmentation final state. A more complete analysis of e^+e^- annihilation, DIS, SIDIS and $p+p$ scattering

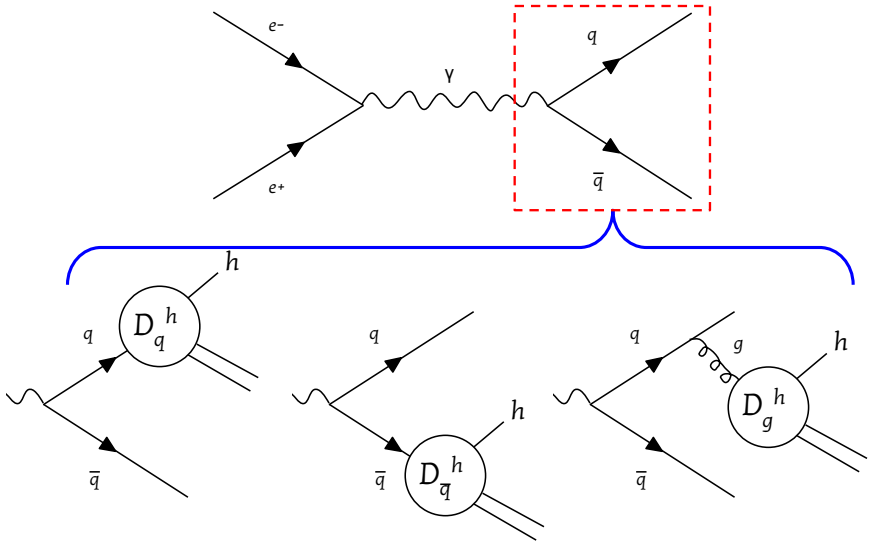

Figure 1.13: Examples of the role of fragmentation functions in the production of hadrons in electron-positron annihilation.

by DSS [28] allows better separation of the fragmentation functions, including those for identified pions, such as with the π^+ fragmentation functions in Fig. 1.14. As with PDFs, fragmentation functions are defined so as to absorb final state collinear singularities, and so they also have evolution equations, outlined in [28].

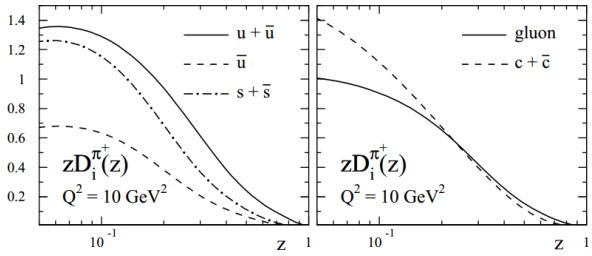

Figure 1.14: From [28]. Fragmentation functions for different partons into a final state containing a π^+.

1.3.5 From $A_{LL}^{\pi^0}$ to ΔG

Ultimately, we want to use measurements of A_{LL} to extract polarized PDFs for the proton. To that end, we note that the asymmetry in production of a final state hadron h, is just

$$A_{LL}^{h} \equiv \frac{\Delta\sigma^{p+p\to h+X}}{\sigma^{p+p\to h+X}}. \tag{1.25}$$

Thus, by including fragmentation function measurements and pQCD calculations of partonic cross-sections, we will be able to extract from our measurements of various A_{LL}^{h} polarized PDFs such as $\Delta g(x, \mu_F^2)$.

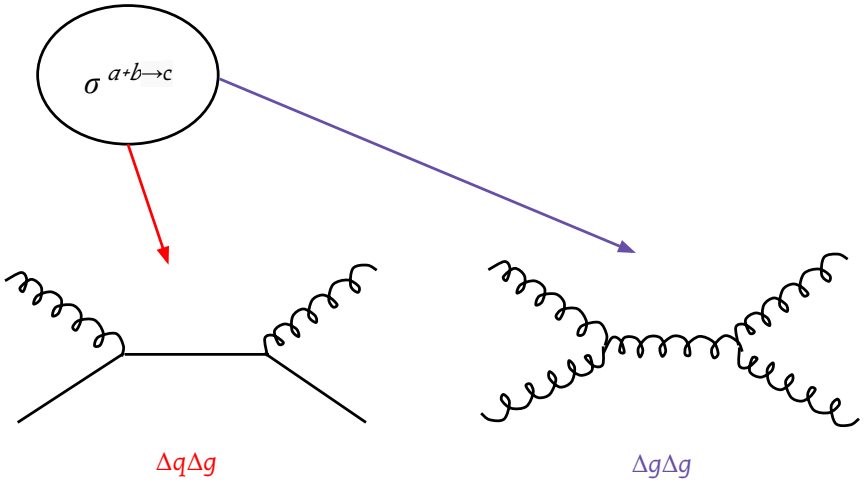

Figure 1.15: Leading order contributions to the partonic scattering term in factorization for neutral pion production.

Figure 1.15 shows the leading order contributions to the partonic cross section term ($\sigma^{a+b\to c+X}$) in the factorization expression for neutral pion production. Thus, to leading order, we should expect $A_{LL}^{\pi^0}$ to behave as the linear combination

$$A_{LL}^{\pi^0} \sim c_{qg}\Delta g\Delta q\frac{\Delta\sigma^{g+q\to g+q}}{\sigma^{g+q\to g+q}} + c_{qq}\Delta q\Delta q\frac{\Delta\sigma^{q+q\to q+q}}{\sigma^{q+q\to q+q}}. \tag{1.26}$$

The partonic helicity asymmetry terms like $\frac{\Delta\sigma^{q+q\to+q}}{\sigma^{q+q\to+q}}$ are calculable in pQCD and are shown in Fig. 1.16. Figure 1.17 also shows the gluon Bjorken-x range sampled by inclusive π^0 measurements at a given p_T.

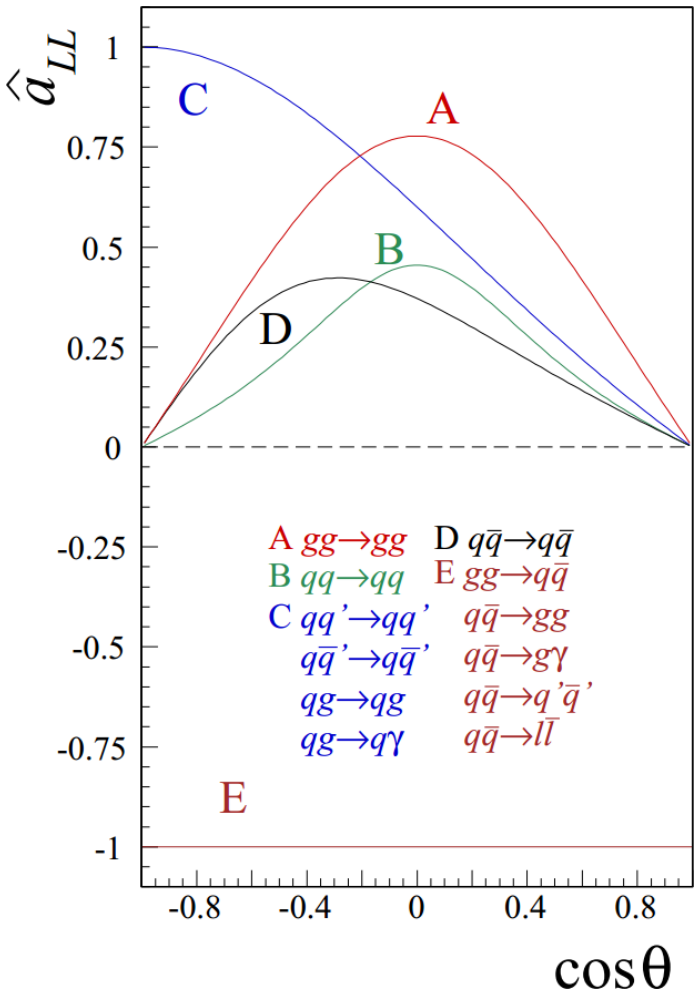

Figure 1.16: From [22]. Partonic double longitudinal helicity asymmetries as a function of partonic center-of-mass scattering angle.

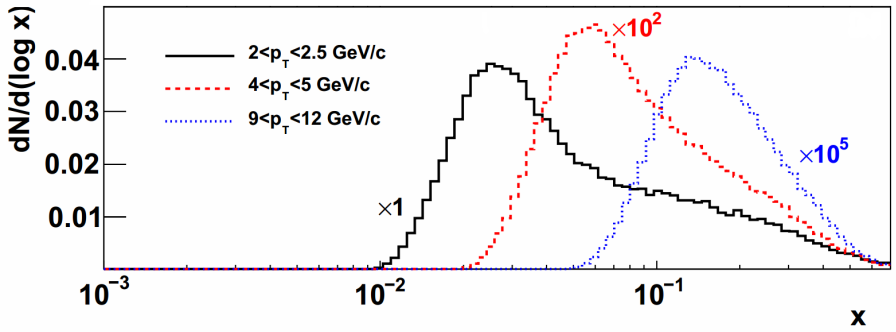

Figure 1.17: From [4]. Distribution of gluon Bjorken-x sampled in three π^0 p_T bins for the process $p + p \to \pi^0 + X$ at $\sqrt{s} = 200$ GeV, calculated to NLO in pQCD.

Chapter 2

Experiment

In this chapter the facility and detectors used to measure $A_{LL}^{\pi^0}$ will be introduced. This includes the Relativistic Heavy Ion collider, RHIC, which provides collisions of polarized protons at up to 6 interaction points, one of which houses the PHENIX experiment.

2.1 RHIC

RHIC consists of two intersecting storage ring synchrotrons, designated Blue and Yellow, in each of which as many as 120 polarized proton bunches can be accelerated to an energy of 255 GeV per proton. In the 2009 run, RHIC was typically operated with 109 out of 120 bunches filled in each ring. The rings intersect in 6 locations such that the bunches collide with a one-to-one correspondence. This allows an unambiguous definition of 120 "crossings" per revolution at each experiment, with a 106 ns separation. At PHENIX, there were 107 crossings in which both bunches were filled, as well as 4 crossings with only the bunch in one ring filled to enable estimates of beam background.

The stable polarization direction in RHIC is vertical. The polarization for each bunch can be aligned or anti-aligned with this vertical axis at injection, allowing for variation over all four possible polarization combinations within 4 crossings, or 424 ns. To reduce false asymmetries related to coupling between the polarization patterns and the bunch/crossing structure, four different polarization vs. bunch patterns, hereafter refered to as "spin patterns," were used, defined by flipping all polarizations in one or both beams in the base pattern. The patterns were cycled after each successful beam store, or "fill".

The beam polarization was measured several times per fill using a fast relative polarimeter which detects elastic scattering off of a thin carbon target that is moved across the beam. This polarimeter can determine both the

amplitude of the polarization and any variation across the width of the beam (see 2.1.3). In order to normalize this relative measurement, the absolute polarization is measured over the entire running period via scattering of the beam with a continuously-running polarized gas-jet target (see 2.1.3).

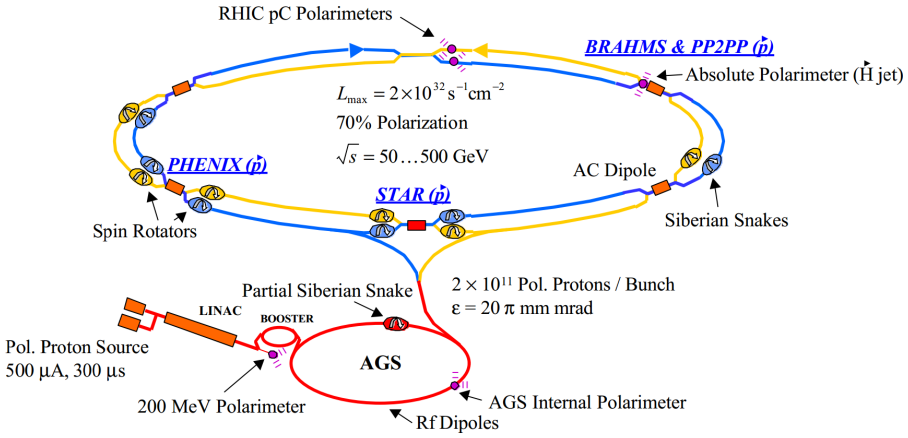

Figure 2.1: From [11]. Diagram of the RHIC/AGS Facility Complex.

2.1.1 Polarized p+p Operation

From Source to Accelerator

Each polarized proton bunch in RHIC start as a single pulse of polarized H^- ions from the Optically Pumped Polarized Ion Source (OPPIS), produced at a rate of 7.5 Hz. Initially, there are about 9×10^{11} ions in each pulse at 80% polarization. The H^- ions are accelerated to 200 MeV by a radio-frequency quadrupole followed by a 200 MHz LINAC. The ions are then passed through a stripping foil that removes the electrons, and the remaining polarized protons are captured into single bunches in the low energy booster ring where they are accelerated to about 2 GeV. Next each proton bunch passes to the main Alternating Gradient Synchrotron (AGS) ring where it is accelerated to about 23 GeV before being passed through a spin transparent transfer line into the main RHIC synchrotron ring. The process, which has about 50% intensity transmission efficiency, is repeated until all the bunches in the Blue and Yellow RHIC beams are filled, at which point the bunches can be accelerated to a variety of energies including 31, 100, and 250 GeV.

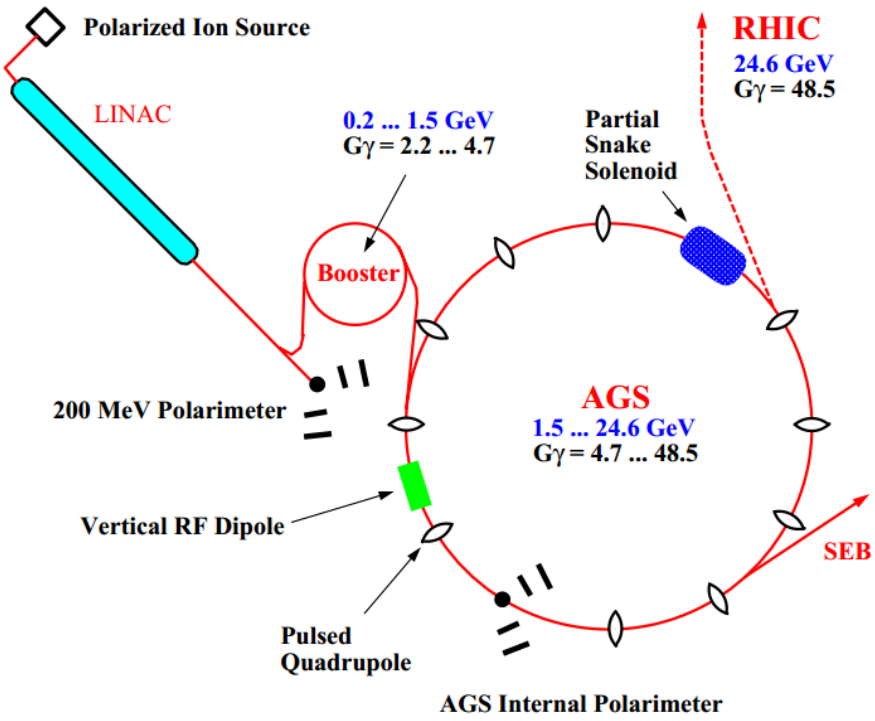

Figure 2.2: From [11]. Diagram of the components that create and accelerate the polarized proton beam before injection into RHIC.

Spin Pattern

The spin pattern at RHIC is set at the level of the pulses from OPPIS. In practice, any pattern can be chosen, although more frequent changes slow the total injection time. Being able to measure all of the double and single spin asymmetries dictates the pattern chosen, as does the constraint to see all physically distinct patterns cycled within a short time period to reduce the introduction of systematic uncertainties from changing beam conditions. Fig. 2.3 shows the spin patterns used in RHIC for the 2009 run, with the bunches used to calculate particular asymmetries highlighted.

Siberian Snakes and Spin Rotators

The Lorentz equation for orbital motion of a charged particle in a vertical magnetic field $\mathbf{B}_\perp$ is

$$\frac{d\mathbf{p}}{dt} = \mathbf{p} \times \left[-\frac{e}{\gamma mc} \mathbf{B}_\perp \right], \tag{2.1}$$

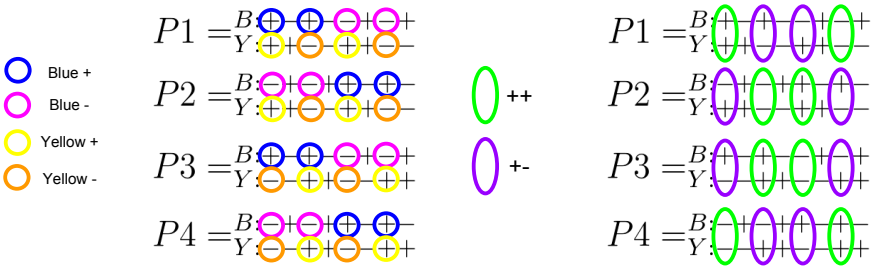

Figure 2.3: The spin patterns used in the 2009 run, with bunches used to calculate single spin asymmetries (left plot) and double spin asymmetries (right plot) in even crossings circled. The full patterns are a repetition of what is shown over all 120 bunches (excluding bunches intentionally left empty).

which translates to a precession frequency of $\frac{e}{\gamma mc}B_\perp$. The stable polarization direction in the vertical RHIC holding magnetic field is vertical. If the direction happens to be slightly off axis, the spin $\mathbf{S}$ of the protons will process according to the Thomas-BMT equation [19], which in the absence of an electric field and at near light speed ($1/\gamma \approx 0$), simplifies to

$$\frac{d\mathbf{S}}{dt} = \mathbf{S} \times \left[-\frac{ea}{mc}\mathbf{B}_\perp \right], \tag{2.2}$$

where $a = (g-2)/2$ is the "magnetic moment anomaly" of the proton. This means the protons spin will precess about the vertical axis at a frequency $\frac{ea}{mc}B_\perp$. The ratio of this frequency to that of orbital motion,

$$\left(\frac{ea}{mc}B_\perp\right) / \left(\frac{e}{\gamma mc}B_\perp\right) = a\gamma \equiv \nu_{\text{spin}} \tag{2.3}$$

is called the spin tune. If $\nu_{\text{spin}} = n$, where n is an integer, protons will periodically encounter any given point in the ring with a specific phase in their spin precession. Therefore, if at a given point in the ring there is some imperfection in the magnetic field that perturbs the precession, the perturbation will add constructively over multiple orbits and degrade the overall polarization of the beam in what is referred to as an "imperfection resonance."

Another concern is betatron oscillations, wherein the beam periodically deviates from its design orbit as it circles the ring. As with the spin tune, a "betatron tune" ν_{beta} can be defined by taking the ratio of the betatron oscillation frequency to that of orbital motion. In the simplest example, betatron oscillations occur in a constant vertical magnetic field when the beam

follows any of the other stable orbits transversely offset from the design orbit. These other orbits will intersect the design orbit at two points, resulting in a betatron tune of 1. In practice, there exist non-integer betatron tunes in a synchrotron, both in the vertical and horizontal plane, due to the periodic placement of magnets around the ring, referred to as the "magnetic lattice". Such deviations of the beam cause a depolarizing resonance when the spin tune matches the betatron oscillations or is an integer multiple of the magnetic lattice spacing. This type of resonance is referred to as an "intrinsic resonance."

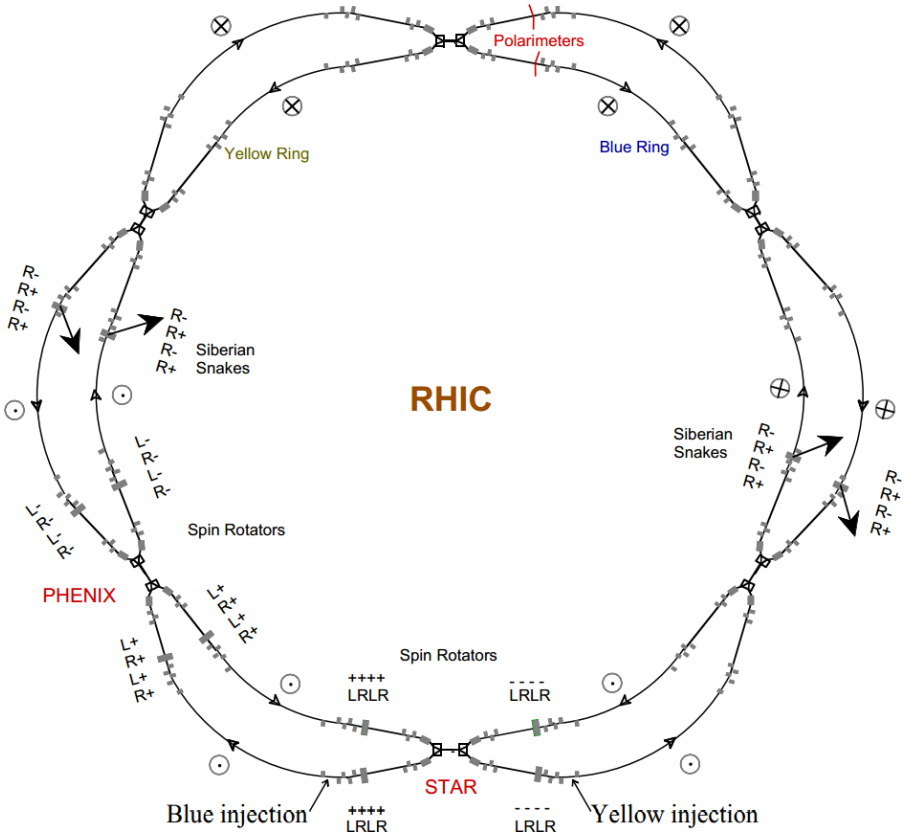

Figure 2.4: From [11]. A non-scale diagram of the RHIC ring showing the placement and handedness of the Siberian snake and spin rotator helical dipole magnets. Handedness of the four helical dipole magnets in each snake and rotator are labeled, and the polarization direction in each region of the ring is shown.

As a solution to this problem, RHIC employs "Siberian Snakes," each snake a set of four helical dipole magnets that creates a magnetic field perpendicular

to the spin vector, causing it to rotate. There are two full snakes in each ring in RHIC, and their positions are shown in Fig. 2.4. Each snake rotates the polarization vector by 180° around separate axes perpendicular to the (vertical) polarization axis, as in Fig 2.5. The net effect is to cause a 180° precession about the polarization axis so that the effects of depolarizing resonances are canceled on successive passes around the ring. There is also a partial snake in the AGS to cancel resonances, albeit over a greater number of cycles. Figure 2.6 shows the improvement in polarization retention across an intrinsic resonance with the RHIC snakes.

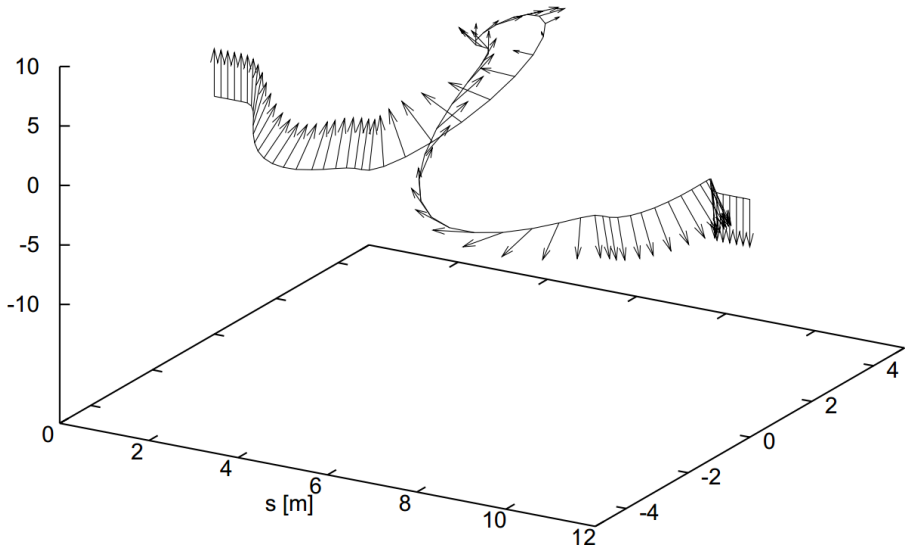

Figure 2.5: From [55]. The path and polarization direction of a polarized proton bunch passing through a full Siberian snake.

As seen in Fig. 2.4, there are also spin rotators on opposite sides of each IR. The spin rotators have the same design as the snakes but the handedness and magnetic field strength of each component helical dipole differs from those in the snakes so that instead of causing a net 180° rotation about the polarization axis, the spin rotators before the IR can change the polarization direction from vertical to horizontal. After passage through the zero-field IR, this operation is undone by the partner spin rotators opposite the IR.

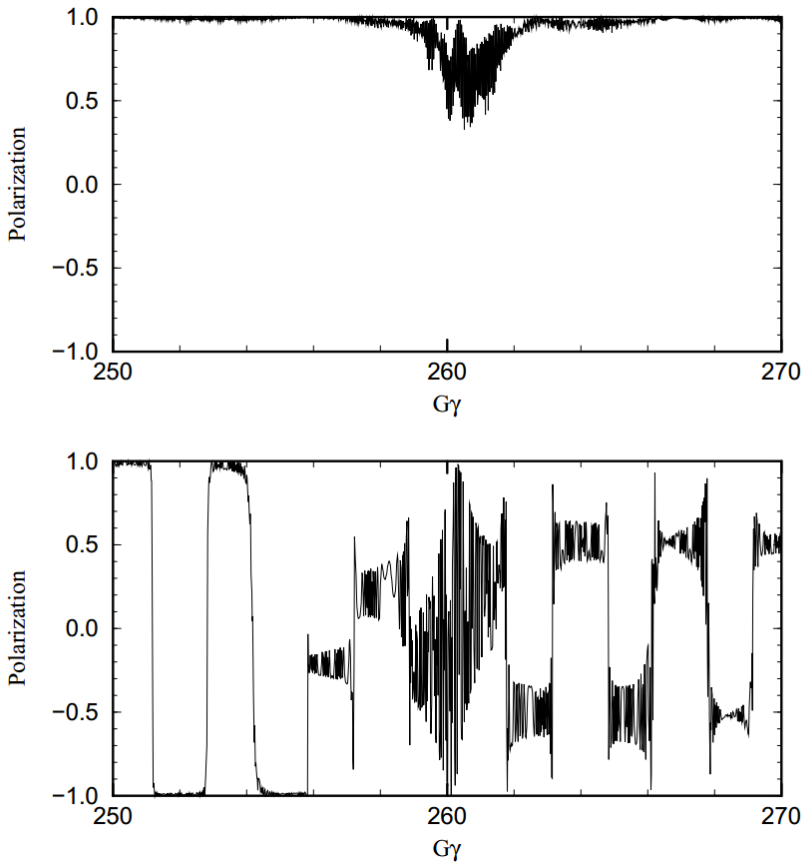

Figure 2.6: From [11]. The upper plot shows the relative proton bunch polarization vs. a scan across an intrinsic depolarizing resonance with the RHIC Siberian snakes ON. The lower plot is the same scan with the snakes OFF, which reveals many other weaker depolarizing resonances. The unit G corresponds to the magnetic moment anomaly that is called a above.

2.1.2 Monitoring

Beam Position Monitors

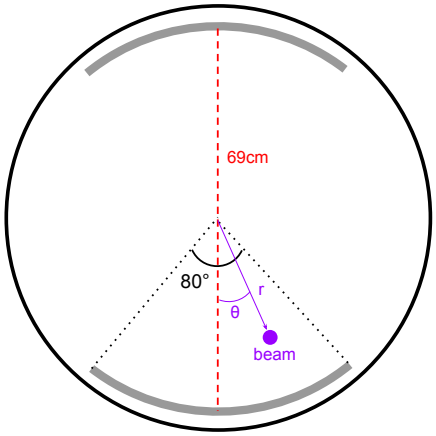

Figure 2.7: Cross-sectional sketch of the relevant design parameters in a single-plane RHIC stripline BPM.

There are hundreds of "stripline" Beam Position Monitors (BPMs) located around RHIC, used to measure the beam position at the ring's various magnets, points of β_{max}, and at opposing sides of the experimental IRs. Some are of the single-plane design shown in Fig. 2.7, while others, like those surrounding the IRs, are dual-plane BPMs which are essentially two single-plane BPMS superimposed with one rotated 180° around the beam axis. The striplines that give the detector its name (depicted as the grey arcs in Fig. 2.7) are wire EDM cut from 316L stainless-steel tubing, and extend 23 cm along the beam axis. The signal is generated from the difference in the image current between two striplines, which depends on the displacement of the beam. The image current density induced by a pencil beam of current I_{beam} in a metal plate at radius a and azimuthal angle ϕ is given in terms of the transverse coordinates of the beam (r, θ) as (from [35])

$$j_{im}(\phi) = \frac{I_{beam}}{2\pi a}\left(\frac{a^2 - r^2}{a^2 + r^2 - 2ar \cdot \cos(\phi - \theta)}\right), \tag{2.4}$$

and the current in a plate covering an azimuthal angle α is

$$I_{im} = \int_{-\alpha/2}^{+\alpha/2} a \cdot j_{im}(\phi) d\phi. \tag{2.5}$$

The ratio of such an image current to the beam current is plotted versus the beam location in Fig. 2.8(a) using the RHIC BPM parameters as given in Fig. 2.7. The response becomes less sensitive to the beam angle at small displacements. As shown in Fig. 2.8(b), the change in signal with angle are a few parts in 10^6 or less for displacements along the BPM plane of up to 900 μm, which is far smaller than the calibration and signal transmission uncertainties.

The location of the BPM electrical center is determined in-situ by means of a calibration antenna, shown with the BPM assembly in Fig. 2.9. Reading the antenna signal in the BPM gives the position of its electrical center relative to the antenna's electrical center, which is then related to survey measurements of the antenna electrical center relative to its external fiducials. This calibration procedure determines the BPM electrical center to $\sigma = 50$ μm. The roll accuracy cannot be measured in-situ and was calibrated before installation to about $\sigma = 1$ mrad. There is also a dependence of the measurement on the signal frequency. It varies by about 50 μm from 1 MHz to 100 MHz, and is attributed to reflections at imperfect terminations and coupling to other electronics in the room.

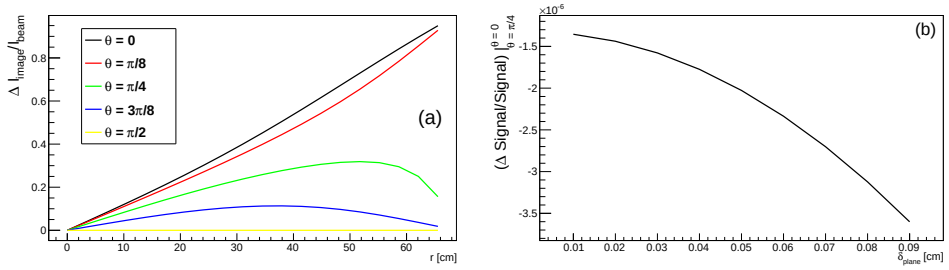

Figure 2.8: (a) Prediction for the difference in image current between the two strips shown in Fig. 2.7 relative to the beam current as a function of the beam position, calculated from Eqs. 2.4 and 2.5. (b) Relative change in signal for a beam at angle $\theta = 0$ and a beam at angle $\theta = \pi/4$ with equal displacements δ_{plane} in the BPM measurement plane, out to the typical maximum beam displacement in a Vernier scan [32] of 900 μm.

Each plane of the two dual-plane PHENIX BMPs have designations that refer to their position relative to the IR and which beam they measure. The $DX.7_{B,Y}$ BPMs are on the South side of the IR, and the $DX.8_{B,Y}$ BPMs are on the North side. "DX" refers to their location at the DX magnets. An example of the readings from all of the BPMs for the $\sqrt{s} = 200$ GeV Run in 2009 are shown in Fig. 2.10. These values can be combined in various ways to give the angles of the beams or collision axis through the IR, as will be done

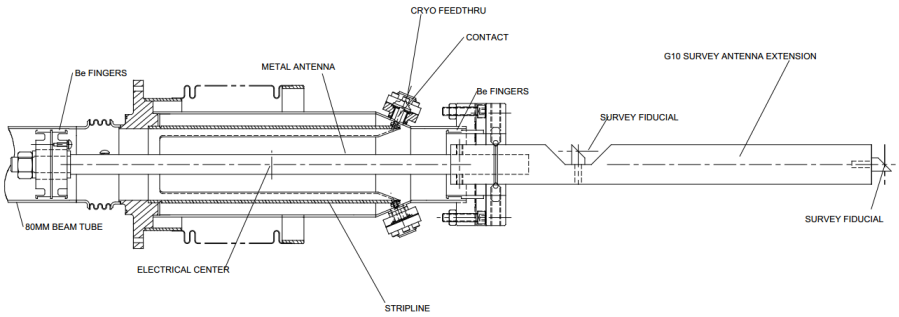

Figure 2.9: From [24]. Top view of a Beam Position Monitor with antenna installed.

in Section 4.4.

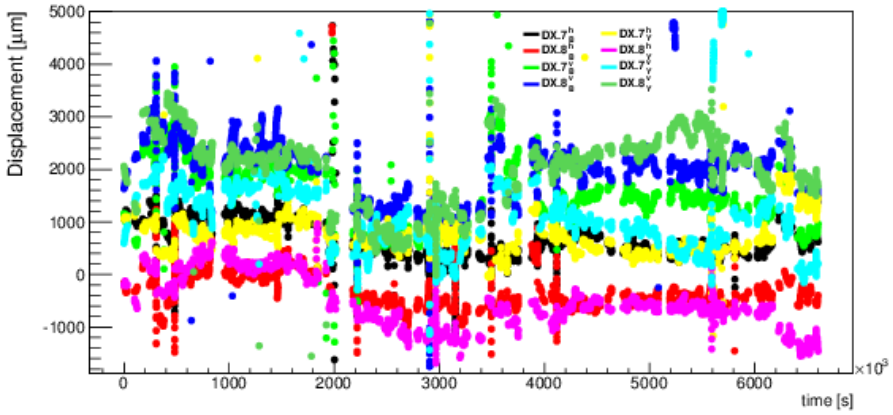

Figure 2.10: Raw BPM data in the 2009 run at $\sqrt{s} = 200$ GeV.

Wall Current Monitors

The RHIC wall curent monitor, or WCM, system measures the longitudinal profile of proton or heavy-ion bunches in the RHIC rings. This information is useful for such reasons as calculating the machine luminosity and determining the longitudinal emittance (spread in momentum and time) of the beam. The system operates similar to the design shown in Fig. 2.11, with the single-turn secondary rotated around the longitundinal axis to form a case for the ferrite core. There are three WCMs at RHIC, two at the 2 o'clock position (one for each ring), and an additional WCM at the 4 o'clock position where the singals from counter-rotating bunches in the two rings cancel, which can aid in adjusting the collision point.

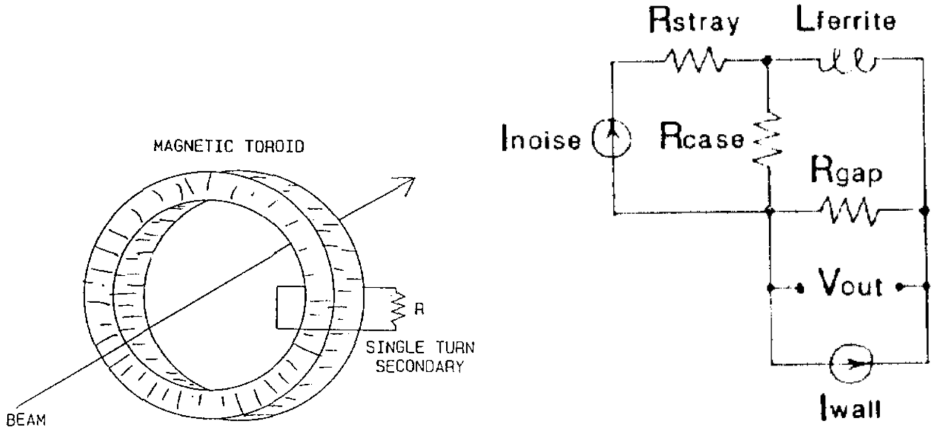

Figure 2.11: Left: Simple device for measuring a beam current, from [60]. It consists of a ferrite ring inductor with a single turn. Right: Equivalent circuit, with additional elements for a case to isolate the detector from outside noise. From [48].

If a beam image current passes through the center of the toroid, the induced voltage across the single-turn secondary winding will be given according to Lenz's law as the difference in flux from the beam current i_b and the flux due to the compensating current driven in the secondary winding i_s,

$$v_S = L\left(\frac{di_b}{dt} - \frac{di_s}{dt}\right). \tag{2.6}$$

Substituting $i_s = v_S/R$ and using a Fourier transform to the frequency domain, which, acting on the time derivatives, brings out a factor $j\omega$, where $j = \sqrt{1}$,

we arrive at

$$V_s(\omega) = j\omega L \left(I_b - \frac{V_s(\omega)}{R} \right), \tag{2.7}$$

which can be solved as

$$\begin{aligned} V_s(\omega) &= j\omega L \cdot \frac{I_b(\omega)}{1 + j\omega L/R} \\ &= \omega L \cdot I_b(\omega) \cdot \frac{\omega L/R + j}{1 + (\omega L/R)^2}. \end{aligned} \tag{2.8}$$

The magnitude of the response is then

$$\left| \frac{V_s(\omega)}{I_b(\omega)} \right| = \frac{\omega L}{\sqrt{1 + (\omega L/R)^2}}. \tag{2.9}$$

Fig. 2.12 shows this response plotted vs. frequency, with typical parameters similar to those for the RHIC WCMs. The frequecy range from the $1/\sqrt{2}$ point is close to what is quoted for the RHIC WCMs, about 3 kHz to 6 GHz [25].

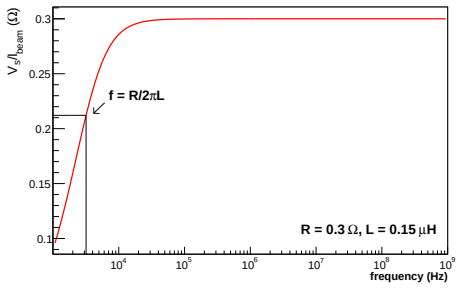

Figure 2.12: Response of the WCM design shown in Fig. 2.11 versus frequency, given the parameters shown in the legend. The corner frequency, where the response drops from its maximum by a factor $1/\sqrt{2}$, is also marked on the plot.

During typical in-store operation, WCM readings of the entire 120 bunch profile are taken approximately every 5 minutes. As an example, a superposition of the WCM readings for the first 10 bunches in the blue beam are shown in Fig. 2.13, both for the 2009 and the 2012 RHIC run.

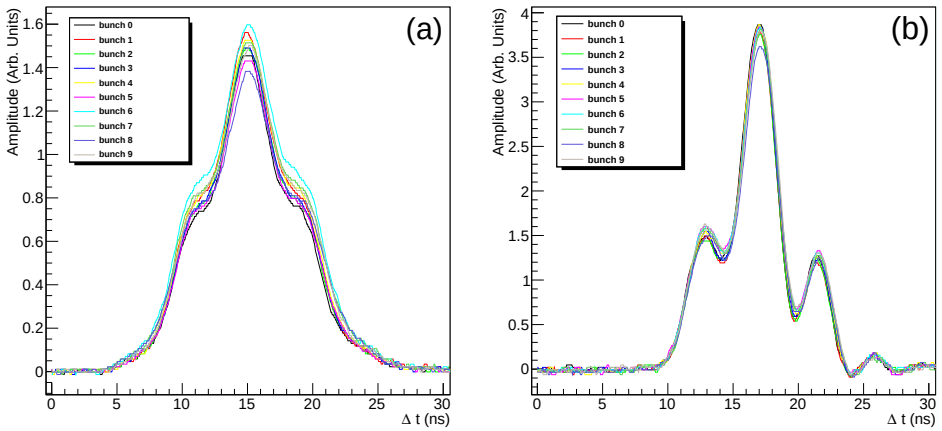

Figure 2.13: Example WCM readings of the first 10 bunches in the yellow ring. (a) shows a reading from the 2009 $\sqrt{s} = 200$ GeV RHIC run, and (b) shows a reading from the 2012 $\sqrt{s} = 510$ GeV RHIC run. The stark difference in bunch shape is due to the introduction of the 9 MHz RF system in the 2011 run.

2.1.3 CNI Polarimetry

Both types of polarimeters in RHIC operate on the basis of **C**oulomb-**N**uclear **I**nterfecence, or CNI, a phenomenon that takes place in proton-proton elastic scattering at small momentum transfer where Coulomb and Nuclear cross sections become comparable in size. To see how spin dependence comes into play, consider the five independent scattering amplitudes for longitudinally polarized protons:

$$\begin{aligned}
\Phi_1 &= \langle ++|M|++\rangle \\
\Phi_2 &= \langle ++|M|--\rangle \\
\Phi_3 &= \langle +-|M|+-\rangle \\
\Phi_4 &= \langle +-|M|-+\rangle \\
\Phi_5 &= \langle ++|M|+-\rangle,
\end{aligned} \tag{2.10}$$

where $+, -$ denote the helicity each proton. The remainder of the 16 possible amplitudes can be related to the above via parity invariance of the electromagnetic and strong forces, and by exchanging the labeling of the protons in the initial or final state (of these, 7 are equal to Φ_5, which gives it a relative weighting of 4 in the total cross-section). These amplitudes can be expressed in terms of an electromagnetic amplitude plus some hadronic amplitude, offset

by the "Coulomb phase" δ:

$$\Phi_j = \Phi_j^{em} + e^{-i\delta}\Phi_j^h. \tag{2.11}$$

The single-spin asymmetry A_N can be expressed ([23]) in terms of δ and the ratio of the single-spin-flip amplitude to the non-spin-flip amplitudes

$$r_5 = \frac{m_p}{\sqrt{-t}} \frac{2\Phi_5}{Im(\Phi_1 + \Phi_3)}, \tag{2.12}$$

where m_p is the mass of the proton and t is the square of the momentum transfer. These terms are important to describe the shape and exact magnitude of A_N, but the theory still predicts non-zero A_N if r_5 and δ are set to zero. The theoretical prediction for A_N in $p+p$ and $p+C$ processes is shown in Fig. 2.14.

The RHIC polarimeters measure energy and time-of-flight of the elastic recoil protons or carbon, for which the kinetic energy follows the non-relativistic relation

$$E_{meas} + E_{loss} = \frac{m}{2} \times \frac{L^2}{(t_{meas} + t_0)^2} \tag{2.13}$$

with calibration factors E_{loss} and t_0. Fitting the time vs. energy distribution to this function allows these elastic events to be distinguished from background.

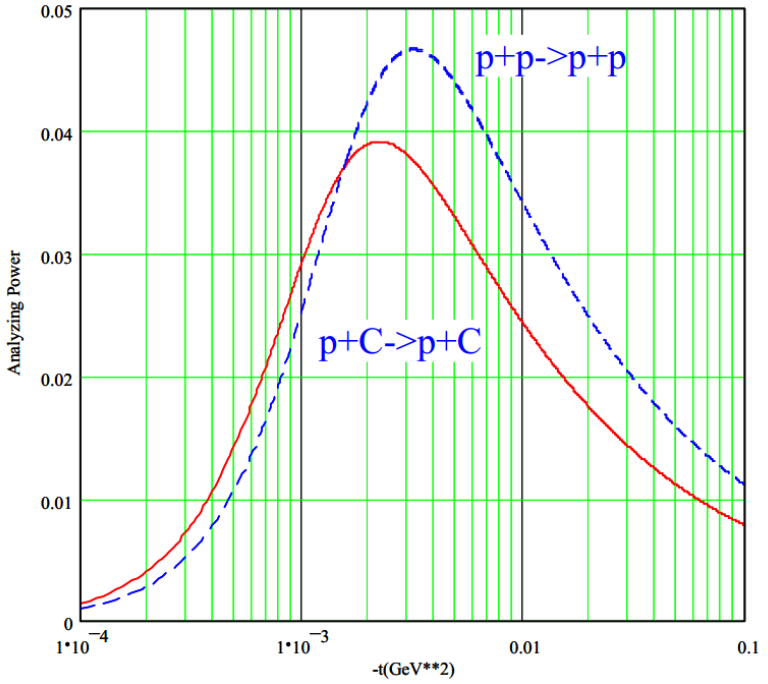

Figure 2.14: Analyzing power (A_N) of the CNI process for elastic $p + p$ and $p + C$ scattering for a 250 GeV proton beam. From [41]

H-Jet Polarimeter

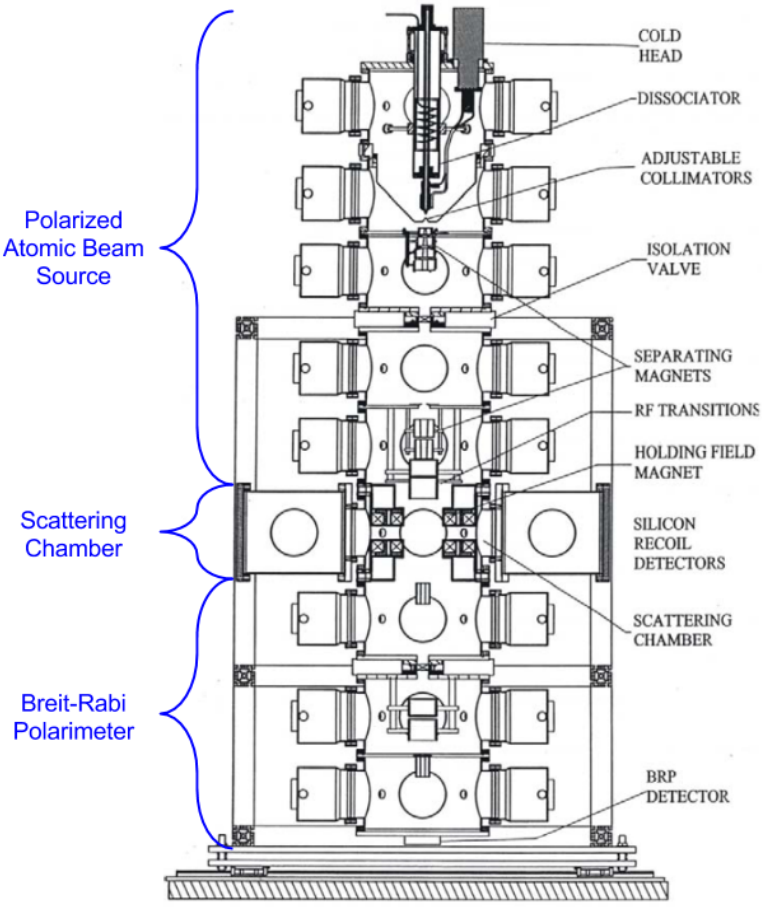

Figure 2.15: Diagram of the hydrogen-jet polarimeter. From [61]

A diagram of the Hydrogen-jet polarimeter is shown in Fig. 2.15, details of which are given in [61]. Located at the 12 o'clock position, its purpose is to provide a vertically polarized atomic hydrogen beam for scattering with the vertically polarized RHIC beams. The first stage of the system is the polarized atomic hydrogen beam source, which dissociates diatomic hydrogen with an RF field operating nominally at 21.6 MHz and $200 - 300$ W. The atomic hydrogen is then cooled to cryogenic temperatures below 100 K as it escapes out a nozzle headed towards the RHIC beam. After leaving the nozzle, the atomic hydrogen beam passes through a magnetic field gradient provided by four sextupole magnets. The hyperfine splitting of hydrogen produces four quantum states, which, as detailed in [51], simplify in the presence of the

typical $1.6 - 1.7$ T sextupole field strength to

$$\begin{aligned} |1\rangle &= |e\uparrow, p\uparrow\rangle \\ |2\rangle &= |e\uparrow, p\downarrow\rangle \\ |3\rangle &= |e\downarrow, p\downarrow\rangle \\ |4\rangle &= |e\downarrow, p\uparrow\rangle. \end{aligned} \tag{2.14}$$

The field gradient acts as a Stern-Gerlach device for the electron polarization and sweeps states $|3\rangle$ and $|4\rangle$ from the beam, leaving only states $|1\rangle$ and $|2\rangle$, which differ in proton spin direction. The hydrogen beam is then focused by two additional sextupole magnets and subject to an RF field that selectively causes a transition from $|1\rangle$ to $|3\rangle$ (Weak Field Transition) or from $|2\rangle$ to $|4\rangle$ (Strong Field Transition), depending on the desired target proton spin state. Thus the hydrogen beam enters the scattering chamber with a uniform vertical proton polarization and scatters at a 90° angle with the RHIC beam.

After scattering, the hydrogen beam enters the Breit-Rabi polarimeter chamber. This chamber also has sextupole magnets in a Stern-Gerlach setup, which further reduces the beam into just one of the states in Eq. 2.14 before it strikes an ion-gage beam detector that measures the beam intensity. By switching between different combinations of the weak and strong field transitions, these intensity measurements can be used to extract the relative state populations and RF transition efficiencies, and this information can be used to find the target polarization, which is about 96%, as described in [51].

The Hydrogen-jet polarimeter gives a very accurate reading of the RHIC beam polarization due to the fact that the interaction is dominated by $p + p$ scattering and thus knowledge of the spin asymmetry A_N in the interaction is not required. In fact, the beam polarization can be determined directly from the ratio of the raw production asymmetry with respect to the RHIC beam ϵ_N^{beam} and the raw production asymmetry with respect to the atomic hydrogen beam, ϵ_N^{target}, as long as the hydrogen beam polarization, P_{target}, is known:

$$P_{beam} = -\frac{\epsilon_N^{beam}}{\epsilon_N^{target}} \times P_{target}, \tag{2.15}$$

which follows from the A_Ns being equal.

The raw asymmetries ϵ_N are measured for elastic $p + p$ scattering by selecting elastic recoil protons using time of flight and energy measurements in six silicon strip detectors. The detectors are parallel to the H-jet/RHIC beam scattering plane, with three on each side. The measurements determine P_{beam} to $6 - 8\%$ statistical uncertainty per fill, given an event rate of about 30 kHz.

The diameter of the H-jet beam is about 7 mm and the entire assembly can be shifted by 10 mm so that the H-jet beam scatters on only the yellow or blue RHIC beam, which are separated by about 10 mm at the 12 o'clock interaction region. The net polarization of the H-jet beam is cycled between up, zero, and down in intervals of 300, 30, and 300 seconds.

The dominant systematic uncertainties in the measurement are due to contamination of the H-jet beam by molecular (diatomic) hydrogen, and scattering of the H-jet beam with RHIC beam gas background. Diatomic hydrogen has zero net proton polarization and also does not register on the ion gauge detector in the Breit-Rabi polarimeter, so it enters as a dilution factor on the net polarization,

$$P_{jet} = (1 - \delta) P_{\text{Breit-Rabi}} \tag{2.16}$$

where δ is the admixture of molecular hydrogen in atomic equivalent units and is estimated to be $\delta = 3\% \pm 2\%$. Scattering with the beam gas may also produce an asymmetry, which modifies the effective A_N measured in the detectors.

$$A_N^{eff} = (1 - r) A_N + r A_N^{bgr}, \tag{2.17}$$

where r is the fraction of beam gas background, with a typical $r \approx 5\%$. Knowledge of A_N^{bgr} is consistent with zero, so this contribution also acts as a dilution factor [53].

p-Carbon Polarimeter

There are two pCarbon polarimeters in RHIC, one for each ring. A schematic layout of one is shown in Fig. 2.16. The polarized proton beams scatter on an unpolarized carbon ribbon of approximate dimensions 2.5 cm $\times$ 10 μm $\times$ 25 nm. Bunch by bunch polarization can be measured to about 4% statistical uncertainty with typical rates of 20 MHz. Usually four two-minute measurements are made per fill, which allows the polarization decay time to be sampled. The ribbons can also be scanned in different orientations across the beam to measure vertical and horizontal polarization profiles, with a positioning accuracy for the ribbon of ± 0.5 mm, limited by the ribbon straightness. The measurement opperates under the sample principle as the H-jet polarimeter, except that the Carbon ribbon is not polarized and the composition obviously does not match that of the proton beam. Therefore the analyzing power A_N in the measurement does not cancel and the polarization must be expressed in terms of the raw asymmetry ϵ_N as

$$P_{beam} = \frac{\epsilon_N}{A_N}. \tag{2.18}$$

To remove unertainty from the knowledge of A_N in p-Carbon CNI scattering, the measurement must therefore be normalized to the lower statistics H-jet measurement over a sufficiently long time scale, usually the entire Run-Year.

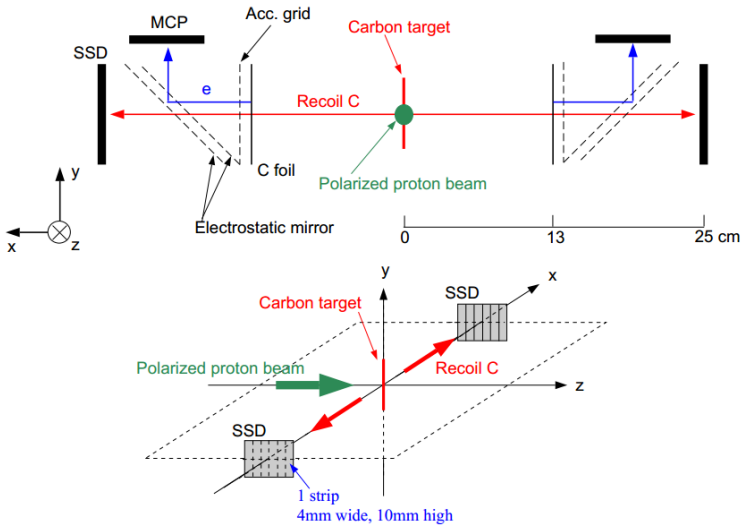

Figure 2.16: Schematic layout of the p-Carbon polarimeter. From [11]

To measure the asymmetry in recoil Carbon atoms, the detector employs 6 silicon strip detectors placed at 18 cm from the ribbon target. All hits with energy and ToF above a certain threshold are recorded. The layout of these detectors is shown in Fig. 2.16.

2.2 PHENIX

The PHENIX detector [8] consists of two forward muon arms and two central arms, the latter of which are shown in Fig. 2.17. The central arms each cover a pseudorapidity range of $|\eta| < 0.35$ and have azimuthal coverage of $\Delta\phi = \frac{\pi}{2}$. The PHENIX central magnet consists of two coils which provide a field-integral of up to 1.15 Tm in $|\eta| < 0.35$ when they are run with the same polarity, as was done in 2005 and 2006. In 2009, the two central coils were run with opposite polarity to create a field free region near the beam pipe for the newly installed Hadron Blind Detector [13], which is not used in the present analysis and has a negligible effect on π^0 and η meson decays as a conversion material. From a radius of 2–5 m, which is outside the magnetic field region, there are several tracking and PID detectors that are not used in this work. At a radius of

approximately 5 m, there is a thin multiwire proportional chamber called the pad chamber (PC3) followed immediately by an electromagnetic calorimeter (EMCal), both of which are used here. The coordinate system used to describe the PHENIX detector has a z-axis along the beam direction. Along this axis at forward rapidity are the Beam Beam Counters (BBC), which can be used to measure the z-vertex, and the Zero Degree Calorimeters (ZDC).

Figure 2.17: Beam view of the PHENIX central arm in 2009 [7]. Tracking detectors include the Drift Chambers (DC) and Pad Chambers (PC). The EMCal consists of two separate subsystems, the Lead Scintillator (PbSc) and the Lead-Glass Cherenkov Radiator (PbGL).

2.2.1 Zero Degree Calorimeters and Shower Max Detectors

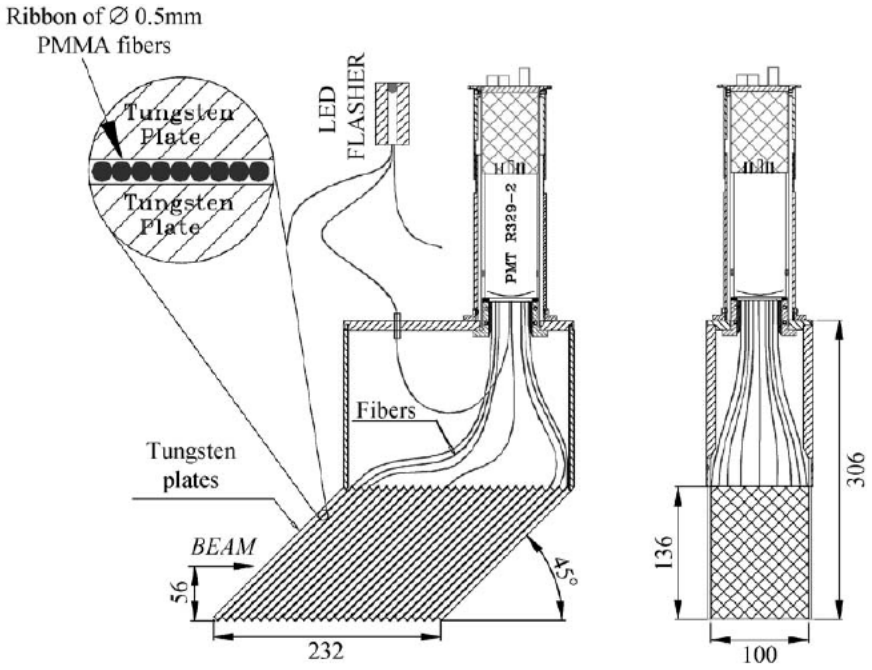

Figure 2.18: From [9]. Two views of a single module in the PHENIX Zero Degree Calorimeter (ZDC). Each arm of the detector has three such modules, with the Shower Max Detector (SMD) located between the first and second modules (see Fig. 2.19).

The PHENIX Zero Degree Calorimeter is illustrated in Fig. 2.18. The ZDC consists of two arms (one is shown in Fig. 2.19) located $|z| = 18$ m from the interaction point (IP) along the beam axis, covering $|\eta| > 6$. Each arm is composed of three modules of tungsten-scintillator sandwich calorimetry with a total of 5 nuclear interaction lengths. As the arms lie beyond the bending magnets, which serve to separate the two beams outside the experimental area but also sweep away charged particles from the interaction, the ZDC primarily triggers on neutrals. A ZDC trigger requires a minimum energy deposit in each arm of nominally 20 GeV.

The Shower Max Detector (SMD) is located behind the first ZDC module in each arm. Its position roughly coincides with the depth in hadronic shower development in the ZDC where the particle multiplicity is maximal. Each arm of the SMD has two layers of scintillator strip hodoscopes. The SMD is read

out in 7 strips of width 15 mm in the horizontal direction, and 8 strips of width 20 mm in the vertical direction. The normal to the SMD face makes a 45 degree angle with the beam axis, which makes the effective vertical strip width about 14 mm.

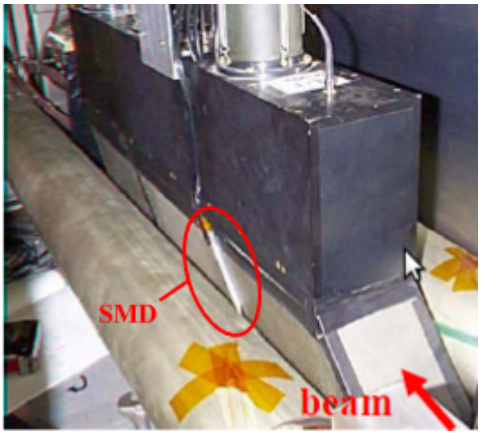

Figure 2.19: One of the arms of the PHENIX Zero Degree Calorimeter (ZDC).

2.2.2 Local Polarimetery

Local polarimetry at PHENIX is used to determine the degree of longitudinal polarization in the PHENIX IR. After a long shutdown or significant changes to the machine parameters, PHENIX runs with the spin rotator magnets (see 2.1.1) off (i.e. with the polarization direction vertical in the IR) for some time to establish with the ZDCs a baseline measurement of the single transverse spin asymmetry A_N of forward neutron production [6]. Then, when the rotators are turned on for longitudinal running, the remaining transverse component of each beam can be measured as

$$f_T \equiv \frac{P_T}{P} = \frac{A_{N,\text{rotators on}}}{A_{N,\text{rotators off}}} \tag{2.19}$$

and the corresponding longitudinal component is given by

$$f_L \equiv \frac{P_L}{P} = \sqrt{1 - \left(\frac{P_T}{P}\right)^2}. \tag{2.20}$$

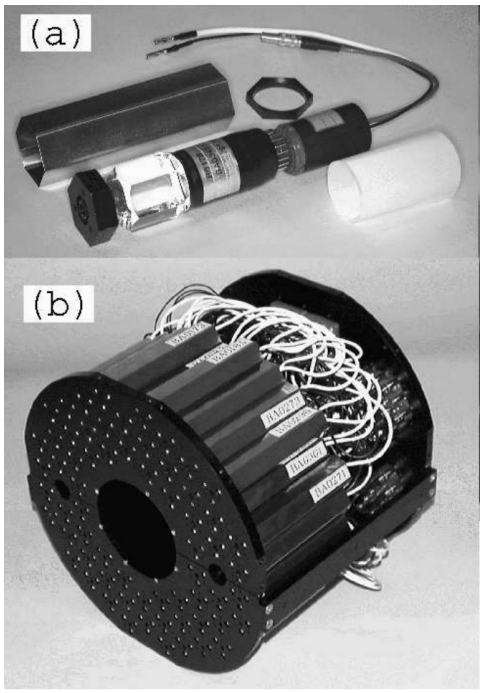

Figure 2.20: (a) View of a single quartz crystal and photomultiplier tube assembly. (b) One arm of the BBC, which holds 64 of the assemblies in (a). Both figures from [12].

2.2.3 Beam-Beam Counters

The main role of the PHENIX Beam-Beam Counters, or BBC, is to measure the time and z-vertex of a $p+p$ or heavy-ion collision by sampling hard scattering at forward rapidity, $3.0 < |\eta| < 3.9$. There are two arms to the BBC, each located 144 cm from the IP. One arm of the BBC is shown in Fig 2.20. It has an outer diameter of 30 cm and surrounds the beam pipe with 1 cm of clearance. Each arm is composed of 64 assemblies of quartz crystal, which act as Čerenkov radiators, in front of a photomultiplier tubes. Each group of 8 elements is controlled by a single power supply. The average timing resolution for each individual assembly under real experimental conditions is 52 ps with a standard deviation of 4 ps. If one PMT fires on each arm, with the initial time of the collision defined as $t_0 = (t_N + t_S)/2$ this translates into a timing resolution of 37 ps.

2.2.4 EMCal

The PHENIX Electromagnetic Calorimeter, or EMCal, employs two separate detector technologies that operate on different principles. Six out of the eight EMCal sectors (called the Lead Scintillator or "PbSc") are Shashlik calorimeters based on scintillation calorimetry, while the remaining two (called the Lead-Glass or "PbGl") are based on Čerenkov radiation calorimetry, which makes them significantly less responsive to hadrons.

The components of a PbSc calorimeter "module" are detailed in Fig 2.21. Each of the 3,888 modules contains 4 optically isolated "towers," which define the lateral segmentation of the calorimeter at 5.535×5.535 cm^2 per tower. The modules are grouped into 18×36 module arrays called "sectors," of which there 6 total. These sectors are not contiguous, and thus there is an acceptance edge at the perimeter of each. There is also a unit of "supermodule" defined for the PbSc, which is a 6x6 collection of modules. Each tower has a depth of 66 sampling cells, each cell a 0.4 cm layer of Polystyrene scintillator plus a 0.15 cm layer of lead. The lead acts as an absorber to produce electromagnetic showers, which trigger the release of scintillation light in the scintillator. To collect the scintillation light, 36 wavelength-shifting fibers pierce each layer, running the depth of the calorimeter and terminating at a photomultiplier tube. Other parameters of the calorimeter are summarized in Table 2.1. A PbGl "supermodule," a group of 6×4 towers with a common calibration system, is shown in Fig. 2.22. Each tower is 4×4 cm^2, which again defines the lateral segmentation of the detector. There are a total of 2 PbGl "sectors" in the EMCal, each a collection of 192 supermodules in a 12×16 array. This makes the PbGl sectors approximately the same size as the PbSc sectors, with sector areas of approximately 2×4 m^2 each. Each PbGl tower is a solid block of TF1-type lead-glass individually wrapped in 12-micron thick aluminized mylar to reflect the Čerenkov radiated light and direct it to a photomultiplier tube at the end of the block. The index of refraction of the mylar is 1.648.

Both the PbSc and PbGl are designed to measure the total energy of an electromagnetic shower, with active depths of 18.8 and 14.3 radiation lengths, respectively. The nominal energy resolutions from test-beam data are $8.1\%/\sqrt{E[\mathrm{GeV}]} \oplus 2.1\%$ and $6.0\%/\sqrt{E[\mathrm{GeV}]} \oplus 0.9\%$ [15]. They also have sufficient lateral tower segmentation ($\Delta\eta \sim 0.01$, 0.008 and $\Delta\phi \sim 0.01$, 0.008 rad., for the PbSc and PbGl respectively) to measure not only the position but also the transverse distribution of an electromagnetic shower, with a typical shower contained in a 3x3 array of EMCal towers. The segmentation is also sufficient to avoid pile-up at the highest RHIC $p + p$ rates and in the high-multiplicity environment of heavy ion collisions.

The relative time-of-flight (ToF) for showers can also be measured with the

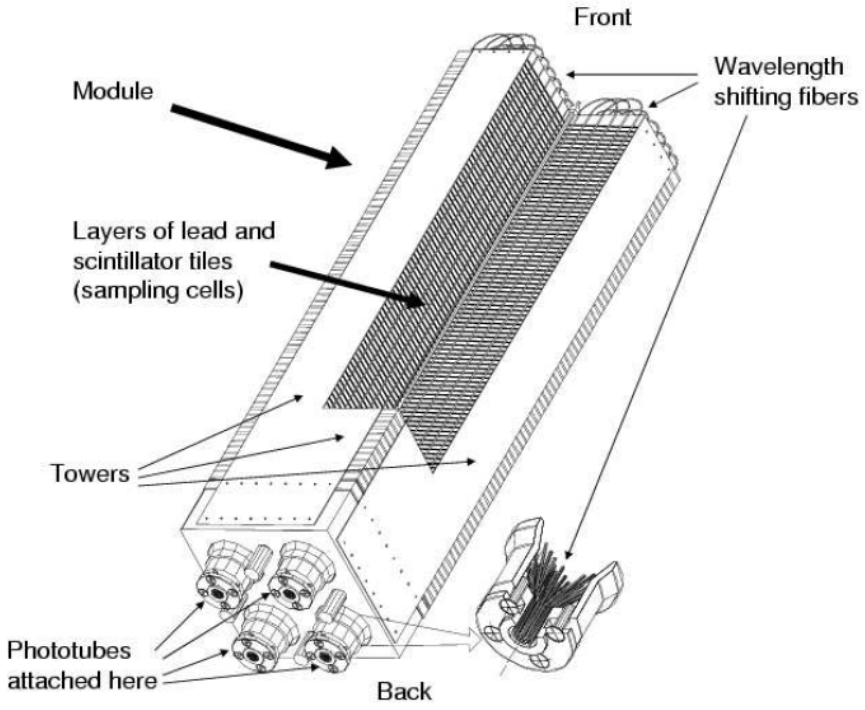

Figure 2.21: Partial cross-section diagram of a single Lead Scintillator module. The "leaky" optical fiber used for calibration can be seen at the core of the module. From [15].

EMCal with a timing resolution of about 0.7 ns (relative to the initial collision time t_0 measured by the BBC). This measurement can be used to reduce the contribution from hadrons and other backgrounds that are out of time from the expected arrival for a photon.

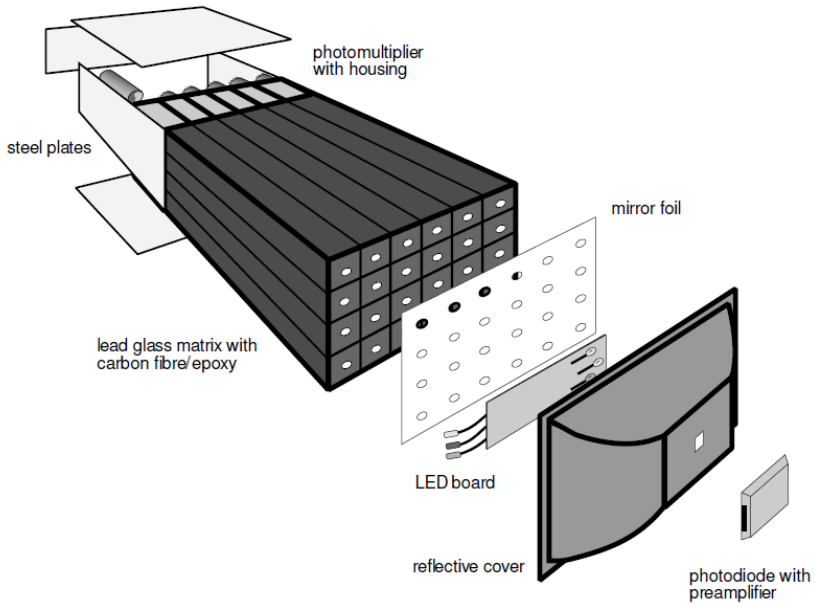

Figure 2.22: Exploded view of a Lead Glass supermodule (16 individual towers). The LED assembly at the beam-facing side is used for energy calibration. From [15].

Sub-Detector	PbSc	PbGl
Style	Shashlik	Čerenkov
Scintillator	Polystyrene (1.5% p-Terphenyl, 0.5% POPOP)	N/A
Absorber	Pb	N/A
Dielectric	N/A	Pb-Glass (TF1)
Active Depth, L (cm)	37.5	40
Segmentation (cm^2)	5.5×5.5	4.0×4.0
Segmentation ($\Delta\eta \times \Delta\phi$ [rad.])	0.01×0.01	0.007×0.008
Radiation Length, X_0 (cm)	2.0	2.8
Nuclear Interaction Length, λ_I (cm)	44	38*
Energy Resolution	$8.1\%/\sqrt{E[\text{GeV}]} \oplus 2.1\%$	$6.0\%/\sqrt{E[\text{GeV}]} \oplus 0.9\%$
Position Resolution (mm)	$1.55 \oplus 5.7/\sqrt{E[\text{GeV}]} \oplus (L/X_0)\sin(\theta)$	$0.3 \oplus 8.7/\sqrt{E[\text{GeV}]} \oplus (L/X_0)\sin(\theta)$
Electron Timing Resolution (ns)	$0.06 + 0.03/(E[\text{GeV}] - 0.01)$	$0.17/\sqrt{E[\text{GeV}]} \oplus 0.075$
Intrinsic Light Output (photo-electrons/GeV)	1.5×10^3	5×10^2

Table 2.1: Some properties of the two sub-detectors that constitute the PHENIX Electromagnetic Calorimeter (collected from [15]). The quantity θ in the PbSc position resolution is the impact angle (w.r.t. orthogonal). *Although λ_I is similar for the PbGl and PbSc, the PbGl is much less sensitive to hadrons due to their having a significantly higher Cherenkov threshold than electrons.

2.2.5 EMCal Trigger

To record a significant sample of events containing a π^0 meson with large transverse momentum (p_T), a high energy photon trigger is used. A trigger tile is defined as a 2×2 array of EMCal towers, and, for the π^0 analysis, the energy in a 2×2 array of tiles (or 4×4 towers) is summed and compared to the trigger threshold. To reduce loss at the edge of a tile, the groups of 4×4 towers overlap. For the $\sqrt{s} = 200$ GeV π^0 analysis, we use two trigger thresholds, one at 1.4 GeV, called the 4×4c and one at 2.1 GeV, called the 4×4a. For π^0s, these are maximally efficient at meson energies of > 4 GeV/c and > 6 GeV/c, respectively. Due to separate circuits for triggers in odd and even bunch crossings resulting in a small variation in the threshold energy, all analysis is performed separately for even and odd crossing data, except at sufficiently high energies where the trigger efficiency is constant.

2.2.6 EMCal Offline Energy Calibration

Tower-by-Tower Calibration

A separate high voltage is supplied to each supermodule in the PbSc and PbGl, which is adjusted on a short time scale to calibrate the response to a UV laser (in the case of the Pbsc) or an LED (in the case of the PbGl). To account for tower-by-tower differences in the EMCal response, an offline energy calibration must be performed. For each event, target towers are identified as those centered in a cluster with energy greater than 0.8 GeV. All possible pairings are then made with other clusters in the EMCal with energy greater than 0.3 GeV and with a pair $p_T > 1$ GeV/c. A shower shape cut is also used on the clusters to remove hadrons. The data for the calibration must be accumulated over a significant portion of the Run Year to get sufficient statistics to histogram the π^0 mass peak in each tower. Once the peak position is measured for each tower, that tower's energy is scaled by a "calibration coefficient" factor that would put the π^0 mass peak at 137 MeV, which is the nominal position expected in the EMCal due to energy smearing effects. Since the individual tower energy is not the total energy of the cluster, the calibration must be iterated to converge on final values for the calibration coefficients. The effect of the tower-by-tower calibration on the π^0 peak position and width are shown in Figures 2.23 and 2.24.

Run-by-Run Calibration

Since the above calibration covered the entire 2009 Run for each tower (in order to have adequate statistics), an additional run by run calibration was

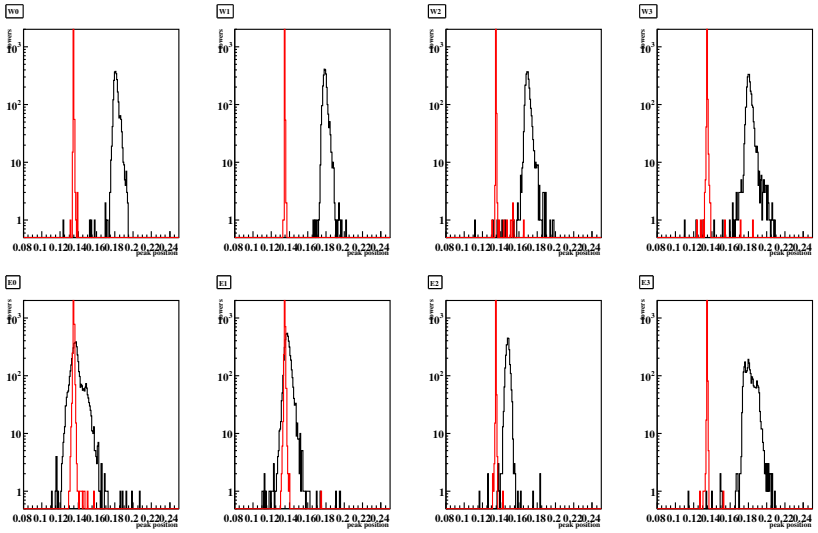

Figure 2.23: 2009$\sqrt{s} = 200$ GeV π^0 peak position for each sector in the EMCal before and after the EMCal tower-by-tower calibration. Sectors E0 and E1 are the PbGl.

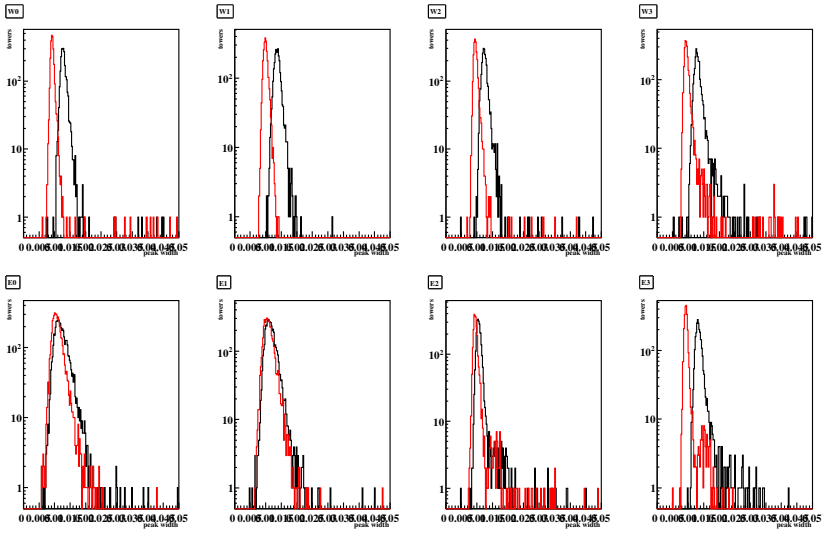

Figure 2.24: 2009$\sqrt{s} = 200$ GeV π^0 peak width for each sector in the EMCal before and after the EMCal tower-by-tower calibration. Sectors E0 and E1 are the PbGl.

required for each EMCal sector. Cluster energies from a given sector were multiplied by 137 MeV divided by the peak position measured in the stability check. Those details can be found in the next subsection.

EMCal stability

The EMCal stability is checked by fitting the π^0 peak position, width, and background fraction under the π^0 peak. This check is done run-by-run and sector-by-sector, with the spurious outlier runs (judged using Chauvenet's Criterion) excluded from the analysis. π^0s with p_T between 2.0 and 3.0 GeV/c are used here and the selection of π^0s by various cuts is the same as the main analysis. The background fraction $\frac{N_{BG}}{N_{\pi^0}+N_{BG}}$ is calculated within a ± 25 MeV/c^2 window around the π^0 mass peak.

Figures 2.25 through 2.27 show the π^0 peak position, π^0 peak width, and background contributions as a function of run number.

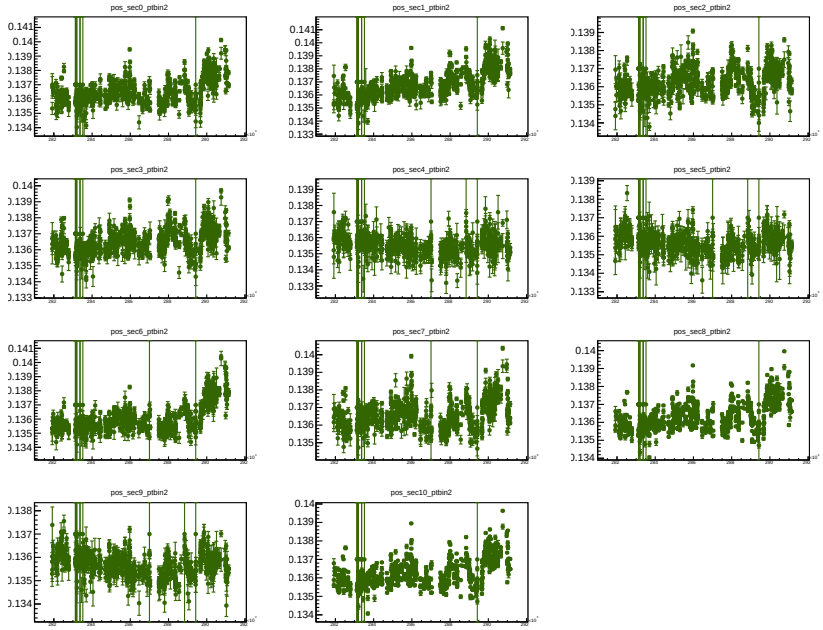

Figure 2.25: Run dependence of π^0 mass peak position in EMCAL for all sectors. The last two plots show the aggregated PbSc and PbGl.

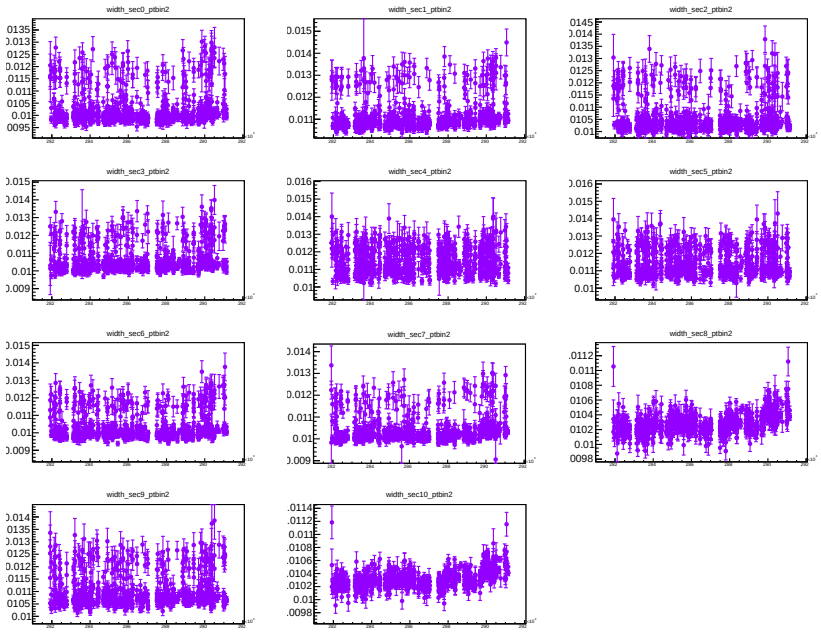

Figure 2.26: Run dependence of π^0 mass peak width in EMCAL for all sectors. The last two plots show the aggregated PbSc and PbGl.

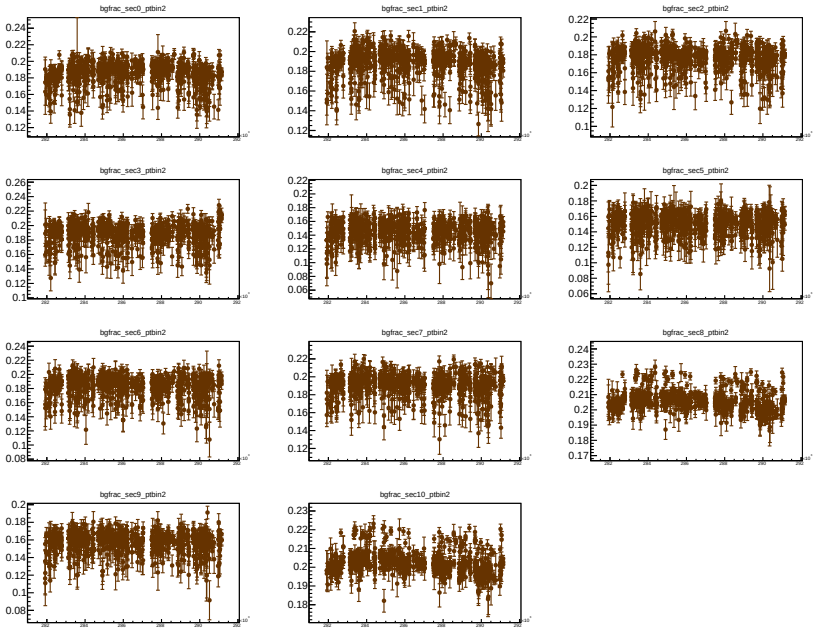

Figure 2.27: Run dependence of background fraction under π^0 mass peak in EMCAL for all sectors. The last two plots show the aggregated PbSc and PbGl.

2.2.7 Pad Chamber 3

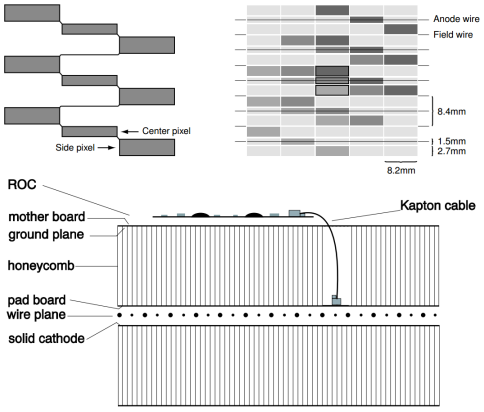

Figure 2.28: From [44]. Top Left: Readout geometry of the Pad Chambers. Nine non-adjacent pixels are read out at once. Top Right: Pixel layout with some readout groups highlighted, and an example of three pixels that constitute a "cell" are outlined in black. Bottom: Side view of a Pad Chamber.

PHENIX has Pad Chamber (PC) detectors in each arm at varying radii for the tracking of charged particles. They are single plane multiwire proportional chambers with one of the two cathodes segmented into fine pixels, which sense an induced charge from avalanches of positive ions onto the wires. Some diagrams of the PC design are shown in Fig. 2.28. The position resolution in the PCs is set by "cell" size, with a cell being a group of three pixels. The pixels are "ganged" together in non-adjacent groups of nine to reduce the number of readout channels. The condition for a valid hit is satisfied when an avalanche is sensed by three "gangs" that cover a given cell. This triple coincidence requirement reduces background. The PCs have a very high efficiency, $> 99.5\%$ at plateau.

The last layer in the PC system, the PC3, sits directly in front of the EMCal in each arm, and is thus very useful for vetoing charged tracks that leave an energy deposit in the EMCal. The cells in the PC3 are 1.7×1.7 cm^2, which is significantly smaller than the position resolution of any EMCal tower. The exact two dimensional position resolution depends on whether a hit is contained within a single cell or split between two cells. In the former case, the resolution is simulated at 4.9 mm along the direction of the wires, and 6.1 mm across the wires. In the latter case, the resolution improves and is 3.2 mm along the wires and 4.8 mm across [49]. The third position coordinate is provided by the PC3 radius.

2.3 STAR Scalers

There are 3 STAR scaler boards at the PHENIX experiment, so named because they were initially designed for use in the STAR collaboration. Each scaler board has 24 inputs plus a clock, and keeps a separate count for all 2^{24} correlations of input signals, with 40 bits of memory each [26]. On each board, 7 inputs need to be reserved for the crossing counter, since there are 120 crossings and $2^7 = 128$ is the next largest number. That leaves 17 inputs open for counting various other correlations, although one of those is usually reserved for the DAQ busy bit so that live or raw rates can be calculated. At PHENIX, these scalers are incremented and read out over one run. To time in the STAR scalers, fine and coarse delays can be set. The course delay corresponds to the beam clock, typically about 106 ns. The fine delay is 1/8 of the coarse delay.

Chapter 3

Analysis

3.1 π^0 Reconstruction

In order to count the number of neutral pions, a two photon invariant mass spectrum is constructed from all combinatorial EMCal cluster pairings using the relation for a decay into two massless photons,

$$m^2_{\gamma\gamma} \equiv 2E_1E_2(1 - cos\theta), \tag{3.1}$$

where E_1 and E_2 are the energies of the two clusters and θ is the angle between the two vectors from the decay vertex to the EMCal clusters. The branching ratio for the $\pi^0 \rightarrow \gamma + \gamma$ decay is more than 99%, so such a reconstruction should include almost all of the π^0 that decay into the EMCal acceptance. The mean decay time for a π^0 is about 9×10^{-17} seconds, which means it decays after traveling about 26 nm and the collision vertex can be assumed equal to the decay vertex for our analysis.

3.2 Asymmetry Calculations

A double longitudinal spin asymmetry in production of some final state is defined in terms of cross sections:

$$A_{LL} = \frac{\sigma_{++} - \sigma_{+-}}{\sigma_{++} + \sigma_{+-}}, \tag{3.2}$$

where the indices denote the helicity configuration of the initial state (++ being like helicity, and +− being unlike helicity). Experimentally, measuring A_{LL} as written in Eq. 3.2 is not feasible due to the sizable systematic uncertainties in any cross section measurement, and the small asymmetries

expected. However, we may make use of the relation

$$\sigma = \frac{\left(\frac{N}{\epsilon}\right)}{L} \tag{3.3}$$

, where N is the particle yield in the detector, ϵ is the efficiency times acceptance of the detector, L is the $p+p$ luminosity. Using Eq. 3.3 and assuming efficiency times acceptance is constant across different helicity combinations, A_{LL} can be expressed as

$$A_{LL} = \frac{1}{P_B P_Y} \frac{N_{++} - RN_{+-}}{N_{++} + RN_{+-}} \tag{3.4}$$

where N is the observable yield in the given helicity state and $P_{B(Y)}$ is the polarization of the Blue (Yellow) beam. R is the relative luminosity between helicity states, and is defined as

$$R = \frac{L_{++}}{L_{+-}} \tag{3.5}$$

where the luminosity is measured in each helicity state. The uncertainty in A_{LL} calculated this way is

$$\begin{aligned}(\Delta A_{LL})^2 &= \left(\frac{1}{P_B P_Y} \frac{2RN_{++}N_{+-}}{(N_{++}+RN_{+-})^2}\right)^2 \left(\left(\frac{\Delta N_{++}}{N_{++}}\right)^2 + \left(\frac{\Delta N_{+-}}{N_{+-}}\right)^2 + \left(\frac{\Delta R}{R}\right)^2\right) \\ &\quad + \left(\left(\frac{\Delta P_B}{P_B}\right)^2 + \left(\frac{\Delta P_Y}{P_Y}\right)^2\right) A_{LL}^2 \end{aligned} \tag{3.6}$$

According to Section 3.2.2, we may neglect the fill-by-fill uncorrelated systematic uncertainty in the polarization terms. We may also neglect the fractional statistical uncertainty on R since it is much smaller than that of the yield terms. Then, since there is no fill-to-fill uncorrelated relative luminosity systematic uncertainty, we need not carry it through our fill-by-fill calculations.

As noted, by writing A_{LL} in this way we are assuming that all acceptance and efficiency corrections are helicity and crossing independent. The detector acceptance and reconstruction efficiencies do not change on the scale of hundreds of nanoseconds, which is the typical time between helicity flips in RHIC. Therefore, this assumption is safe. In the case of the trigger efficiency, this assumption does not hold due to the design of the trigger circuit: odd and even crossings use separate circuits due to the trigger reset time of ~ 140 ns being longer than the time between bunches, and these separate circuits can

have different effective thresholds. The analysis is therefore done separately for odd and even crossings for $p_T < 7$ GeV/c. Above this p_T, the triggers are maximally efficient and there is no observed dependence on the trigger circuit.

Similarly, for R, we do not measure the luminosity recorded in each helicity state, but instead the number of MB triggered events, again assuming that efficiency and acceptance cancel in the ratio. The accuracy of this assumption, as well as the assumption that the MB trigger has no inherent asymmetry, are discussed in Chapter 4. The latter leads to the largest systematic uncertainty in the determination of A_{LL}.

As seen in Fig. 3.1, the two-photon mass yield in the π^0 mass peak region (solid raspberry shading) consists of both signal and background. The asymmetry measured in this region, A_{LL}^{S+B}, contains both the signal asymmetry, A_{LL}^{S}, and the asymmetry in the background component, A_{LL}^{B}. The relationship between these three asymmetries in the mass peak region can be written as

$$A_{LL}^{S} = \frac{A_{LL}^{S+B} - w_{BG} A_{LL}^{B}}{1 - w_{BG}} \tag{3.7}$$

where w_{BG} is the background fraction in the peak region. For the π^0, we define the peak region as $112 < m_{\gamma\gamma} < 162$ MeV/c^2, which corresponds to roughly 2σ about the mean of the mass peak at low p_T. The peak position does not correspond exactly to the known mass values for the mesons due to energy smearing effects in the EMCal.

The background fraction w_{BG} is extracted from a fit to the mass range near the π^0 mass peak of 50$-$300 MeV/c^2. The fit function is a Gaussian to describe the mass peak and a third order polynomial to describe the background. w_{BG} is defined as the integral of the background polynomial in the mass peak range $[m_1, m_2]$ divided by the total yield in this same range:

$$w_{BG} = \frac{\int_{m_1}^{m_2} (a + bm + cm^2 + dm^3)}{\text{binwidth} * \text{Yield}_{[m_1,m_2]}}. \tag{3.8}$$

Variations of the initial fit parameters and range showed no significant modification to w_{BG} except in the 12$-$15 GeV/c p_T bin, where modifying the binning led to a 5% change in $A_{LL}^{\pi^0}/\sigma_{A_{LL}^{\pi^0}}$, attributable to the difficulty in fitting the low-statistics background in this p_T range (see Subsection 3.5.2). Average background fractions for the different p_T bins are listed in Tables A.1 and A.2.

The background asymmetry in the peak region cannot be directly measured, but if the background asymmetry is constant as a function of $m_{\gamma\gamma}$, then a measurement in the sideband regions on either side of the peak can be used instead. Figure 3.2 shows the asymmetry as a function of mass in the back-

ground region near the π^0 peak for several p_T bins. No indication of a mass dependence in the background asymmetry is seen. However, as discussed in Subsection 3.5.5, a small systematic uncertainty is evaluated for $A_{LL}^{\pi^0}$ to account for any mass dependence. To include any possible mass dependence, as well as to increase the statistics of the background asymmetry , the yields in sidebands on both sides of the peak region are summed to calculate background asymmetry. The sideband regions are shown in Fig. 3.1 in blueberry, and are defined as $47 < m_{\gamma\gamma} < 97$ MeV/c^2 and $177 < m_{\gamma\gamma} < 227$ MeV/c^2.

Yields for peak and sideband regions as well as background fractions can be found in Tables A.1 and A.2 in Appendix A.3.

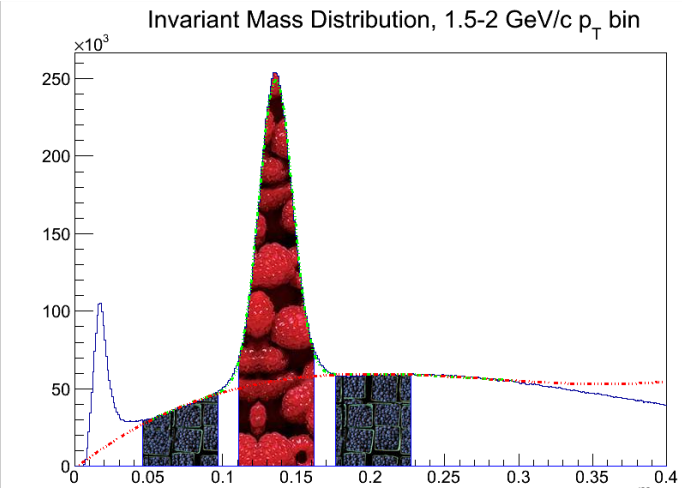

Figure 3.1: Two photon invariant mass distribution. Raspberry area, 112 MeV$< M_{\gamma\gamma} <$ 162 MeV/c^2, is used for π^0 plus background asymmetry measurements ($A_{LL}^{\pi^0+BG}$); Blueberry, 47 MeV/c^2 $< M_{\gamma\gamma} <$ 97 MeV/c^2 and 177 MeV/c^2 $< M_{\gamma\gamma} <$ 227 MeV/c^2, for A_{LL}^{BG}

A_{LL}, as written in Eq. 3.4, is calculated for peak and background sidebands in each RHIC fill. Due to the variation in trigger electronics discussed above, the analysis is done separately for even and odd crossings. For each of the four spin patterns, A_{LL}^{S} is calculated using Eq. 3.7 with the statistically-weighted-average over fills of A_{LL}^{S+B} and A_{LL}^{B}. The eight results (four spin patterns for even crossings and four spin patterns for odd crossings) are compared for consistency, and then combined to arrive at the final A_{LL}^{S}.

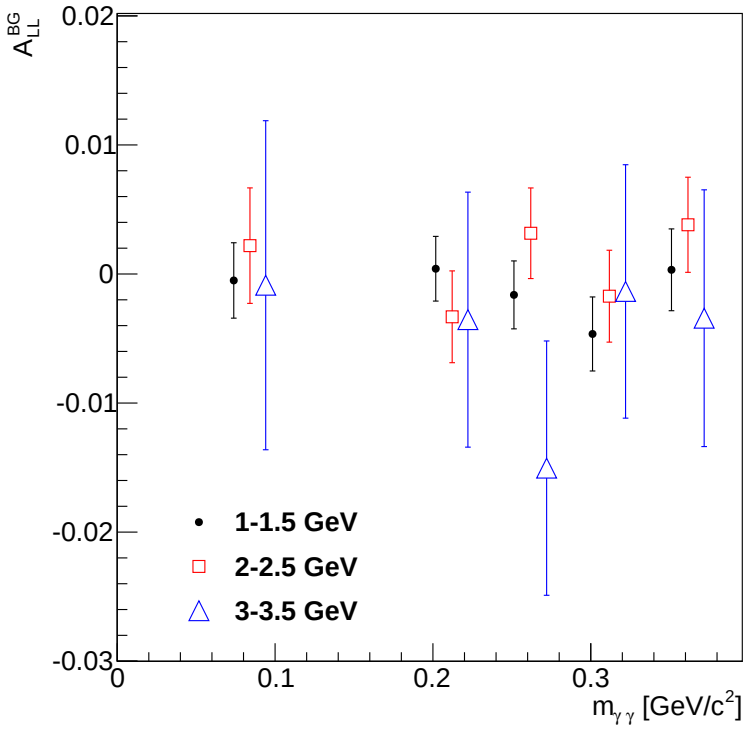

Figure 3.2: A_{LL} vs. $m_{\gamma\gamma}$ for the background region near the π^0 mass peak for three p_T bins: $1-1.5$ GeV/c (black circle), $2-2.5$ GeV/c (red square) and $3-3.5$ GeV/c (blue triangle), for a single spin pattern in odd crossings. The peak region A_{LL} is not shown. No $m_{\gamma\gamma}$ dependence is found.

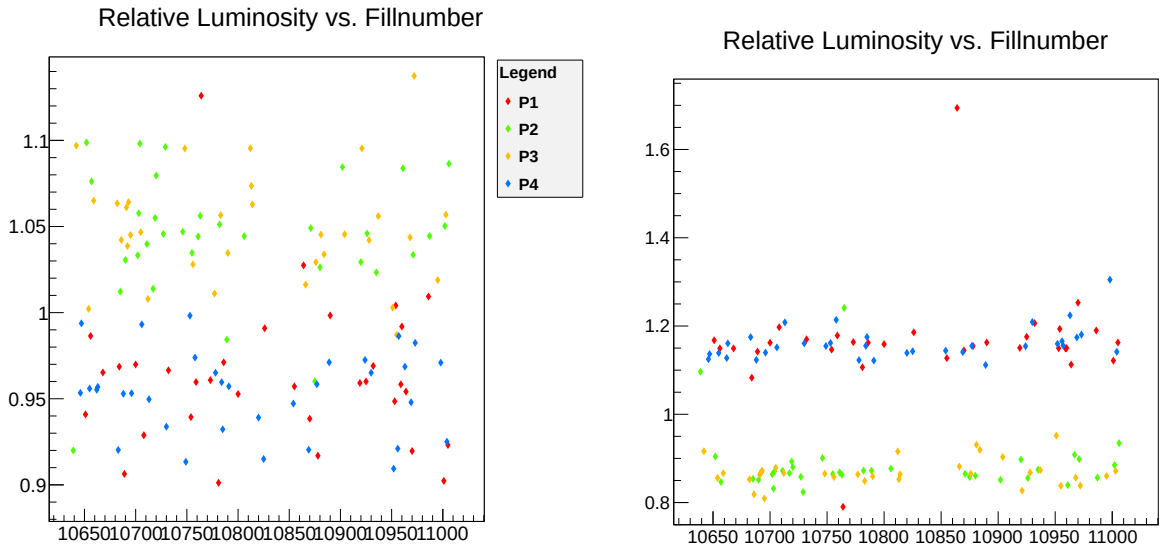

(a) **(b)**

Figure 3.3: Relative Luminosity vs. fill number as measured by the BBCs for (a) even and (b) odd crossings separately for each spin pattern: P1 = Red, P2 = Yellow, P3 = Green, P4 = Blue.

3.2.1 Relative Luminosity

Relative luminosity is calculated as the ratio between the number of BBC triggered events in same helicity crossings to the number in opposite helicity crossings. In order to correspond to the binning of the EMCal cluster data, it is separated into even and odd crossings. Figure 3.3 shows relative luminosity as a function of fill number for odd and even crossings separately.

3.2.2 Polarization

Polarization, as measured by the p-Carbon polarimeter and normalized to the H-jet polarimeter over the entire running period (see 2.1.3), is provided to the experiments by the CNI-pol group. For 2009 $\sqrt{s} = 200$ GeV running, the average beam polarizations were 56% for the Blue beam and 55% for the Yellow beam, for a product $P_B P_Y = 0.31$. The overall relative scale uncertainty on the product $P_B P_Y$ was 6.5%, with 4.8% of that considered correlated with other RHIC running years. The fill-by-fill values and uncertainties can be found in [38]. Only fill-by-fill statistical uncertainties and the systematic global scale uncertainty are included in the analysis. The fill-by-fill uncorrelated system-

atic uncertainty in Run9 200 GeV was 7.2% for both beams. It is mostly yellow-blue beam correlated so for a double-spin asymmetry it becomes more like 14.4% for the product $P_B P_Y$. With 135 fills in the Run9 analysis, this 14.4% scales as $14.4\%/\sqrt{135} \approx 1\%$ when compared to the global systematic uncertainty on $P_B P_Y$ of 8.8%, and so we may neglect it for convenience. Figure 3.4 plots each beam polarization vs. runnumber, using the fill-by-fill values along with the decay rates provided by the CNI-pol group. The changes in polarization from fill to fill are much larger than the run-to-run changes within a fill, motivating the division of the analysis into fill-groups.

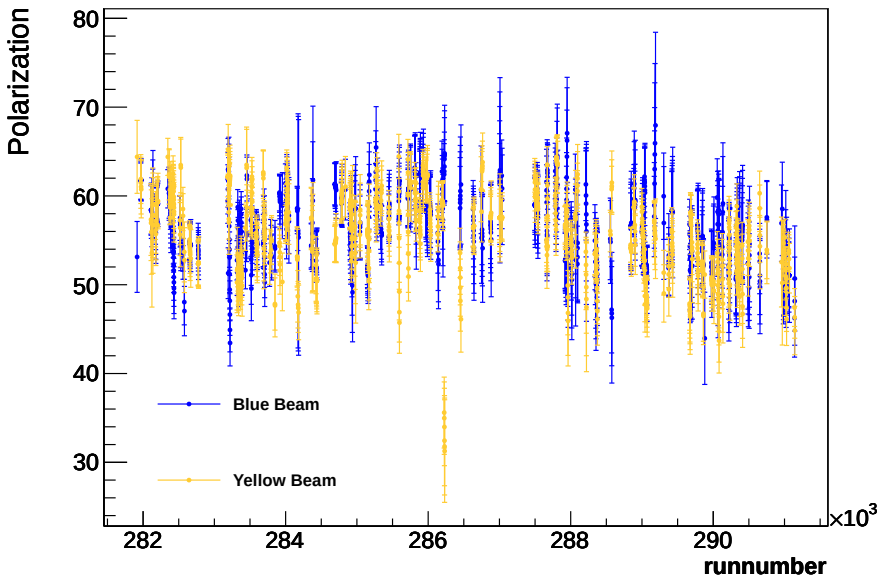

Figure 3.4: Polarization of each beam vs. runnumber, with statistical uncertainty, which was calculated from the fill-by-fill polarization values and polarization decay rates provided by the CNI-pol group. The deviation from fill-to-fill is much larger than the decay from run to run within a fill.

3.2.3 Local Polarimetry Scaling

For the 2009 RHIC run at $\sqrt{s} = 200$ GeV, the fraction of the polarization in the transverse direction, $f = P_T/P$, was measured to be

- $f_L^B = 0.994 + \frac{+0.006}{-0.008}(\text{stat}) + \frac{+0.003}{-0.010}(\text{syst})$ for the blue beam and
- $f_L^Y = 0.974 + \frac{+0.014}{-0.018}(\text{stat}) + \frac{+0.019}{-0.035}(\text{syst})$ for the yellow beam

where the systematic uncertainty comes from considerations of detector acceptance and imprecise knowledge of the collision axis with respect to the ZDCs.

Given these numbers, we must scale our final $A_{LL}^{\pi^0}$ by a factor 1.03 and include an additional global scaling uncertainty of

$$\sqrt{\left(\frac{\delta f_L^B}{f_L^B}\right)^2 + \left(\frac{\delta f_L^Y}{f_L^Y}\right)^2} = \sqrt{\left(\frac{\frac{+0.007}{-0.013}}{0.994}\right)^2 + \left(\frac{\frac{+0.024}{-0.039}}{0.974}\right)^2} = \frac{+2.6\%}{-4.2\%} \tag{3.9}$$

where combining of the asymmetric errors has been done by treating the + and − errors separately and assuming the systematic error is uncorrelated between the blue and yellow beam.

3.2.4 Uncertainties on Counting

Prescales

Some data taken in the 2009 run had the ERT triggers prescaled. We therefore scale up all counts taken during these runs by a factor $a \equiv \text{prescale} + 1$. To illustrate the range of possible uncertainties when counting a prescaled quantity, we present the following extremes:

- Consider a counting experiment in which the experimenter counts events passing a specific selection criteria "by twos", that is, for every second event passing the criteria, the experimenter records one tally mark. At the end of the experiment, if the experimenter has exactly N tally marks, she knows that there were either $2N$ or $2N + 1$ events passing the selection criteria. Given Poisson statistics, the statistical uncertainty on the number of events passing the criteria is (neglecting the +1) $\sqrt{2N}$.

- Now take the case where the experimenter again records "by twos" events passing some selection criteria, but this time looks within said events to find N events passing an additional, completely uncorrelated criteria. An example would be counting with a prescale "events coinciding with a clock tick" and then looking within this sample for "events with a π^0." In this case, the uncertainty on the number of events that would have passed the second selection without the initial prescale would be $2\sqrt{N}$. This is because the prescale and our measurement N in the prescaled sample have no correlation, and so we cannot combine the information to reduce the relative error.

So we see that when up-scaling counts taken with a prescale, how we handle the uncertainty depends on to what extent our first and secondary selection criteria are correlated.

In this analysis, we have taken for our run-by-run counting uncertainties the conservative estimate of $a\sqrt{N}$. That this overestimates the statistical uncertainty can be seen by comparing the bunch shuffling plots of Subsection 3.5.7 for 4×4c triggers with 4×4a triggers, the latter of which was never prescaled in the 2009 run.

Event Multiplicity Uncertainty Enhancement Factor

To be consistent with previous A_{LL} analyses in PHENIX, an uncertainty enhancement factor, referred to internally as a "k-factor," is used to account for cluster pair multiplicities in a given event. The standard derivation is as follows: we have some number of cluster pairs, $N_{\gamma\gamma}$, and we wish to find the uncertainty on this number. It can be related to the number of events N_{ev} via

$$N_{\gamma\gamma} = \sum_{i=1}^{N_{ev}} k_i = \bar{k} N_{ev}, \tag{3.10}$$

where k_i is the pair multiplicity in each event, and $\bar{k}$ is the average multiplicity over all events. Then, assuming the number of events and the multiplicity per event are uncorrelated, linear error propagation gives

$$\sigma^2_{N_{\gamma\gamma}} = N^2_{ev}\sigma^2_{\bar{k}} + \bar{k}^2\sigma^2_{N_{ev}}. \tag{3.11}$$

This may not be a good assumption if the event trigger shares some requirement with the cluster pair selection, which it does in our case: one cluster in each pair is required to have been capable of triggering the event. In this case, a higher average multiplicity per event means the trigger is more likely to fire on each collision and we should accumulate a greater number of events, a clear correlation. Still, we will proceed with it, since it turns out to be a more conservative choice and also to keep in line with previous analyses. An alternate derivation, which arrives at a much different conclusion, is given in Appendix A.1 Now we need $\sigma^2_{\bar{k}}$ which is equal to $\frac{1}{N_{ev}}\sigma^2_k$. Using also simple poisson statistics for N_{ev}, i.e. $\sigma^2_{N_{ev}} = N_{ev}$, Eq. 3.11 becomes

$$\sigma^2_{N_{\gamma\gamma}} = N_{ev}\sigma^2_k + \bar{k}^2 N_{ev} = N_{ev}(\bar{k}^2 + \sigma^2_k). \tag{3.12}$$

Using the definition of the variance,

$$\sigma_k^2 = \bar{k^2} - \bar{k}^2, \tag{3.13}$$

Eq. 3.12 can be rewritten

$$\sigma_{N_{\gamma\gamma}}^2 = N_{ev}\bar{k^2}, \tag{3.14}$$

and using the relation $N_{ev} = N_{\gamma\gamma}/\bar{k}$, we find

$$\sigma_{N_{\gamma\gamma}} = \sqrt{\frac{\bar{k^2}}{\bar{k}} N_{\gamma\gamma}}. \tag{3.15}$$

3.3 EMCal Clusters

A variety of variables are stored for "clusters" in the EMCal, which are groups of neighboring towers sharing the energy distributed by some particle traversing the detector. A typical electromagnetic cluster is completely contained within a 3×3 array of towers. For each cluster, the information stored includes

- The x, y, and z position of the cluster,
- The total energy of the cluster including a correction assuming the cluster shape is electromagnetic,
- The Time of Flight (ToF) of the cluster as measured by the EMCal,
- The probability that the cluster is a photon, based on the agreement of the cluster profile with that expected for a true electromagnetic shower, and
- The distance from the cluster to the nearest hit in the PC3, in cylindrical coordinates (z and ϕ).

Two of these quantities, the energy and ToF, require offline calibration after the data has been recorded to adjust for gain and timing settings of the detector.

3.3.1 Warn/Deadmap

Hot (noisy) and dead towers, as well as towers with failed energy calibration are excluded from the analysis. In particular, towers on the outer edge of each sector are not calibrated and are thus excluded.

Any cluster centered on an excluded tower is excluded from the analysis. Thus, in order to prevent a cluster centered on a good tower but extending into a bad tower from being analyzed, a 3x3 block centered on each primary excluded tower is also excluded. 3x3 was chosen because a typical photon shower is not more than three towers in diameter. Table 3.1 lists the non-edge and edge excluded towers by sector. In all, ∼10% of the non edge EMCal was masked.

sector	masked non-edge towers	masked edge towers	total towers
W0	169 (6%)	416 (16%)	2592
W1	104 (4%)	416 (16%)	2592
W2	199 (7%)	416 (16%)	2592
W3	379 (15%)	416 (16%)	2592
E0	940 (20%)	560 (12%)	4608
E1	270 (6%)	560 (12%)	4608
E2	332 (13%)	416 (16%)	2592
E3	171 (7%)	416 (16%)	2592
PbSc	1364 (9%)	2496 (16%)	15552
PbGl	1210 (13%)	1120 (12%)	9216
Total	2574 (10%)	3616 (15%)	24768

Table 3.1: Number of non-edge (hot, dead and uncalibrated) and edge masked towers from the warn map study. The number in parenthesis is the percentage of the total.

3.4 Cuts

3.4.1 Shower Profile Cut

In reconstruction, the distribution of a cluster's energy across EMCal towers is compared to the expected distribution of a photon, and the result of this comparison is stored in a variable named "prob photon." Values closer to one indicate better agreement with the expected distribution; hadron showers are likely to have a value near zero. In this analysis, as in previous π^0 cross section and A_{LL} analyses, we cut clusters with "prob photon" < 0.02, in both the PbSc and PbGl.

3.4.2 Minimum Cluster Energy

A minimum energy cut is applied to all clusters to reduce combinatorial background from very low energy clusters. In all analyses from 2003 to 2006, clusters with energy below 0.1 (0.2) GeV in PbSc (PbGl) were discarded. It is the same here.

3.4.3 Time of Flight

A particular hardware-based effect that became apparent with increases in the instantaneous luminosities delivered to the experiments in 2009 involved the readout electronics for the EMCal. When a trigger fires, the signal in each EMCal tower is compared with an analog-buffered value from 424 ns, or four crossings, earlier. Due to the long decay time of an EMCal signal, any energy deposit occurring in the three previous crossings is read out. Pileup is negligible due to the fine lateral segmentation of the EMCal, so only the combinatorial background is affected. In the 2009 run, the likelihood for a collision in at least one of three previous crossings was significant at about 22%. One cut in particular that can reduce this effect is the ToF cut.

The ToF for a given EMCal cluster is given relative to t_0, the initial time of the collision as measured by the BBC. Photon candidates in this analysis are required to reach the EMCal within $^{+8}_{-6}$ ns of the expected ToF for a photon, which removes low energy hadrons and other out of time clusters but also reduces the contribution of clusters from previous crossings. Although the circular buffering in the EMCal readout makes the ToF measurement insensitive to timing offsets that are multiples of the beam-crossing period, the fact that different crossings have independent t_0 effectively smears the ToF distribution. This is the dominant effect in increasing the likelihood of previous-crossing clusters to have a ToF outside the cut window.

This background can be studied in more detail by analyzing specific sets of crossings that follow one- or two-bunch empty crossings and therefore contain a smaller number of previous-crossing clusters. We define the following crossing selections for study based on the number of previous crossings that can contribute clusters given a four-crossing (current plus three) memory:

- +0: The three previous crossings are empty
- +1: One of the three previous crossings is filled
- +2: Two of the three previous crossings are filled
- +3: All three previous crossings are filled.
- +3*b*: Same as +3 but spaced further from empty crossings.

Figure 3.5 shows the efficiency of (fraction of events passing) the ToF cut on the various selections. The efficiency decreases as the selection moves away from the empty crossings and the previous-crossing cluster background increases, indicating that the ToF cut is more effective at removing this specific type of background than the total background. Also, from selection +0 to +3, the relative efficiency in the π^0 peak region decreases by about 0.5% compared to a decrease of roughly 3% in the high mass background efficiency. The smaller change for the peak region is due to the trigger cut (see next section) removing true mesons from previous crossings. As expected, there is no significant change in cut efficiency between selections +3 and +3*b* since the buffer encompasses only three previous crossings.

3.4.4 Charge Veto

Another method to remove charged hadrons is to veto photon candidates with associated (charged particle) hits in the PC3. However, in order not to unnecessarily remove real photons that pair-converted before the EMCal, but outside of the magnetic field, a special cut was developed for the 2003 analyses [20] and re-evaluated for the 2009 analysis.

We define two vectors: (1) the vector starting at the event vertex and pointing to a cluster in the EMCal and (2) the vector pointing from the vertex to the nearest hit in the PC3. The angle between these vectors is defined as θ_{CV}, the charge veto angle. The diagram in Fig. 3.6 shows schematically how this angle is defined for three distinct cases, which can be classified according to the relative magnitude of θ_{CV}:

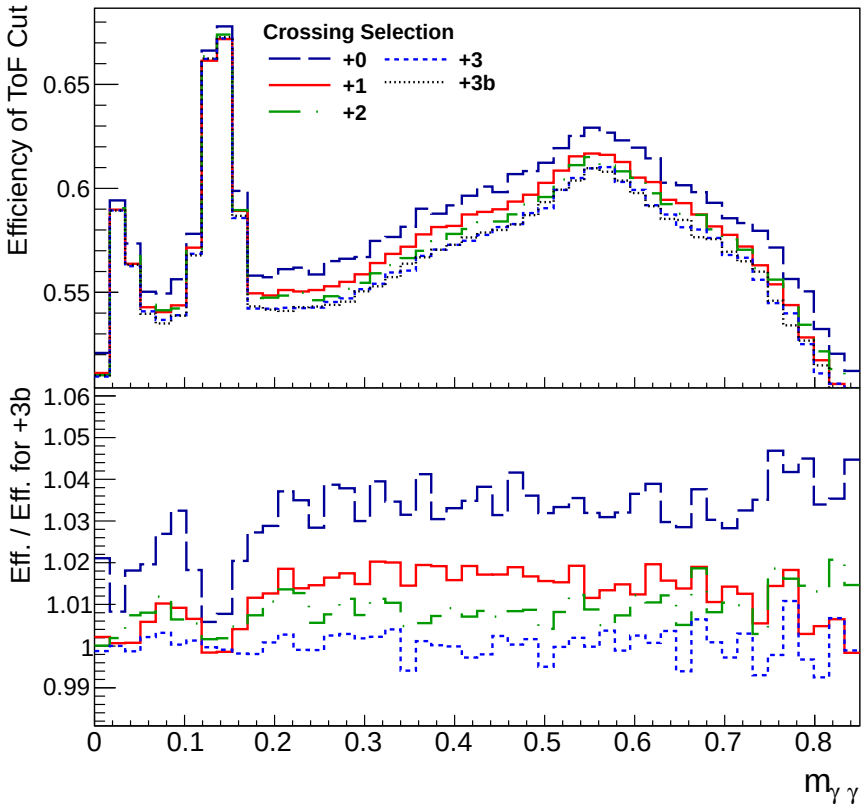

Figure 3.5: (a) Efficiency of ToF cut, with the minimum energy, trigger, and offline z-vertex cuts already applied, for different crossing selections defined in the text, and for a p_T range of $2-4$ GeV/c. The energy asymmetry cut has not been applied here, and the decreased efficiency in the higher mass region is due to the larger background fraction. (b) Ratio of the histograms in (a) to the histogram with crossing selection +3b.

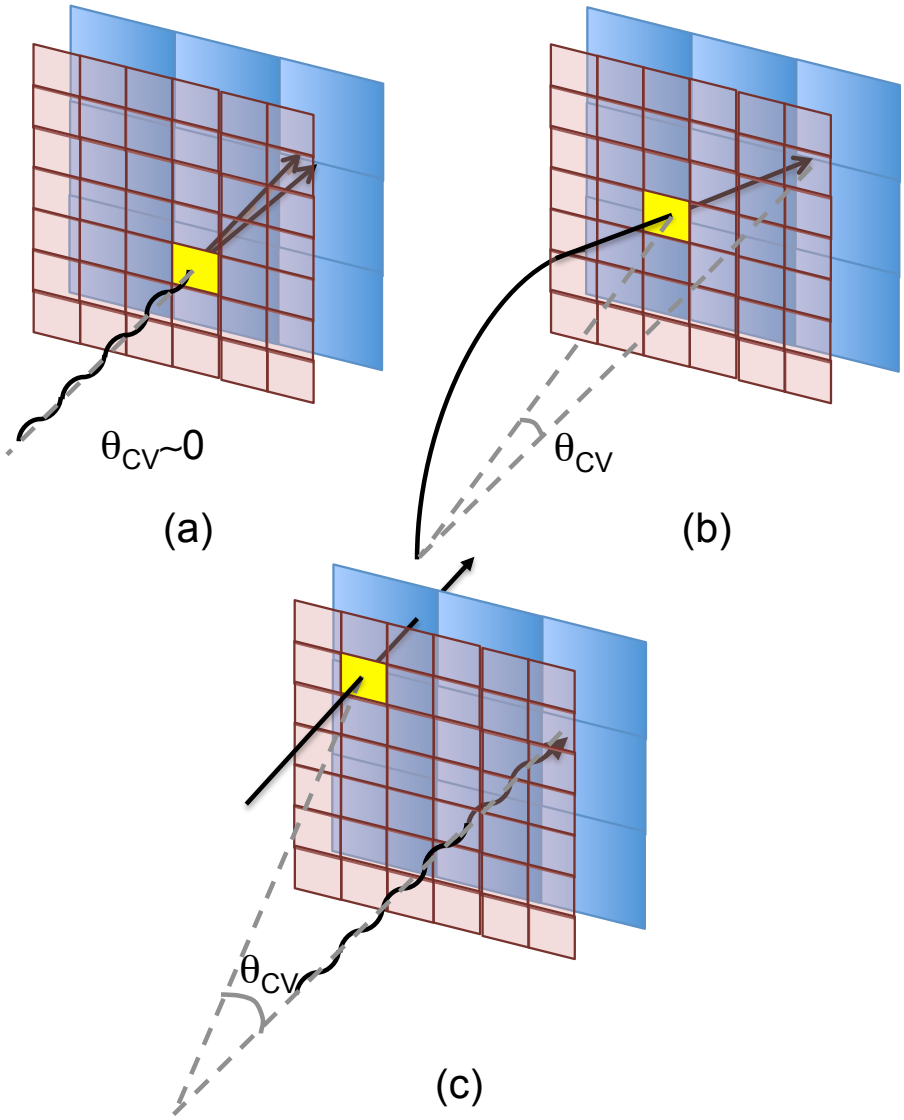

Figure 3.6: Schematic (not to scale) of the hits in the PC3 (transparent grid) and the related θ_{CV} from three particle classes which leave clusters in the EMCal (solid grid behind PC3): (a) photons which convert outside on the magnetic field prior to the EMCal, and have very small θ_{CV}, (b) charged hadrons which bend in the magnetic field, and so have moderate sized θ_{CV}, and (c) photons which do not convert, and are randomly associated with a different particle's PC3 hit, and therefore are likely to have large θ_{CV}. Courtesy of Kieran Boyle.

1. Small θ_{CV}: e^+e^- pairs from photon conversions outside of the magnetic field region can still form a single cluster if their opening angle or the conversion's distance from the EMCal is small. In this case we may find an associated PC3 hit directly in front of the cluster, but we can still reconstruct the original photon from the energy deposited. Thus we should retain clusters with small θ_{CV}.

2. Moderate θ_{CV}: For hadrons that travel through (and bend in) the inner magnetic field region, it is not possible to draw a straight line connecting the EMCal cluster, PC3 hit and collision vertex. Thus there will be some finite θ_{CV} associated with these particles which we wish to exclude from the analysis.

3. Large θ_{CV}: The phase space for combinatorial association of an EMCal cluster with an unrelated PC3 hit increases linearly with $tan(\theta_{CV})$. Thus random association dominates this region and we should not throw out these clusters.

To exclude clusters associated with PC3 hits from hadrons while retaining photons which convert near the EMCal, an energy dependent cut based on the θ_{CV} is applied.

After applying all other cluster cuts to PbSc clusters, each reconstructed pair invariant mass was assigned to the (energy, θ_{CV}) bin of both of its clusters, and a θ_{CV} interval was chosen as a function of cluster energy such that the exclusion of PbSc clusters in this interval minimized the statistical uncertainty on π^0 A_{LL}. The resulting θ_{CV} intervals are shown in Fig. 3.7 for clusters in the PbSc. Due to their decreased response to hadrons, no additional benefit for the charge veto cut on top of the other cuts was found for the PbGl sectors, and thus no charge veto cut was applied to those.

The invariant mass distribution near the π^0 mass peak reconstructed using clusters in the PbSc is shown in Fig. 3.8 for different θ_{CV} requirements. It is clear that the signal to background for π^0 is significantly larger for clusters with a moderate θ_{CV}, due to hadron contamination in the photon candidates.

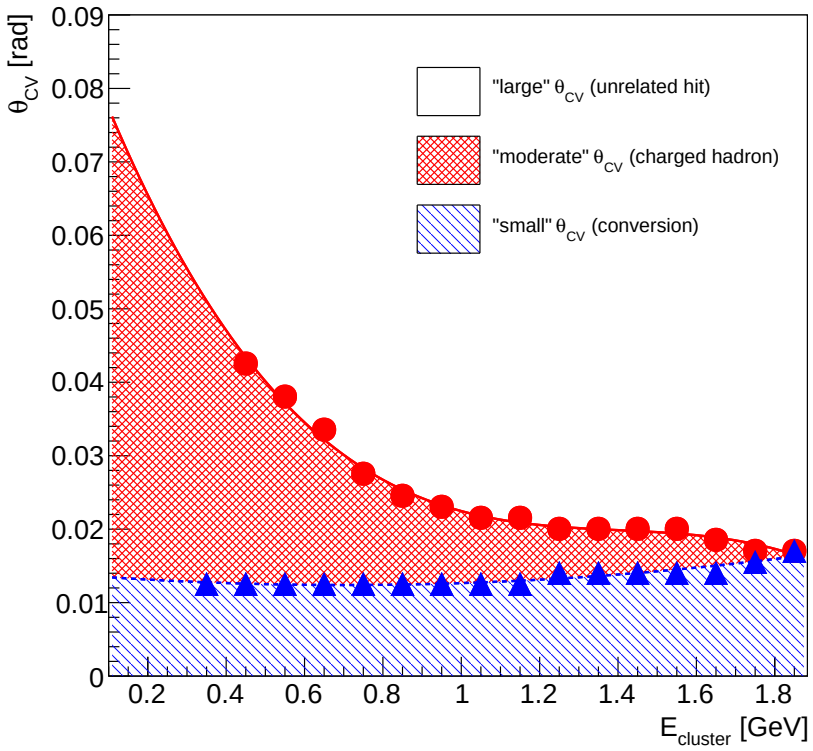

Figure 3.7: θ_{CV} as a function of cluster energy in the EMCal PbSc. Clusters in the red cross-hatched region are excluded from the analysis. For $E_{\text{cluster}} > 1.9$ GeV, no distinction between the regions is possible due to the inverse relationship between bend radius and energy for hadronic tracks.

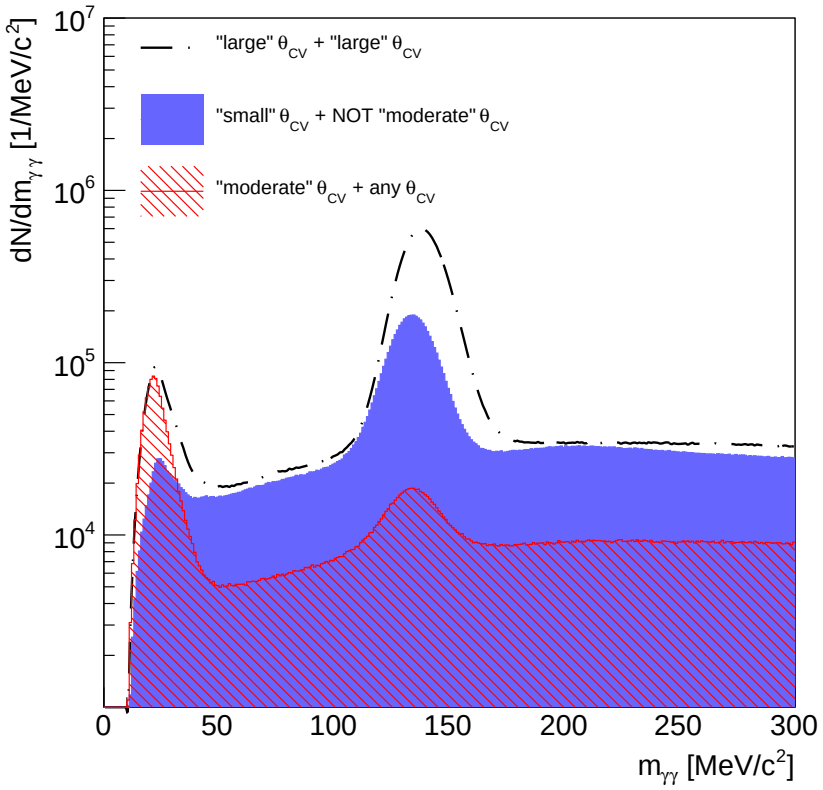

Figure 3.8: Yield of cluster pairs for different θ_{CV} requirements as a function of invariant mass (calculated assuming both clusters are photons), in the PbSc only and for $E_{cluster} < 1.9$ GeV.

3.4.5 Trigger

As we are using a triggered data set, we must be sure that we understand our trigger bias. In other words, we want to avoid counting π^0s in $p+p \to \pi^0+C+X$ events where C is some other particle or particles and C fires the trigger. Unless inclusive $C + \pi^0$ production has the same asymmetry as inclusive π^0 production, counting such events would pollute our asymmetry measurement. We should require that the π^0 itself triggered the event, but in practice we make the weaker requirement that the ERT supermodule containing the central tower of the higher energy cluster in each pair has the ERT4x4c (below $p_T = 4$ GeV/c) or ERT4x4a (above $p_T = 4$ GeV/c) trigger bit set. This requirement has been shown to be equivalent to requiring the π^0 trigger the event, and the same procedure has been followed in all previous π^0 cross section and A_{LL} measurements.

3.4.6 Minimum Statistics

The highest p_T bins are larger than 1 GeV/c wide so that there are enough statistics to assume Gaussian uncertainties in the calculations. For the "peak" region calculation, fills where

$$N_{++} + N+- < 30 \tag{3.16}$$

for a given (even/odd,p_T) bin were excluded from that bin's analysis. The cut was done this way so that, with high probability, N_{++} and $N+-$ would have more than 10 counts each and be distributed according to Gaussian statistics. Cutting instead on $N_{++} < 10||N_{+-} < 10$ could introduce bias because it would preferentially cut fills where, for instance, the helicity with lower production rate fluctuated downward. For the "sideband" region calculation, the condition for exclusion was

$$N_{++} < 1||N_{+-} < 1 \tag{3.17}$$

in order to avoid divide-by-zero errors in the uncertainty calculations. At high p_T where sideband counts drop below 10 per fill, the background fraction is small enough that we need not worry about the deviation from Gaussian statistics. Note that fills were allowed to be analyzed for the sideband calculation but not the peak, and vice-versa.

3.5 Systematic Uncertainties/Cross-Checks

3.5.1 Event Overlap in EMCal Readout

Before the time of flight cut was applied, there was some systematic difference between the different fill patterns in the fill-by-fill A_{LL}s, especially at low p_T. The effect was more pronounced in the background than in the signal data. We attribute this effect to the way in which the EMCal stores cluster energy information. The effect was not noticeable in the 2005 and 2006 runs due to the lower luminosities.

The EMCal effectively stores cluster energy information for four crossings. When an event is written out, all clusters from the current beam crossing are recorded as well as those from any of the previous 3 crossings. This means that the combinatorial background includes di-photon pairs where one photon may be from a previous crossing (the cut in Subsection 3.4.5 insures that the higher energy photon comes from the current crossing). As the luminosity increases, the likelihood of an EMCal energy deposit in one of the previous crossings increases and thus so does this combinatorial background.

On average, these previous "ghost" clusters will contribute equally to each bunch crossing, as long as the bunches preceding each bunch share the same characteristics. But with the typical empty bunches in the collider, a select few filled bunches see fewer "ghost" clusters than others. Luminosity fluctuations correlated to specific bunches could also cause a systematic difference in the number of ghost clusters for each bunch, although at a much smaller level. Thus we consider only the effect of the first case, empty bunches, on the asymmetries.

To understand how empty bunches can affect asymmetries, consider the first eight bunches (0-7) after the abort gap in a fill. For now assume a spin pattern of $+-+--+-+$ for the blue beam and $++--++--$ for the yellow beam (RHIC spin pattern P1). There should be no collisions in the abort gap, and so crossing 0 will only have clusters from crossing 0, i.e. no "ghost" cluster background. Crossing 1, on the other hand, will inherit "ghost" clusters from crossing 0. Crossing 2 will have contributions from crossings 0 and 1. Crossings 3-8 will all have "ghost" clusters from three previous crossings. If there is no inherent asymmetry, then in each crossing we would expect to measure N_{real} clusters. In addition, each crossing will have on average N_{ghost} clusters from any of the previous three crossings that are filled. Then we have, before the trigger bit check, $N_{real}(N_{real}-1)$ pairs in crossing 0, $(N_{real}+N_{ghost})(N_{real}+N_{ghost}-1)$ for crossing 1, $(N_{real}+2N_{ghost})(N_{real}+2N_{ghost}-1)$ for crossing 2, and $(N_{real}+3N_{ghost})(N_{real}+3N_{ghost}-1)$ for crossings 3-8. If our relative luminosity detector does not suffer the same effect, then it is obvious that we

will see a significant false asymmetry. In this simple case, the false asymmetry would be $4N_{ghost}/N_{tot}$. If the spin pattern were P2 (blue: $--++--++$, yellow: $++--++--$), then the asymmetry would be negative with the same magnitude. Thus, for this effect we should find that patterns P1 and P4 (P4 is P1 with both beams' patterns flipped) should have the same false asymmetry. P2 and P3 should also share the same asymmetry, the negation of that for P1 and P4.

In Run 9, bunches 38, 39, 78, 79, and 111-119 were either empty-empty or empty-filled. Therefore bunches 0-3, 40-43, and 80-83 would see varying amounts of ghost clusters. As the spin pattern is a multiple of 8, and these bunches are separated by 40 bunches, the impact on the asymmetry goes according to the above example.

The spin pattern in RHIC is cycled with each new fill between the four possible patterns. Thus, to avoid mixing these false asymmetries, we do four separate analyses for the four groups of fills. This way we ensure that we are subtracting the correct A_{LL}^{BG} from $A_{LL}^{\pi^0+BG}$ when we calculate the final result. After subtracting the sideband asymmetries, the results for are consistent within statistical uncertainties.

3.5.2 Rebinning Study

To investigate the robustness of the background fraction calculation, the entire final analysis was re-run with the binwidth doubled in every invariant mass histogram. The one and only component of the analysis affected by this change is the fit to the π^0 mass peak, which enters the calculation through Equation 3.8. Table 3.2 lists the result. The impact is negligible, even in the last bin where it is largest but only 2.1% of the statistical uncertainty.

p_T bin (GeV/c)	$\Delta A_{LL}^{\pi^0}/\delta A_{LL}^{\pi^0}$
1-1.5	0.00%
1.5-2	−0.01%
2-2.5	0.00%
2.5-3	0.00%
3-3.5	0.00%
3.5-4	0.00%
4-5	−0.01%
5-6	0.07%
6-7	0.13%
7-9	−0.19%
9-12	−0.36%
12-15	2.10%

Table 3.2: Change, relative to the statistical uncertainty, in final $A_{LL}^{\pi^0}$ values from a doubling of the binwidth in all invariant mass histograms.

3.5.3 p_T Smearing Study

To test the effects of p_T smearing from the energy resolution of the EMCal, we can take a functional form for A_{LL} such as the DSSV08 fit (see Chapter 5) and apply a p_T dependent Gaussian smearing. To determine the degree of p_T smearing to apply, we relate the π^0 p_T to the individual EMCal cluster energies:

$$\begin{aligned} p_T^{\pi^0} &\approx E_{\gamma_1} + E_{\gamma_2} = 2\langle E_\gamma \rangle, \\ \frac{\delta p_T^{\pi^0}}{p_T^{\pi^0}} &\approx \frac{1}{\sqrt{2}} \left(\frac{\delta E_\gamma}{E_\gamma} \right), \end{aligned} \tag{3.18}$$

where we have neglected the longitudinal momentum of the clusters, a reasonable assumption in the central arm EMCal. Then, taking the nominal energy resolution for the PbSc given in [15] of

$$8.1\%/\sqrt{E[\mathrm{GeV}]} \bigoplus 2.1\% \tag{3.19}$$

and using Equations 3.18 we get a π^0 p_T resolution of

$$8.1\%/\sqrt{p_T[\mathrm{GeV/c}]} \bigoplus 1.5\% \tag{3.20}$$

The smearing can then be applied by multiplying this relative uncertainty by p_T and using it as the standard deviation in a Gaussian distribution,

$$A_{LL}p'_T = \frac{\int dp_T N(p_T) G(p_T - p'_T) A_{LL}(p_T)}{\int dp_T N(p_T) G(p_T - p'_T)}, \tag{3.21}$$

where $N(p_T)$ gives the p_T spectrum. The results of such a smearing applied to the DSSV08 global analysis result for $A_{LL}^{\pi^0}$ are shown in Figure 3.9. The smearing has a negligible effect when compared to the DSSV08 uncertainty band.

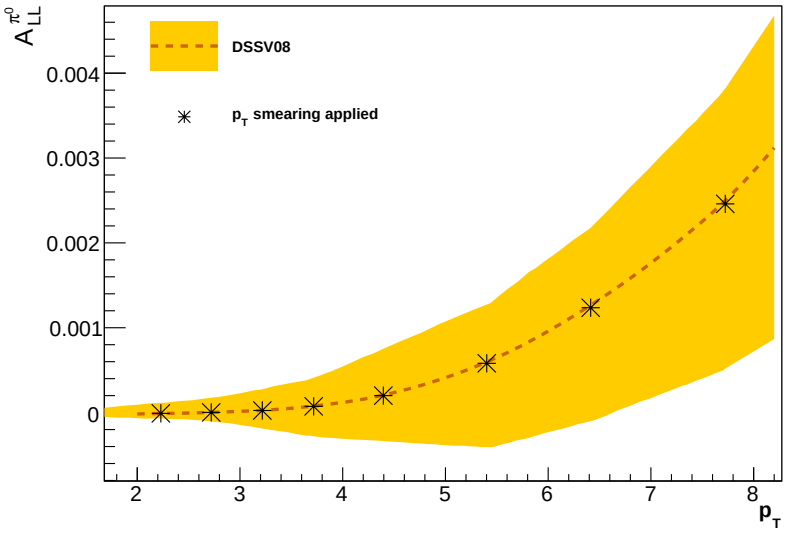

Figure 3.9: A sampling of points from the p_T-smeared DSSV08 best-fit along with the original DSSV08 best-fit and uncertainty band. The difference is too negligible to discern on the plot.

3.5.4 Single Spin Asymemtries

A single spin asymmetry is defined as

$$A_L \equiv \frac{\sigma_+ - \sigma_-}{\sigma_+ + \sigma_-} \quad R = \frac{L_+}{L_-} \tag{3.22}$$

and is calculated using

$$A_L = \frac{1}{P_{Beam}} \frac{N_+ - RN_-}{N_+ + RN_-} \quad R = \frac{L_+}{L_-} \tag{3.23}$$

where σ_+ (σ_-) is the cross section of positive (negative) helicity bunches for one beam (the other beam is summed over) and P_{Beam} is the polarization for that beam. If the collider is filled such that there is a net correlation between the two beams' spins, a double-spin asymmetry contribution would be introduced. This is not the case for, e.g., the blue beam if

$$R_{++\text{to}+-} = R_{-+\text{to}--} = 1, \tag{3.24}$$

where the blue beam is listed before yellow in the indices. This is close enough to the reality in RHIC. Note that the spin pattern was changed in the 2006 Run and beyond so that A_L is always measurable, which was not the case in the 2005 Run.

The analysis is similar to the A_{LL} analysis, with Eq. 3.23 substituted for Eq. 3.4. The final results are given in Appendix A.4 and Tables 3.3 and 3.4. The consistency of these asymmetries with zero is an important cross-check, since finiteness would indicate parity violation of the strong force, which has so far never been observed.

3.5.5 Difference Between Sideband Asymmetries

The asymmetry in the background under the π^0 mass peak cannot be measured directly. Therefore, the asymmetry in the sideband regions shown in blueberry in Fig. 3.1 is measured and assumed to have an A_{LL} equal to that of the background under the π^0 mass peak. To test the assumption that the background asymmetry is roughly constant in the region around the π^0 mass peak, the asymmetry in each sideband is independently measured to see that they are consistent.

For potential use as a systematic uncertainty on the sideband asymmetries,

p_T (GeV)	Yellow $A_L^{\pi^0}$	$\Delta A_L^{\pi^0}$	$\Delta A_L^{\pi^0}$	$\Delta A_L^{\pi^0}$	chisq/dof
1-1.5	2.63E-4	7.26E-4	1.27E-4	7.37E-4	1.87084/7
1.5-2	7.88-5	4.47E-4	6.83E-5	4.52E-4	7.56794/7
2-2.5	4.64E-4	4.44E-4	4.11E-5	4.46E-4	4.66156/7
2.5-3	-9.31E-4	5.67E-4	2.77E-5	5.68E-4	7.19575/7
3-3.5	1.11E-3	8.03E-4	2.14E-5	8.03E-4	6.64841/7
3.5-4	-6.32E-4	1.17E-3	1.85E-5	1.17E-3	1.55308/7
4-5	2.17E-3	1.39E-3	1.81E-5	1.39E-3	13.0832/7
5-6	3.93E-4	2.59E-3	1.69E-5	2.59E-3	5.69042/7
6-7	-1.42E-3	4.53E-3	1.61E-5	4.53E-3	9.89388/7
7-9	5.44E-3	6.30E-3	1.58E-5	6.30E-3	14.2641/7
9-12	1.04E-2	1.27E-2	0.00E+0	1.27E-2	0.0380221/1
12-15	2.00E-2	3.83E-2	0.00E+0	3.83E-2	0.481514/1

Table 3.3: π^0 A_L Yellow from Run9, with associated errors. Data with $p_T <$ 4 GeV/c are triggered using , while data with $p_T >$ 4 GeV/c are triggered using . The value is calculated for a constant fit to the eight individual results (even/odd⊗spin pattern) where NDF= 7.

we define a quantity

$$\delta A_{syst} \equiv \frac{p_0}{2}\left(1 - P(\chi^2 > \chi^2_{p_0=0})\right). \tag{3.25}$$

Here p_0 is determined from a χ^2 fit across p_T to $A_{LL}^{BG1} - A_{LL}^{BG2}$ with uncertainties $\sqrt{\sigma^2_{BG1} + \sigma^2_{BG2}}$. $P(\chi^2 > \chi^2_{p_0=0})$ represents the probability of having a χ^2 value exceeding the χ^2 that results from fixing $p_0 = 0$. A factor in the uncertainty like $\left(1 - P(\chi^2 > \chi^2_{p_0=0})\right)$ is necessary to quantify our uncertainty as to whether or not there is actually a systematic effect; if $p_0 - 0$ is not statistically significant, $\left(1 - P(\chi^2 > \chi^2_{p_0=0})\right)$ is small and we avoid unnecessarily adding statistical fluctuations to our uncertainty.

BG Asymmetry Comparison Plots

Background asymmetries are plotted vs. invariant mass and p_T in Appendices A.5 and A.6. As an additional check, we compare the "sideband" method of determining A_{LL}^{BG} to a method using linear fitting of A_{LL}^{BG} vs. invariant photon mass. The results of the two methods are compared in Fig. 3.5.5.

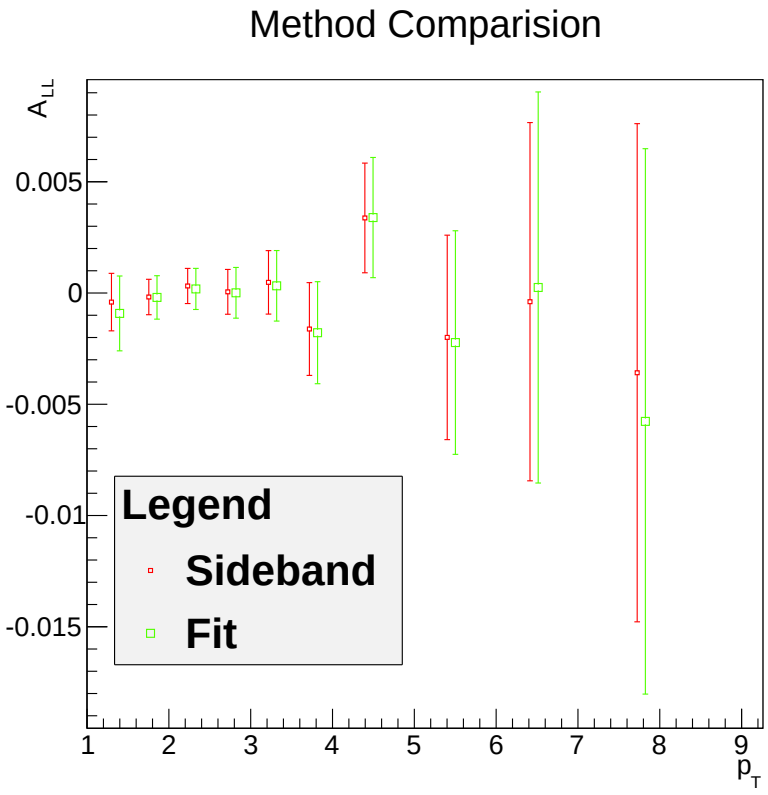

Figure 3.10: A_{LL} calculated with two different methods, the regular sideband method, and a fitting method

p_T (GeV)	Blue $A_L^{\pi^0}$	$\Delta A_L^{\pi^0}$	$\Delta A_L^{\pi^0}$	$\Delta A_L^{\pi^0}$	chisq/dof
1-1.5	2.11E-4	7.25E-4	8.23E-5	7.29E-4	3.331/7
1.5-2	-2.82E-4	4.46E-4	4.37E-5	4.48E-4	4.00816/7
2-2.5	4.32E-5	4.43E-4	2.57E-5	4.43E-4	4.28771/7
2.5-3	7.34E-4	5.65E-4	1.71E-5	5.65E-4	7.32024/7
3-3.5	3.97E-4	8.00E-4	1.33E-5	8.00E-4	5.43012/7
3.5-4	-2.69E-3	1.17E-3	1.14E-5	1.17E-3	6.06213/7
4-5	-2.23E-4	1.38E-3	1.11E-5	1.38E-3	6.70389/7
5-6	-1.37E-3	2.57E-3	1.02E-5	2.57E-3	4.6227/7
6-7	1.57E-3	4.50E-3	9.63E-6	4.50E-3	7.4015/7
7-9	-2.47E-4	6.26E-3	9.51E-6	6.26E-3	5.05028/7
9-12	-4.75E-3	1.26E-2	0.00E+0	1.26E-2	0.00155783/1
12-15	5.53E-2	3.78E-2	0.00E+0	3.78E-2	2.3457/1

Table 3.4: π^0 A_L Blue from Run9, along with associated errors. Data with $p_T < 4$ GeV/c are triggered using , while data with $p_T > 4$ GeV/c are triggered using . The value is calculated for a constant fit to the eight individual results (even/odd⊗spin pattern) where NDF= 7.

Fill Pat.	p_0	Δp_0	$P(\chi^2 > \chi^2_{p_0=0})$	SB Syst. Uncert.
P1	-8.14E-4	2.10E-3	9.38E-1	3.56E-4
P2	-8.69E-5	2.15E-3	5.39E-2	-3.88E-5
P3	5.96E-4	2.34E-3	1.65E-1	2.00E-4
P4	2.66E-3	2.04E-3	6.13E-1	-3.01E-4

Table 3.5: For *even* crossings, systematic uncertainties due to differences in sidebands, along with the parameters used to compute them

Fill Pat.	p_0	Δp_0	$P(\chi^2 > \chi^2_{p_0=0})$	SB Syst. Uncert.
P1	2.64E-3	2.17E-3	4.82E-2	1.19E-3
P2	-9.46E-4	2.21E-3	5.10E-1	9.30E-6
P3	1.68E-3	2.35E-3	2.38E-1	4.40E-4
P4	2.81E-3	2.07E-3	5.13E-1	-3.71E-5

Table 3.6: For *odd* crossings, systematic uncertainties due to differences in sidebands, along with the parameters used to compute them

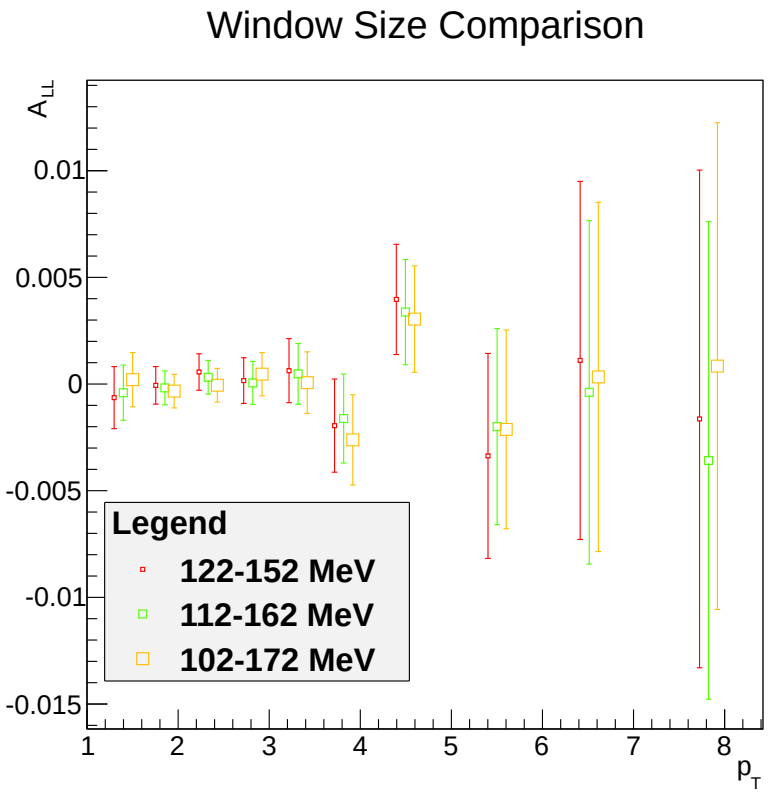

Figure 3.11: A_{LL} calculated with three different signal ranges in the two photon mass spectrum.

3.5.6 Other Crosscheck Asymmetries

A_{LL} from Varying Mass Window

The invariant mass range used to define the "peak" region was varied to see if there was any effect on $A_{LL}^{\pi^0}$. Figure 3.5.6 shows $A_{LL}^{\pi^0}$ p_T for three different "peak" mass ranges. The background "sideband" regions were the same for all three cases. No significant effect is seen when varying the "peak" mass range.

A_{LL} and A_L in EMCal Sub-Detectors

To look for a possible detector-related systematic, we compare the PbSc and PbGl detectors that make up the EMCal. We do so with both double (A_{LL}) and single (A_L) spin asymmetries. If such a systematic effect were from ghost clusters, we would expect to see the largest effect in A_L blue, according to

Figure 2.3 in Subsubsection 2.1.1. No noticeable difference is seen in A_L of the blue beam in Appendix A.4.Since such an effect is not noticeable, so we conclude that our analysis cuts were sufficient to remove the ghost clusters.

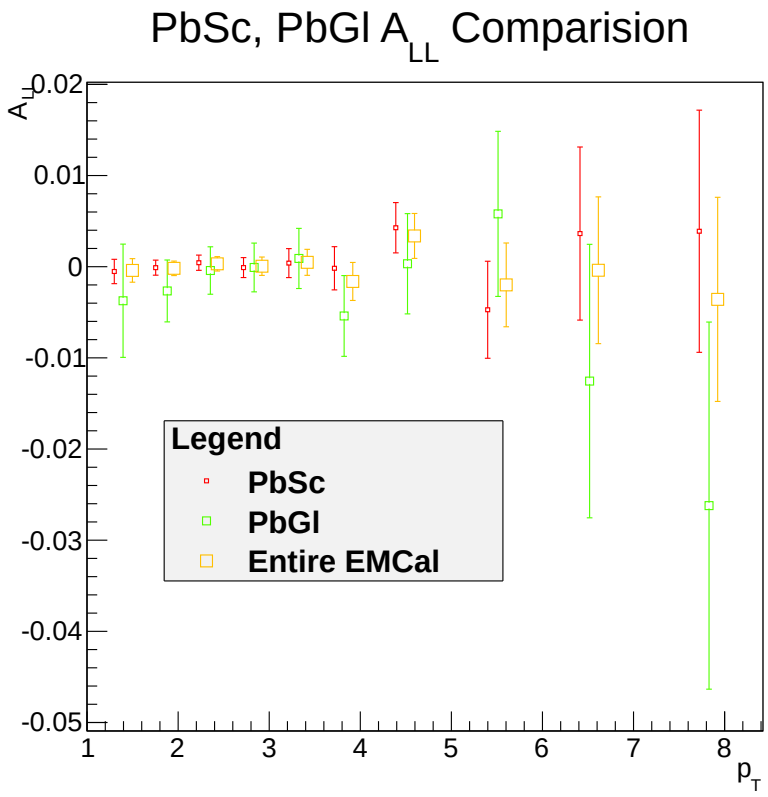

Figure 3.12: A_{LL} calculated in PbSc and PbGl separately, along with in the full detector

3.5.7 Bunch Shuffling

Bunch shuffling is a boot-strapping technique used to extract the statistical uncertainty on A_{LL} in a model-independent way, i.e. no assumptions about underlying statistical distributions need be assumed. The results of bunch shuffling can be checked to see if they agree with the results of our equations for calculating the uncertainty on A_{LL}. The result of such a comparison could point to an unknown systematic uncertainty or an overestimation of the statistical uncertainties.

The typical bunch shuffling procedure employed relies on the smallness of our asymmetries compared to the fractional error on the yield in any given crossing. The spin pattern is completely randomized, separately for each fill, and then fill-by-fill A_{LL} is recalculated based on the new patterns. This procedure is repeated a large number of times, in our case 10,000, and inferences

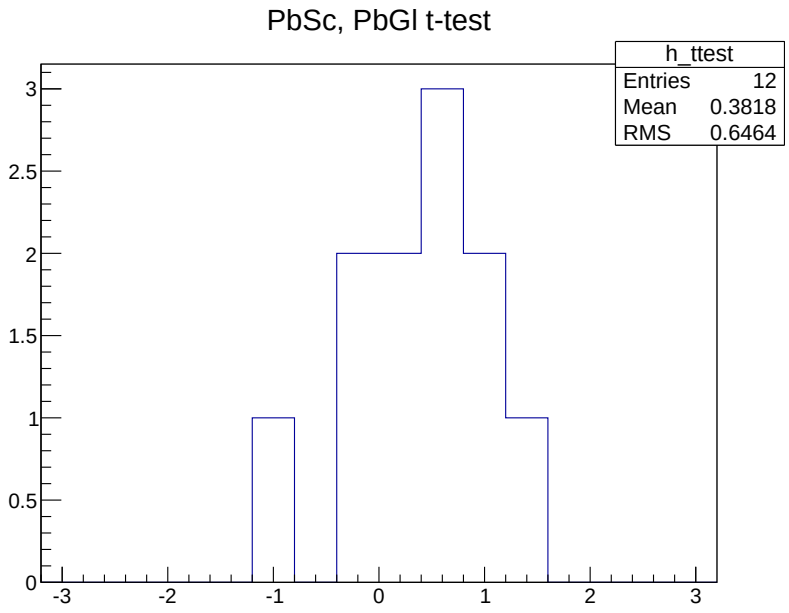

Figure 3.13: Student T-scores between A_{LL} calculated in PbSc and PbGl separately.

can be drawn from the results of the 10,000 shuffles. We do not constrain the relative luminosity in the shuffling, so, for example, if only one crossing were assigned "same" helicity, the relative luminosity would be < 0.01.

We compare statistical uncertainties from bunch shuffling to those calculated from error propagation via Equation 3.6 in each fill by way of the χ^2 distribution, since it has a clear quantitative interpretation. Specifically, we fit A_{LL} versus fill for each sample with each fill's error calculated according to Equation 3.6, which gives one χ^2 value per iteration of the bunch shuffling. We can then check that the χ^2/NDF (number of degrees of freedom) distribution agrees with the theoretical expectation.

The resulting χ^2/NDF distributions for $A_{LL}^{\pi^0+BG}$ and A_{LL}^{BG} are shown in Figs 3.14 and 3.15 for all combinations of *even* and *odd* crossings with the four fill patterns. For $p_T < 4.0$ GeV/c, where some runs are prescaled, the χ^2 distribution is lower than expected. When we switch the error computation from our conservative estimate of $a\sqrt{N}$ to $\sqrt{aN}$ (see Subsubsection 3.2.4), χ^2 shifts up, indicating that our conservative prescale accounting over-estimates the statistical uncertainty. The bunch shuffling result for $p_T < 4.0$ is shown in Figure 3.16.

Also, at high p_T bunch shuffling shows some divergence from the expected distribution for the background regions. This can be understood as an effect due to low (non-Gaussian) statistics.

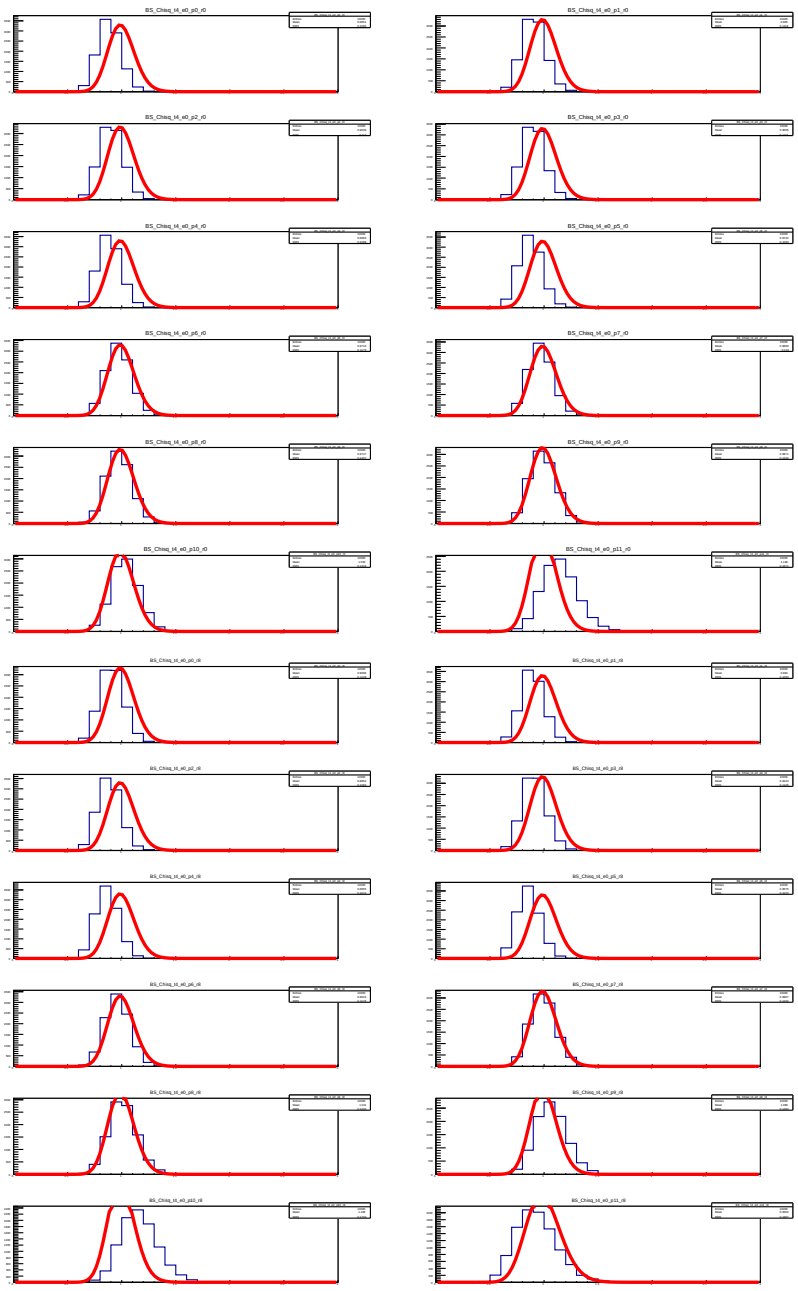

Figure 3.14: Bunch Shuffling χ^2 distributions for peak (left) and sideband (right) regions in *even*, all fill patterns combined (last two bins are even+odd). The red line is the expected distribution.

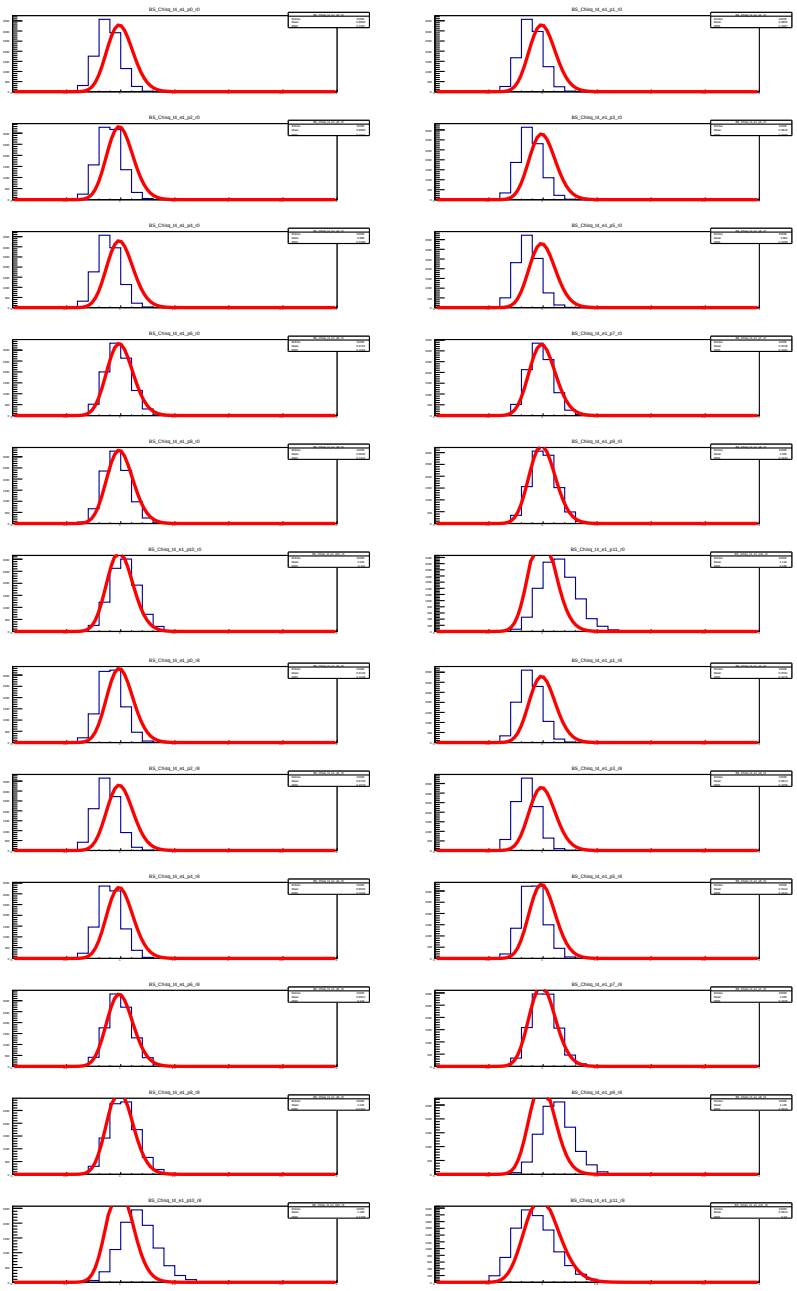

Figure 3.15: Bunch Shuffling χ^2 distributions for peak (left) and sideband (right) regions in *odd*, all spin patterns combined (last two bins are even+odd). The red line is the expected distribution.

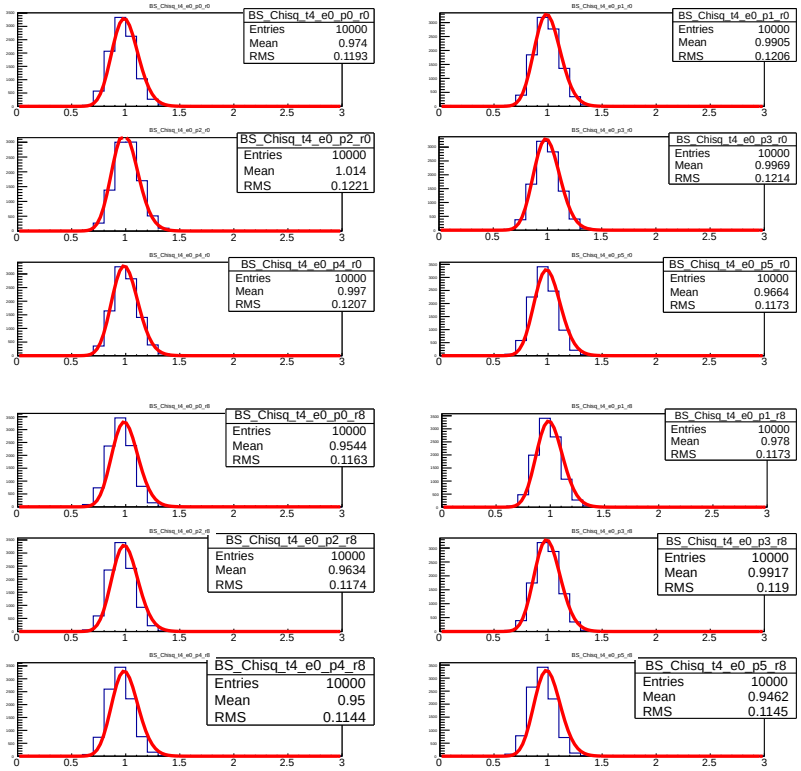

Figure 3.16: Bunch Shuffling χ^2 distributions for triggered events in the lower p_T bins, to demonstrate that the uncertainties were over-estimated in the triggered sample due to the conservative choice described in Section 3.2.4. The red line is the expected distribution.

Chapter 4

Systematic Uncertainty on Relative Luminosity

4.1 Bunch Fitting

With high enough statistics to assume Gaussian probabilities in each crossing, bunch fitting can be used. The bunch fitting formula is $r_i^{\pm} = c(1 \pm \epsilon_{LL})$, where the sign differs from ++ to +− bunches. Chi-squared is given by

$$\sum_{i^+} \frac{(c(1+\epsilon_{LL}) - r_i^+)^2}{\sigma_{r_i^+}} + \sum_{i^-} \frac{(c(1-\epsilon_{LL}) - r_i^-)^2}{\sigma_{r_i^-}}. \tag{4.1}$$

Taking the derivatives with respect to c and ϵ_{LL} and setting them to zero results in

$$\begin{aligned}
\frac{\partial \chi^2}{\partial \epsilon_{LL}} &= 0 = \sum_{i^+} \frac{(c(1+\epsilon_{LL}) - r_i^+)}{\sigma_{r_i^+}} - \sum_{i^-} \frac{(c(1-\epsilon_{LL}) - r_i^-)}{\sigma_{r_i^-}}, \\
\frac{\partial \chi^2}{\partial c} &= 0 = \sum_{i^+} \frac{(1+\epsilon_{LL})(c(1+\epsilon_{LL}) - r_i^+)}{\sigma_{r_i^+}} + \sum_{i^-} \frac{(1-\epsilon_{LL})(c(1-\epsilon_{LL}) - r_i^-)}{\sigma_{r_i^-}}
\end{aligned}$$

These equations can be conveniently rewritten using the following defini-

tions:

$$\begin{aligned} S^+ &= \sum_{i^+} \frac{1}{\sigma^2_{r_i^+}}, \\ S^- &= \sum_{i^-} \frac{1}{\sigma^2_{r_i^-}}, \\ S_r^+ &= \sum_{i^+} \frac{r_i^+}{\sigma^2_{r_i^+}}, \\ S_r^+ &= \sum_{i^-} \frac{r_i^-}{\sigma^2_{r_i^-}}. \end{aligned}$$

With these definitions we have

$$\begin{aligned} 0 &= c(1+\epsilon_{LL})^2 S^+ + c(1-\epsilon_{LL})^2 S^- - (1+\epsilon_{LL})S_r^+ - (1-\epsilon_{LL})S_r^-, \\ 0 &= c(1+\epsilon_{LL})S^+ - c(1-\epsilon_{LL})S^- - S_r^+ + S_r^-. \end{aligned}$$

We now solve both of these equations for c. We get

$$\begin{aligned} c &= \frac{(1+\epsilon_{LL})S_r^+ + (1-\epsilon_{LL})S_r^-}{(1+\epsilon_{LL})^2 S^+ + (1-\epsilon_{LL})^2 S^-}, \\ c &= \frac{S_r^+ - S_r^-}{(1+\epsilon_{LL})S^+ - (1-\epsilon_{LL})S^-}. \end{aligned}$$

Setting the two equations equal, we can solve for ϵ_{LL}:

$$\epsilon_{LL} = \frac{S_r^+ S^- - S_r^- S^+}{S_r^+ S^- + S_r^- S^+} \tag{4.2}$$

which when substituted into the above equation for c yields:

$$c = \frac{S_r^+ S^- + S_r^- S^+}{2S^+ S^-} \tag{4.3}$$

We now calculate the uncertainty in each of these parameters. To do this, note that derivatives with respect to r_i^+ only affect S_r^+, and r_i^- S_r^-. Also, by the chain rule,

$$\frac{\partial S_r^+}{\partial r_i^+} = \frac{1}{\sigma^2_{r_i^+}}, \tag{4.4}$$

and similarly for $-$. Using this, we find

$$\sigma_c^2 = \frac{1}{4}\left(\frac{1}{S^+} + \frac{1}{S^-}\right) \tag{4.5}$$

$$\sigma_{\epsilon_{LL}}^2 = \frac{4(S^+S^-)^2}{(S_r^+S^- + S_r^-S^+)^4}\left((S_r^+)^2S^- + (S_r^-)^2S^+\right). \tag{4.6}$$

4.2 Coincidence Counting Method

The standard method for calculating relative luminosity before the 2009 run was to use bunch fitting on the ratio

$$r_i = \frac{N_{ZDC}^i}{N_{BBC}^i}, \tag{4.7}$$

where N_{ZDC} and N_{BBC} are simply the number of times the two arms of each detector fired in coincidence in a given crossing i. Bunch fitting this quantity is equivalent to measuring the raw asymmetry of BBC triggers with respect to ZDC triggers, and polarization scaling is then applied fill-by-fill to find A_{LL}^R. We choose the ZDC for comparison because, in addition to having a different geometrical acceptance, it samples a significantly different class of events than the BBC. The BBC fires predominantly on charged particles and is dominated by low-p_T soft physics, whereas the ZDC samples mainly diffractive physics and, due to its location behind the accelerator's bending magnets, which sweep away most charged particles, fires on neutrons, photons, and hadronic showers from scattered protons interacting with the machine elements. The asymmetries in the different physics sampled by the ZDC and the BBC cannot be directly calculated. However, comparing these two detectors with different physics sensitivities increases the likelihood that any non-zero asymmetries would be apparent.

This standard "coincidence" method was applied to the 2009 data at $\sqrt{s} =$ 200 GeV [45]. The resulting value for that year along with 2005 and 2006 is shown in Table 4.1. The systematic uncertainty comes from a crossing-by-crossing correction that was made to account for the ZDC online z-vertex smearing of approximately 30 cm. To be conservative, the A_{LL}^R value found plus its total uncertainty is used as the systematic uncertainty on any physics A_{LL} measurement. The reason for the increased value of A_{LL} in 2009 with respect to the previous years has been investigated and will be described in the coming sections, but no satisfactory explanation has been found.

Run Year	A_{LL}^R (10^{-3})	ΔA_{LL}^R(stat+syst) (10^{-3})
2005	0.42	0.23
2006	0.49	0.25
2009	1.18	0.21

Table 4.1: Measured value of A_{LL}^R in $\sqrt{s} = 200$ GeV $\vec{p}+\vec{p}$ running in the given years. A_{LL}^R plus its uncertainty is used as the total shift uncertainty for any physics asymmetry result using the BBC as a relative luminosity monitor. The run-year-correlated part of the uncertainty is taken to equal the maximal overlap in A_{LL}^R across years: 0.42×10^{-3}. The remaining part of each year's A_{LL}^R plus its statistical uncertainty is taken as a run-year uncorrelated part.

4.3 Rate Safe Method

As instantaneous luminosity has increased at RHIC, multiple collisions in one beam crossing have become more likely, and the use of a detector coincidence (such as the "AND" of the BBC arms) as a luminosity monitor has become less valid. This is because a simple detector coincidence is a "binary" result that conveys no direct information about how many times the detector was hit by particles from the collision. However, by modeling the probability of triggering the detector over many crossings of the beam, we can indirectly extract this information. In effect, we change our assumption from 0 = no collision, 1 = 1 collision to 0 = no collision, 1 = ($\geq$ 1 collision) and extract the true hit rate in the detectors from the probabilities for these events.

Detection Probabilities in a Two-Arm Detector

In deriving the probabilities for a two-arm detector such as the BBC to detect a given event, it is useful to first make the following definitions:

- λ: average number of events that are physically capable of triggering both arms of the detector.
- $\lambda_{N(S)}$: average number of events that are NOT physically capable of triggering both arms of the detector, only the North(South) arm.
- $\epsilon_{N(S)}$: efficiency×acceptance for the North (South) arm for detecting λ.
- $\epsilon_{N(S)}^{N(S)}$: efficiency×acceptance for detecting λ_N in the North arm (λ_S in the South arm).

Now we consider the probability distribution for the true number of collisions of type λ in one crossing. If there are of order $\sim 10^{11}$ protons in each bunch, the number of possible collisions in one crossing is of order $\sim 10^{22}$. Since we know from experience that the number of collisions actually occurring in each crossing is much less than $\sim 10^{22}$ (typically of order 1), we can safely assume the number of collisions follows a Poisson distribution with an average number λ,

$$P_{DS}(i) = \frac{\lambda^i e^{-\lambda}}{i!}, \tag{4.8}$$

where i is the number of collisions. Given this probability distribution, we can calculate the probability that k_S of these collisions are seen by the South arm of our detector (regardless of whether or not the multiple collisions are distinguishable in the detector readout).

$$P_{DS}(k_S) = \sum_{i=k_S}^{\infty} \binom{i}{k_S} \epsilon_S^{k_S} \left(1-\epsilon_S\right)^{i-k_S} P_{DS}(i). \tag{4.9}$$

There are appropriate factors for detecting k_S collisions and not detecting $i-k_S$ others, along with a factor $\binom{i}{k_S}$ for the number of ways this can happen. The sum starts at k_S since if there are k_S distinct hits detected (neglecting, for the moment, random noise), we can be sure there were at least k_S collisions.

By pulling k_S factors of λ out of the sum and re-indexing, one can show that the probability for k_S collisions is also a Poisson distribution:

$$\begin{aligned}
P_{DS}(k_S) &= \sum_{i=k_S}^{\infty} \frac{i!}{k_S!(i-k_S)!} \epsilon_S^{k_S} \left(1-\epsilon_S\right)^{i-k_S} \frac{\lambda^i e^{-\lambda}}{i!} \\
&= \frac{1}{k_S!} \epsilon_S^{k_S} \lambda^{k_S} e^{-\lambda} \sum_{i=k_S}^{\infty} \frac{1}{(i-k_S)!} \left(1-\epsilon_S\right)^{i-k_S} \lambda^{i-k_S} \\
&= \frac{1}{k_S!} \epsilon_S^{k_S} \lambda^{k_S} e^{-\lambda} e^{(1-\epsilon_S)\lambda} \\
&= \frac{\left(\epsilon_S \lambda\right)^{k_S} e^{-\epsilon_S \lambda}}{k_S!}.
\end{aligned} \tag{4.10}$$

From Equation 4.10 we can proceed to derive the joint probability distribution $P_{DS}(k_S, k_N)$ for seeing k_S collisions in the South arm and k_N in the

north arm. First, note that

$$\begin{aligned} P_{DS}(k_S, k_N) &= P_{DS}(k_N|k_S) P_{DS}(k_S) \\ &= \left(\sum_{i=k_N}^{\infty} \binom{i}{k_N} \epsilon_N^{k_N} \left(1-\epsilon_N\right)^{i-k_N} P_{DS}(i|k_S) \right) P_{DS}(k_S) \end{aligned} \tag{4.11}$$

$P_{DS}(i|k_S)$ is the probability that there were i collisions given that we measured k_S hits. Using Bayes' theorem, we can express

$$P_{DS}(i|k_S) = \frac{P_{DS}(k_S|i) P_{DS}(i)}{P_{DS}(k_S)}. \tag{4.12}$$

$P_{DS}(k_S|i)$ is just

$$P_{DS}(k_S|i) = \binom{i}{k_S} \epsilon_S^{k_S} \left(1-\epsilon_S\right)^{i-k_S} \Theta(i-k_S), \tag{4.13}$$

where the step function ensures the detector arm does not see more distinct hits then there are collisions.

Substituting Equations 4.12 and 4.13 into 4.11, we arrive at

$$P_{DS}(k_S, k_N) = \sum_{i=\max(k_S,k_N)}^{\infty} \binom{i}{k_S} \binom{i}{k_N} \epsilon_S^{k_S} \epsilon_N^{k_N} \left(1-\epsilon_S\right)^{i-k_S} \left(1-\epsilon_N\right)^{i-k_N} P_{DS}(i). \tag{4.14}$$

Note that the step function, along with the original lower limit on the sum of k_S, can be accounted for by setting the lower limit to $\max(k_S, k_N)$. For the special case $P_{DS}(k_S = 0, k_N = 0)$ this formula reduces to

$$P_{DS}(k_S = 0, k_N = 0) = e^{\epsilon_S \epsilon_N \lambda - \epsilon_S \lambda - \epsilon_N \lambda} = e^{-\epsilon_N(1-\epsilon_S)\lambda} e^{-\epsilon_S \lambda}. \tag{4.15}$$

Allowing Single-Sided Events

We now consider single-sided events, which by our definition are only capable of triggering one detector. The distributions describing the number of such collisions in a crossing are again Poisson, this time with average numbers λ_S and λ_N. The probability of seeing k_S distinct time hits in the south detector, for instance, is the same as before:

$$P_{SS}(k_S) = \frac{\left(\epsilon_S^S \lambda_S\right)^{k_S} e^{-\epsilon_S^S \lambda_S}}{k_S!}. \tag{4.16}$$

Most importantly, the probability for seeing zero hits is $e^{-\epsilon_S^S \lambda_S}$. The probability of detecting a total of zero hits in the south detector, both from single and double-sided events, is then

$$\begin{aligned} P(k_S = 0) &= P_{DS}(k_S = 0) P_{SS}(k_S = 0) \\ &= e^{-\epsilon_S \lambda + \epsilon_S^S \lambda_S}. \end{aligned} \tag{4.17}$$

Note that the samples these two distributions apply to do not overlap and so the (non-)events are independent. Similarly, the probability of detecting zero collisions in the two-sided detector is given by

$$P(k_S = 0, k_N = 0) = P_{DS}(k_S = 0, k_N = 0) P_{SS}(k_S = 0) P_{SS}(k_N = 0) = e^{\epsilon_S \epsilon_N \lambda - \epsilon_S \lambda - \epsilon_N \lambda - \epsilon_S^S \lambda_S - \epsilon_N^N \lambda_N}. \tag{4.18}$$

Removing Single-Sided Events

The utility of these three separate probability distributions becomes apparent when we consider the function

$$ln(P(k_S = 0, k_N = 0)) - ln(P(k_S = 0)) - ln(P(k_N = 0)) = \epsilon_N \epsilon_S \lambda, \tag{4.19}$$

or, since $P(k_S = 0) = 1 - P_S$, $P(k_N = 0) = 1 - P_N$, and $P(k_S = 0, k_N = 0) = 1 - P_{OR}$, where P_S, P_N, and P_{OR} are the probabilities of south, north, and OR triggers,

$$ln(1 - P_{OR}) - ln(1 - P_S) - ln(1 - P_N) = \epsilon_N \epsilon_S \lambda. \tag{4.20}$$

Only events and backgrounds capable of causing true coincidence in the two detectors contribute to this quantity. Furthermore, it completely takes into account the effects of multiple collisions. If ϵ_S and ϵ_N are not spin dependent (which is an assumption of the present method for calculating relative luminosity) this quantity can be used to calculate the relative luminosity, although it will not include a vertex cut requirement.

Measurement and Statistical Uncertainty

As is always the case in experiments, it is not possible to know our true parameters exactly; we must estimate P_N, P_S, and P_{OR} from the data. The way to do this is to look at a set number of unbiased events (i.e. all events) and count the number of triggers within that sample. Since the probability of a trigger in any given crossing is significant, we cannot approximate the uncertainty on the number of triggers with a Poisson distribution and must use the full binomial distribution. The probability distribution for the number

of OR triggers in N_{clock} events, for example, is

$$P(N_{OR} = n) = \binom{N_{clock}}{n} P_{OR}^{n} \left(1 - P_{OR}\right)^{N_{clock}-n}. \tag{4.21}$$

The standard deviation in this case is $\sqrt{N_{clock} P_{OR}(1 - P_{OR})}$, and the mean is $N_{clock} P_{OR}$. We can see that estimating the sample mean by the actual number of OR triggers, N_{OR}, is equivalent to estimating P_{OR} as N_{OR}/N_{clock}. The estimate for the standard deviation of N_{OR} is then $\sqrt{N_{OR}(1 - \frac{N_{OR}}{N_{clock}})}$.

In propagating our errors through Equation 4.20, it is easiest to reformulate the equation in terms of non-overlapping counts $N_{N!S}$, $N_{S!N}$, and N_{AND} in order to elimate the necessity for correlation terms:

$$\epsilon_N \epsilon_S \lambda = ln(1 - P_{N!S} - P_{S!N} - P_{AND}) - ln(1 - P_{S!N} - P_{AND}) - ln(1 - P_{N!S} - P_{AND}). \tag{4.22}$$

Then one can proceed with the usual linear propagation of errors.

Correction Results

Figure 4.1 shows the relative difference between the two-arm coincidence rate and $\epsilon_N \epsilon_S \lambda$ for the full z-vertex in the 2009 $\sqrt{s} = 200$ GeV and the 2011 $\sqrt{s} = 500$ GeV runs. The latter had much higher rates, and so the correction is much stronger. For the BBC, the dominant effect is multiple collisions, and thus $\epsilon_N \epsilon_S \lambda$ is higher than the coincidence rate. For the ZDC, accidental coincidences from λ_N and λ_S dominate, so $\epsilon_N \epsilon_S \lambda$ is lower than the coincidence rate. The figures can be thought of as showing the fractional "over-counting" or "under-counting" of the simple coincidence trigger.

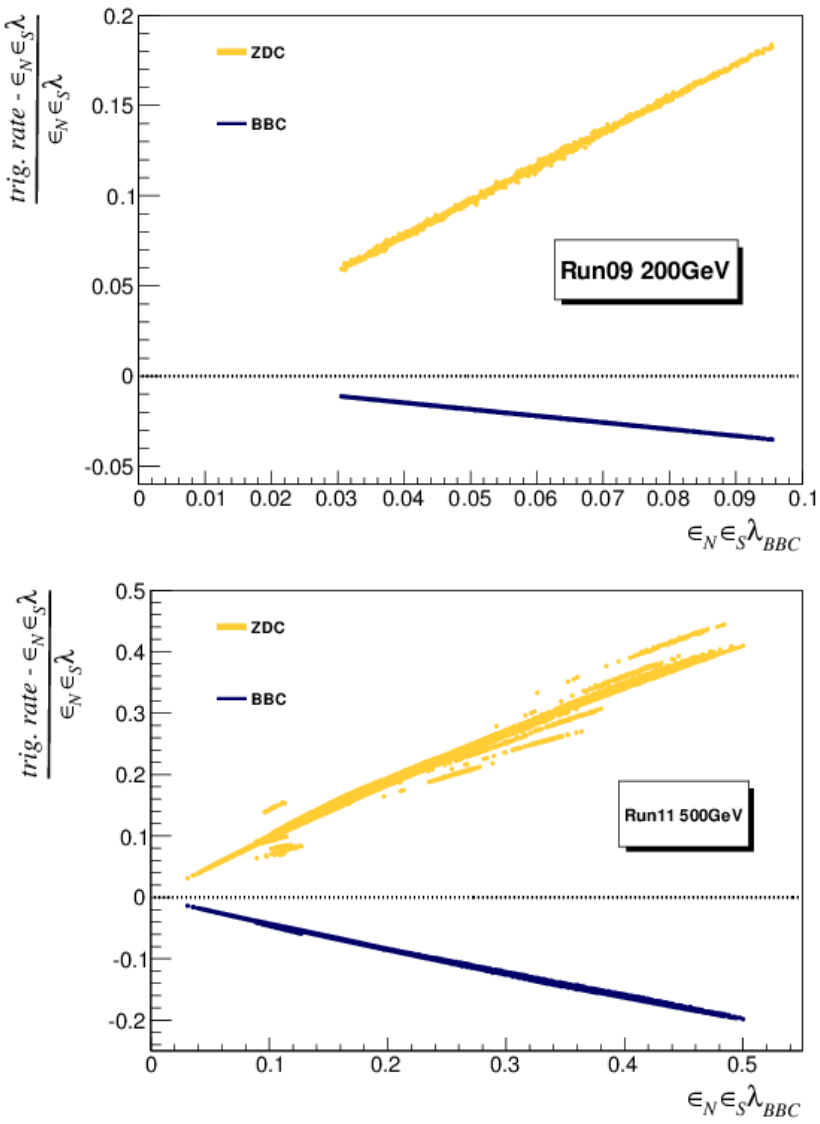

Figure 4.1: Relative difference between the measured trigger rate and the quantity $\epsilon_N\epsilon_S\lambda$ plotted for all beam crossings in the 2009 and 2011 runs.

The average $\chi^2/d.o.f.$ when bunch-fitting all fills with the $\epsilon_N\epsilon_S\lambda$ method is about 1.3, versus 5.9 for the coincidence method. After bunch-fitting all of the fills to produce ϵ_{LL} using either the coincidence or $\epsilon_N\epsilon_S\lambda$ method, the results can be fit across fills to constant functions to extract four asymmetries, one for each spin pattern. Figure 4.2 plots these raw asymmetries for both methods, visually displaying them as normal distributions with mean and sigma from the fit results. Spin patterns P1 and P4 are equivalent for a double-spin asymmetry, as are P2 and P3, which dictates the grouping of the values. Using the $\epsilon_N\epsilon_S\lambda$ method instead of the coincidence method reduces the spread in the spin patterns from around 1×10^{-3} to 2.5×10^{-4}. The leftover spread could potentially be attributed to bunch width variations (see Section 4.5), although it is not yet clear. When scaled by the polarization, as

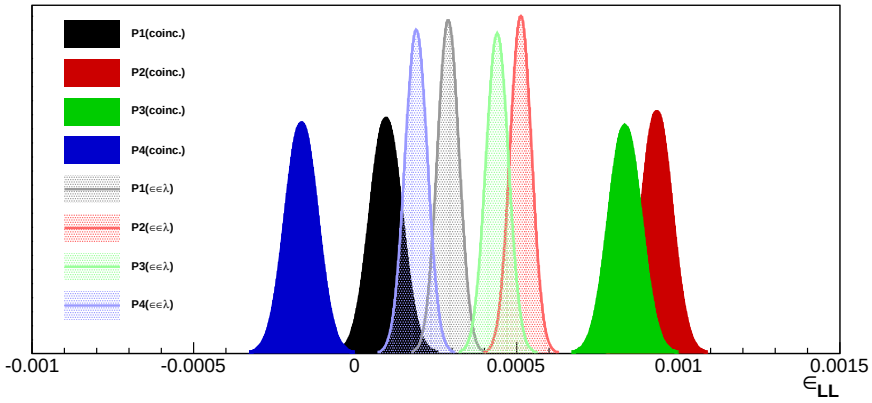

Figure 4.2: Results for the raw ZDC to BBC asymmetry in the 2009 $\sqrt{s} =$ 200 GeV run, both with the coincidence method, and with the $\epsilon_N\epsilon_S\lambda$ method.

in Fig. 4.3, the uncertainty-weighted-average across the four spin patterns of the full-vertex $\epsilon_N\epsilon_S\lambda$ calculated relative luminosities is

$$A_{LL}^R = 1.11 \pm 0.05 \times 10^{-3}, \tag{4.23}$$

which is in agreement with the 30 cm vertex coincidence value in Table 4.1. This strongly indicates that the increased value of the relative luminosity systematic in the 2009 run is not due to rate or bunch width effects.

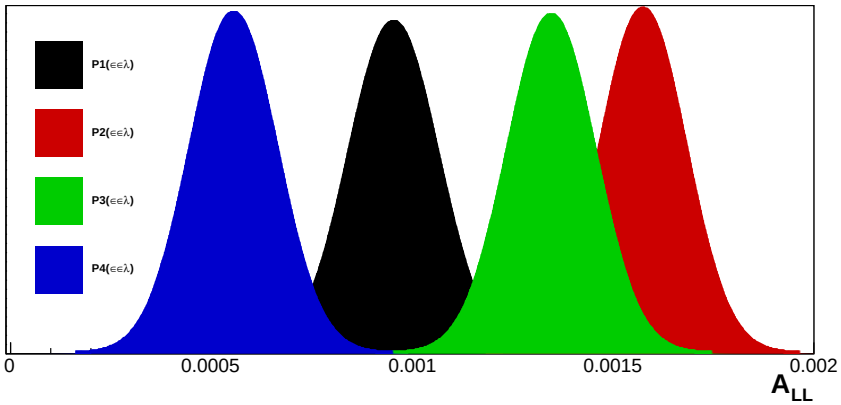

Figure 4.3: Results for the polarization scaled ZDC to BBC asymmetry A_{LL}^{R} in the 2009 $\sqrt{s} = 200$ GeV run with the $\epsilon_N \epsilon_S \lambda$ method.

Rate Safe Relative Luminosity from the 2011 $\sqrt{s} = 500$ GeV and 2012 $\sqrt{s} = 510$ GeV Runs

When bunch fitting is applied to the $\sqrt{s} = 500$ GeV runs, it fails for the coincidence method due to the strength of the rate effects. Figure 4.4 shows the resultant $\chi^2/d.o.f.$ distribution from trying to bunch-fit with the coincidence method, along with the result for the $\epsilon_N\epsilon_S\lambda$ method, which is still poor. Figures 4.5 and 4.6 show the result of the $\epsilon_N\epsilon_S\lambda$ method for these two runs.

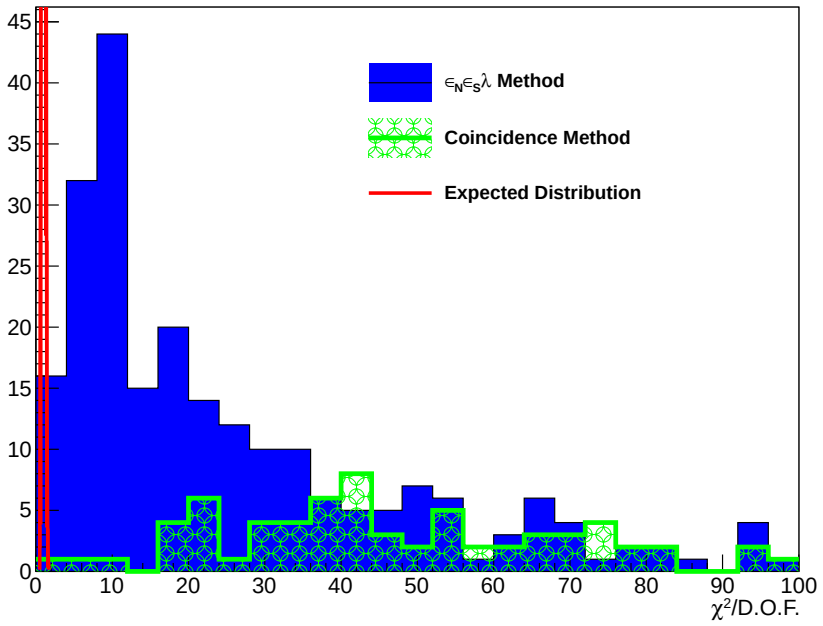

Figure 4.4: χ^2 per degree of freedom in the 2011 $\sqrt{s} = 500$ GeV run, both with the coincidence method and with the $\epsilon_N\epsilon_S\lambda$ method. Also shown is the expected χ^2 distribution for the given degrees of freedom.

Four additional spin patterns were added in the 2012 run. In both cases the raw asymmetry values average much closer to zero, with similar spread to the 2009 values at $\sqrt{s} = 200$ GeV. One potential explanation may be that the remaining transverse component of the polarization was kept as small as possible in these runs, generally always $< 5\%$ (although final numbers are not yet available for the 2011 and 2012 runs) of the total polarization in both beams, compared to 11% and 23% of the total polarization in 2009. Of course it could also be that it is a true physics asymmetry that is simply smaller at higher $\sqrt{s}$. Future longitudinal running at $\sqrt{s} = 200$ GeV with a smaller transverse polarization component would help clarify this point.

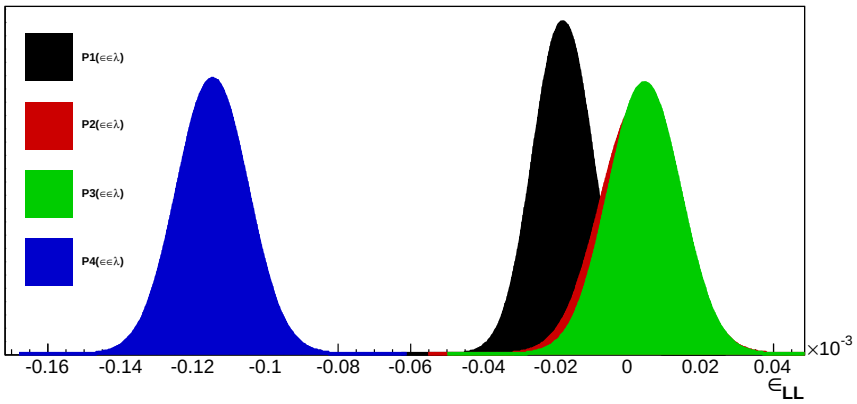

Figure 4.5: Results for the raw ZDC to BBC asymmetry in the 2011 $\sqrt{s} =$ 500 GeV run with the $\epsilon_N \epsilon_S \lambda$ method. Bunch-fitting fails for the coincidence method because the rate effects are too severe.

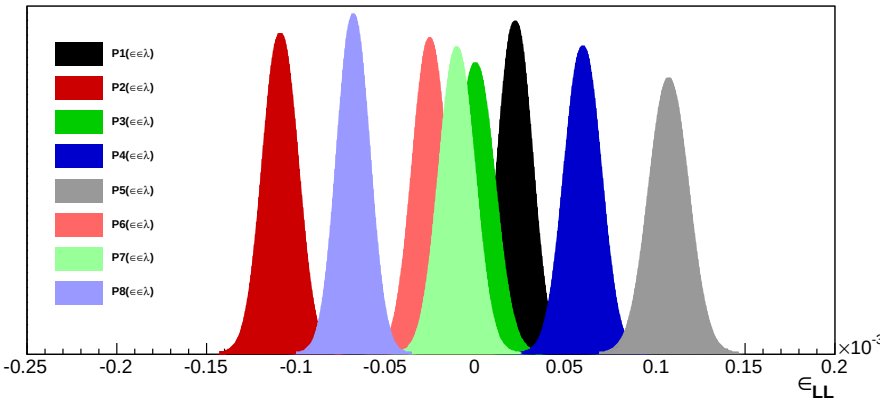

Figure 4.6: Results for the raw ZDC to BBC asymmetry in the 2012 $\sqrt{s} =$ 510 GeV run with the $\epsilon_N \epsilon_S \lambda$ method. Bunch-fitting fails for the coincidence method because the rate effects are too severe.

4.4 Beam Geometry + Transverse Polarization Effects

4.4.1 Simple Model: Colinear Beam Angles and $\epsilon_{++}$to$_{--}$

In this subsection we propose a simple model that can generate a variety of false asymmetries given transversely polarized beam components and an offset or angle of the beams relative to a nominal detector axis. Consider Fig. 4.7, which shows various geometries for beams through a zero-field region. Any complex beam geometry can be expressed as a linear combination of these configurations, which we call "colinear angles," "offsets," and "boosts." The

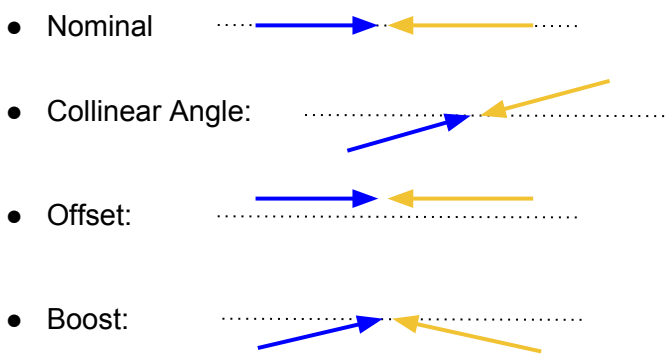

Figure 4.7: Any straight-line beam geometries through the interaction region can be decomposed into the components illustrated here .

existence of a transverse spin asymmetry to which our detector is sensitive means that the production of particles to the right of any forward going beam will be suppressed, with a corresponding excess in production to the left. If the beam is angled, offset, or boosted perpendicular to the transverse polarization axis, the left and right sides will see a modified detector acceptance, as is shown in Fig. 4.8 for a colinear beam angle. We can express this resulting left-right acceptance inbalance as an "acceptance modification factor" in terms of some small parameter δ assuming the beam geometry is small. It is immediately clear that a variety of asymmetries will be generated, including an asymmetry that would seemingly violate parity invariance of the strong interaction (ϵ_{++} to $_{--}$), one that would violate 180° rotational invarance of the experiment (ϵ_{+-} to $_{-+}$), and two double-spin asymmetries with the helicity of one beam held constant (ϵ_{++} to $_{+-}$ and ϵ_{--} to $_{-+}$). All of the helicity combinations used to calculate these asymmetries are highlighted in Fig. 4.8.

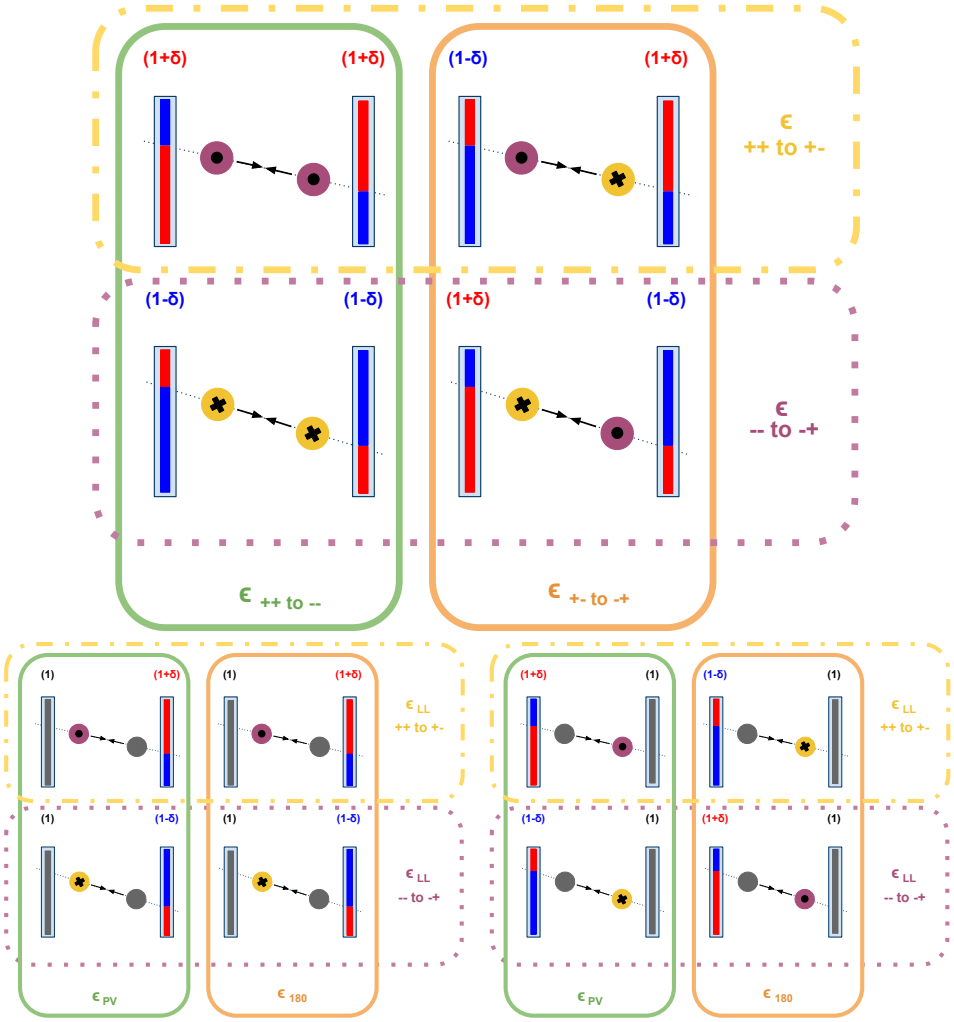

Figure 4.8: Single and double-spin contributions to false asymmetries with a colinear beam angle. The blue and red shadings in an example "detector" indicate the level of left-right particle production with respect to the beam polarizations, which are in or out of the page. Blue shading indicates a suppression in production, and red the corresponding excess. The overall effect of the colinear angle and A_N on particle production into the detector acceptance is summarized above each detector arm as an"acceptance modification factor" in terms of the small parameter δ.

Let us consider only this case of colinear beam angles with transverse beam polarization. The total beam polarization need not be 100%, in fact, lets generalize it to be P_1 in the rightward moving beam and P_2 in the leftward moving beam (according to the diagrams in Figure 4.8). Then, summing up the polarization-weighted contributions from all possible diagramsin terms of the acceptance modification factors, we calculate for $\epsilon_{++\text{to}--}$

$$\begin{aligned}
\epsilon_{++\text{to}--} &\approx P_1(1-P_2)\frac{(1+\delta)-(1-\delta)}{(1+\delta)+(1-\delta)} \\
&+ (1-P_1)P_2\frac{(1+\delta)-(1-\delta)}{(1+\delta)+(1-\delta)} \\
&+ P_1P_2\frac{(1+\delta)^2-(1-\delta)^2}{(1+\delta)^2+(1-\delta)^2} \\
&+ (1-P_1)(1-P_2)*0 \\
&\approx P_1(1-P_2)\delta + (1-P_1)P_2\delta + P_1P_2 2\delta \\
&= (P_1+P_2)\delta, \qquad (4.24)
\end{aligned}$$

where δ could actually be replaced by $\delta(\theta)$, since it depends on the colinear beam angle θ.

Thus, our prediction for the size of our false $\epsilon_{++\text{to}--}$ is

$$(P_1+P_2)\delta(\theta). \qquad (4.25)$$

Predictions for all of the asymmetries, whose derivations are analgous, are tabulated in Table 4.2. We see that colinear angles produce the seemingly

Geometry	$\epsilon_{++\text{to}--}$	$\epsilon_{+-\text{to}-+}$	$\epsilon_{++\text{to}+-}$	$\epsilon_{--\text{to}-+}$
Colinear Angle	$(P_B+P_Y)\delta$	0	$P_Y\delta$	$-P_Y\delta$
Offset	0	$(P_B+P_Y)\delta$	$-P_Y\delta$	$P_Y\delta$
Boost	0	$(P_B+P_Y)\delta$	$-P_Y\delta$	$P_Y\delta$

Table 4.2: Model predictions for the various asymmetries.

parity violating and double spin asymmetries, while offsets and boosts both produce seemingly 180° rotation voilating asymmetries, along with double spin asymmetries with the opposite sign of those produced with colinear angles. In the next section, we use our simulation to confirm this linear dependence on polarization and to estimate the function $\delta(\theta)$.

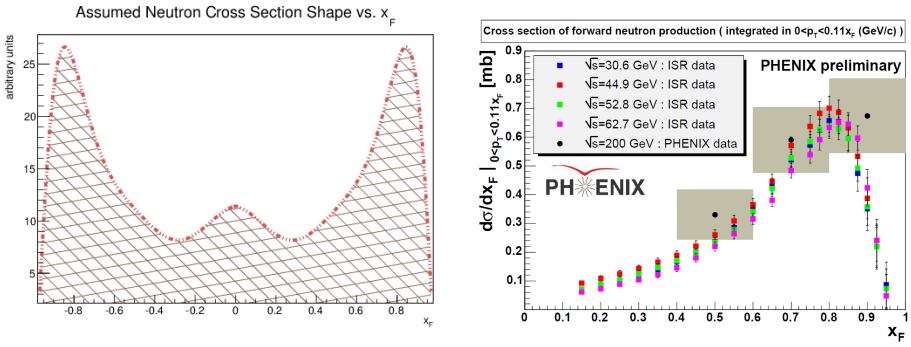

Figure 4.9: (a) Simulation assumed neutron cross-section shape vs. x_F, and (b) Actual measurements of the neutron cross-section vs x_F, a preliminary version of [6].

4.4.2 Simulation

To test the hypothesis, a simulation was designed to collide beams at various angles and offsets, and then produce neutrons (for the ZDC) and charged tracks (for the BBC) at random collision points according to distributions measured in various experiments. The trajectories of these neutrons and charged tracks were then checked for intersection with the ZDC and BBC geometries. The simulation did not require energy or quantum number conservation in the collision.

First, it should be emphasized that this simulation was done specifically for $\sqrt{s} = 200$ GeV. With that clear, following are the neutron cross-section shape distributions used, along with the motivating measurements. A neutron cross-section shape was assumed in simulation as a function of x_F, as well as that measured at various $\sqrt{s}$ by ISR [34] (including also three points at 200 GeV by PHENIX), shown in Figure 4.9. Also assumed was a correlated cross-section shape vs. p_T and ϕ, shown in Figure 4.10. The function plotted is

$$p_T e^{-4.8 p_T} \left(1 - 0.43 p_T cos(\phi)\right). \tag{4.26}$$

This cross-section shape also depends on the spins of the beams through step functions that can reverse the sign of the cosine term (not shown here). The motivation for the above is a $p_T e^{-4.8 p_T}$ cross-section dependence measured by ISR and the PHENIX A_N measurement and its p_T dependence, shown also in Figure 4.10. Distributions for charged tracks for the BBC are also included in the simulation, but they are irrelevant for two reasons: we traditionally have not seen an A_N in the PHENIX BBC, and angles and boosts have less

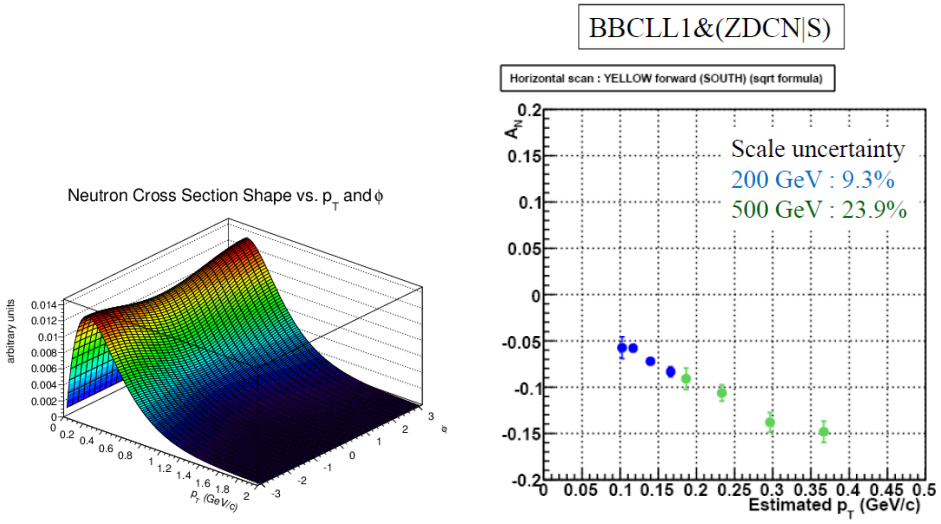

Figure 4.10: (a) Simulation assumed neutron cross-section shape vs. p_T and ϕ, and (b) the motivating PHENIX measurement, a preliminary version of [6].

effect on the BBC due to it's relative closeness (compared to the ZDC) to the interaction point. So, in our simulation, the BBC acts as a relative luminosity monitor with $R = 1$. Thus, we do not bother showing the charged track distributions here. For the bunches collided we assume simple but realistic Gaussian shapes, the x, y, and z profiles of which are shown in Figures 4.11 and 4.12.

Figure 4.13 of our simulation results shows $\epsilon_{++\text{to}--}$ as a function of colinear beam angle θ for the case of 100% polarization. We see immediately that $\delta(\theta)$ is very well described by a linear function. If we fit the case with 100%

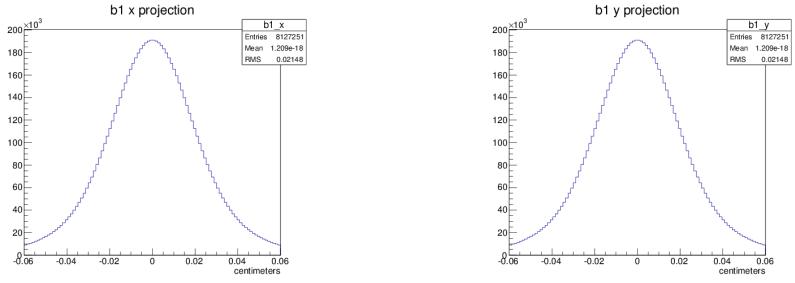

Figure 4.11: Bunch shapes in x and y assumed in the simulation.

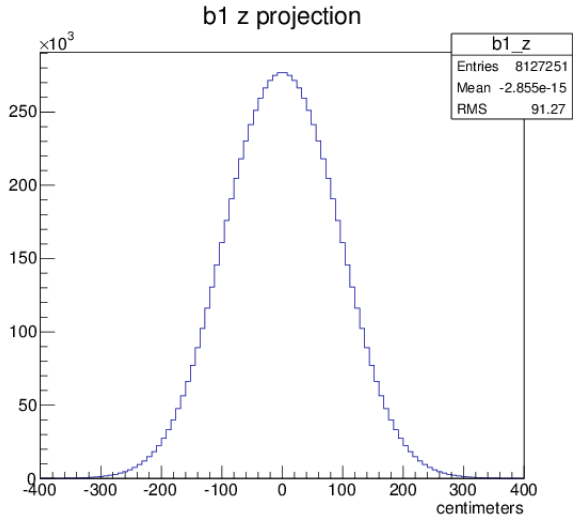

Figure 4.12: Bunch shape in z assumed in the simulation.

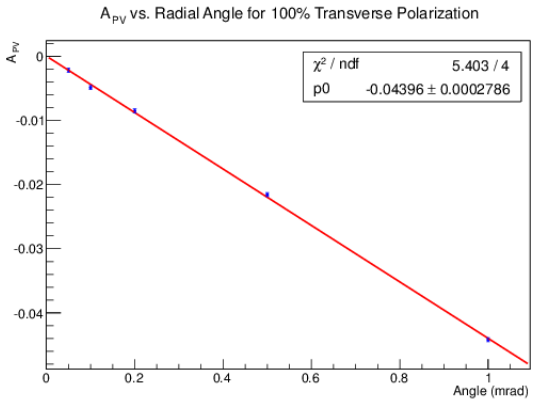

Figure 4.13: $\epsilon_{++\text{to}--}$ vs. colinear beam angle from simulation for 100% transverse beam polarization. Red line is a fit.

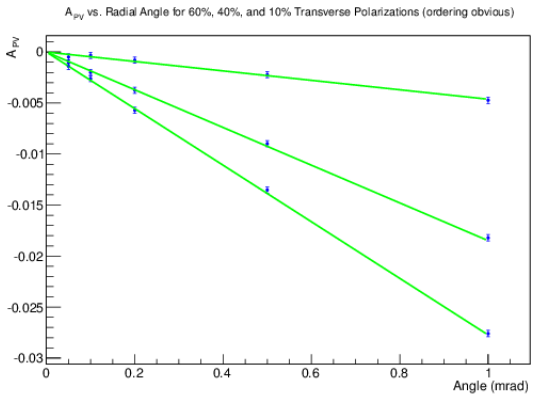

Figure 4.14: ϵ_{PV} vs. colinear beam angle for transverse polarizations of 60, 40, and 10%. The green lines are all taken from the above fit in Figure 4.13 for 100% polarization and scaled by P, thus showing linear dependence on polarization in our simulation.

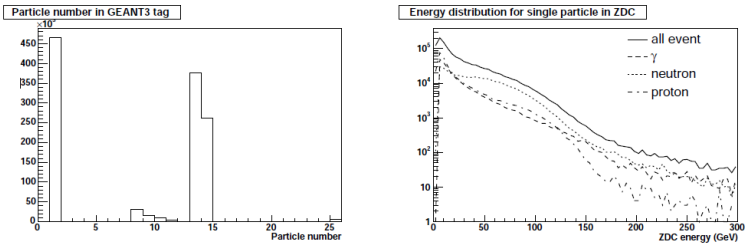

Figure 6.21: The event structure which is detected with the ZDC in pp collision at $\sqrt{s}$=200 GeV was studied by GEANT3 with PYTHIA simulation. The ZDC threshold has set to 5 GeV in the similar to the ZDCN|S trigger. Here, I show the event that one particle is detected with the ZDC in each pp collision (about 92%). The particle tag-number in GEANT3 (summarized in Table 6.1) is plotted in the left. Major particles, the photon, neutron and proton are shown as the tag-number = 1, 13 and 14, respectively. Measured energy distributions for these three particles with the ZDC are plotted in the right figure.

Figure 4.15: Plot from [58], p. 75, figure 6.21. The plot on the lefthand side is used to estimate the fraction of neutrons in the ZDC.

polarization to the function $m\theta$, we find that

$$\epsilon_{++\text{to}--} \approx 2\delta(\theta) = m\theta, \tag{4.27}$$

with $m = -0.044$ mrad^{-1} Plotting this function with the other polarization cases (Fig. 4.14), we see that our linear dependence on P is also confirmed by the simulation.

One last thing to note is that the simulation included only neutron distributions. The actual asymmetry we measure will be different, because the ZDC also detects ample numbers of photons and secondary particles from protons scattering off of the beam pipe. Most conservatively, we can assume that only the neutron component contributes to our A_N, and then dilute our A_N by the fraction of hits in the ZDC that are neutrons, $f_{ZDC}^{neutron}$. This fraction was measured in simulation in [58], see Figure 4.15. Reading off the axis of the plot, we get

- 470 photons for every
- 260 protons,
- 380 neutrons, and
- 30 + 20 + 10 = 60 other particles,

giving

$$f_{ZDC}^{neutron} \approx 380/1170 = 0.32. \tag{4.28}$$

Thus, the simulation predicts that, conservatively,

$$\epsilon_{++\text{to}--} \approx f_{ZDC}^{neutron} m P \theta, \tag{4.29}$$

with $m = -0.044$ mrad^{-1} and $f_{ZDC}^{neutron} \approx 0.32$. If the polarizations of the two beams are unequal, we would expect

$$\epsilon_{++\text{to}--} \approx f_{ZDC}^{neutron} m \frac{(P_B + P_Y)}{2} \theta, \tag{4.30}$$

or

$$\epsilon_{++\text{to}--} \approx -7.04(P_B + P_Y)\theta \tag{4.31}$$

with θ in radians.

4.4.3 Run12 $\sqrt{s} = 200$ GeV Angle Scan

Special Fills

Table 4.4.3 provides the breakdown of the special RHIC fills provided for our scan:

Fill	Spin Pattern	Intended Change of Angle from Nominal
16497	P8	$\Delta = 0$ (but beams steered to be collinear)
16498	P8	$\Delta = 0$ (but beams steered to be collinear)
16502	P5	$\Delta = 120$ urad
16504	P5	$\Delta = 120$ urad
16505	P5	$\Delta = 120$ urad
16506	P5	$\Delta =$ -120 urad
16507	P5	$\Delta =$ -120 urad
16509	P5	$\Delta =$ -120 urad
16511	P5	$\Delta = 0$ (not steered collinear)
16534	P5	$\Delta = 60$ urad (boy we had to push hard for this one!)

BPM data

In order to have data granularity on the run-by-run level, we used the Beam Position Monitors (BPMs) to measure beam angles and offsets. They are read out every four seconds. We took various averages of the BPM data over PHENIX DAQ runs as plotting values, and the standard deviation over said

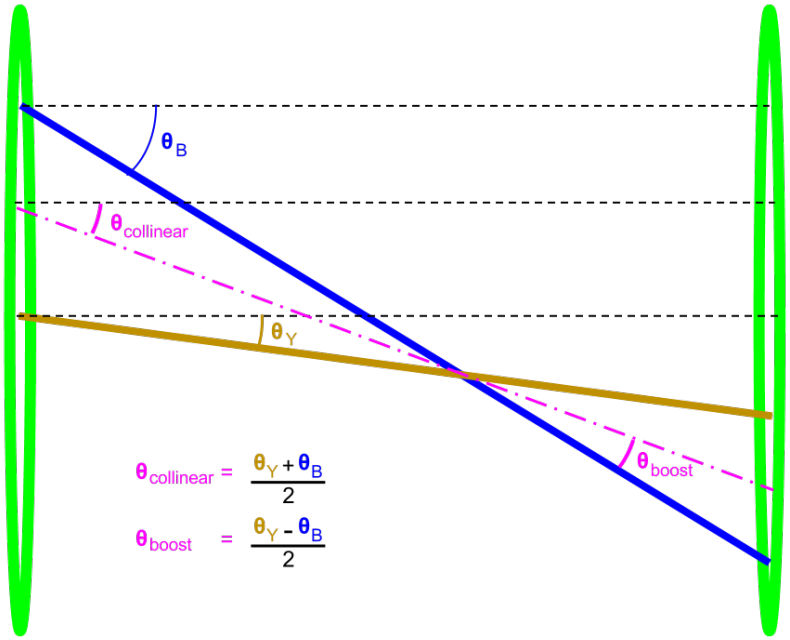

Figure 4.16: Illustration of collinear and boost angle calculations with the blue and yellow beam angles.

runs as the uncertainty on these values. From the difference of readings on the DX.7 and DX.8 BPMs (which are on opposite sides of the IR) we can get the angles through the IR of the blue and yellow beams.

$$\theta_B = atan\left(\frac{(DX.7_B - DX.8_B)}{l_{DX}}\right) \approx \frac{(DX.7_B - DX.8_B)}{l_{DX}}$$
$$\theta_Y = atan\left(\frac{(DX.7_Y - DX.8_Y)}{l_{DX}}\right) \approx \frac{(DX.7_Y - DX.8_Y)}{l_{DX}}, \qquad (4.32)$$

where l_{DX} is the distance from the nominal interaction point to the DX BPMs.

These angles can then be combined to get "collinear angles" and "boost angles" as illustrated in Figure 4.16. Offsets, on the other hand can calculated by averaging $(DX.7_B - DX.8_B)/2$ and $(DX.7_Y - DX.8_Y)/2$, and then can be put on the same "footing" as boosts by dividing by l_{ZDC}, the distance from the interaction point to the ZDCs.

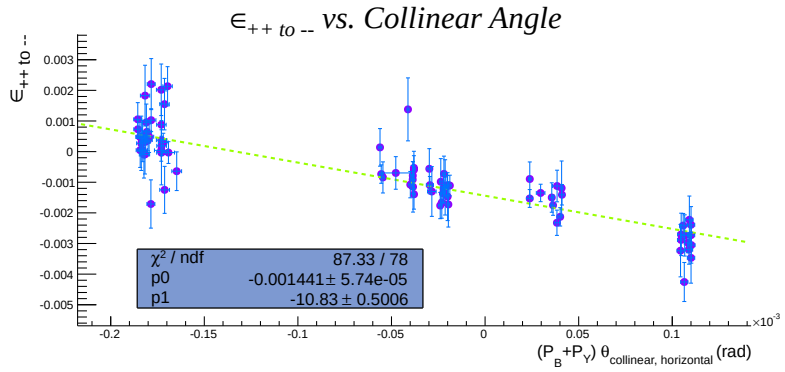

Figure 4.17: Raw "parity violating" asymmetry plotted vs. the horizontal (transverse to the supposed vertical polarization direction) collinear beam angle, polarization included.

4.4.4 Results vs. Collinear Angle

We first plot the results of the angle scan vs. the collinear beam angle, since changing this angle, in the direction perpendicular to the supposed polarization, was the goal of the study. The reduced chi-squared of a linear fit of $\epsilon_{++\text{to}--}$ vs. polarization weighted collinear angle, in Fig. 4.17, is not unreasonable at 1.17. Polarization values are from CNI offline analyses. The slope for this fit is -10.83 ± 0.50 rad^{-1}, which differs from the simulation result of -7.04 rad^{-1} by only 54%, a reasonable difference considering the simulation was conservative and simplistic. The other unphysical asymmetry, $\epsilon_{+-\text{to}-+}$, which is equivalent to rotating the experiment by 180°, was not expected to change as offsets and boosts were not scanned. This asymmetry is shown in Fig. 4.18. Its slope with respect to offsets and boosts is consistent with that of $\epsilon_{++\text{to}--}$ with respect to collinear angle, albeit with less significance. The remaining (non-independent) asymmetries that can be reconstructed from the data are the single spin asymmetries for the yellow and blue beams with the opposite beam spin held constant. They are shown in Figures 4.19 and 4.20. As predicted by the model, each pair of asymmetries has an equal and opposite dependence on the collinear angle, but the average is not zero. In fact, it is about 2×10^{-3}, which is consistent with the ϵ_{TT} found in the rest of the 2012 transverse run at $\sqrt{s} = 200$GeV. Thus the collinear angle scan study still leaves this non-zero asymmetry unexplained. However, insights into the 180° rotation and parity violating asymmetries prevents us from having to add additional systematic uncertainties to our result. For instance, $\epsilon_{++\text{to}--}$ is 1.4×10^{-3} when the BPMs read "zero" collinear angle. If this were attributed

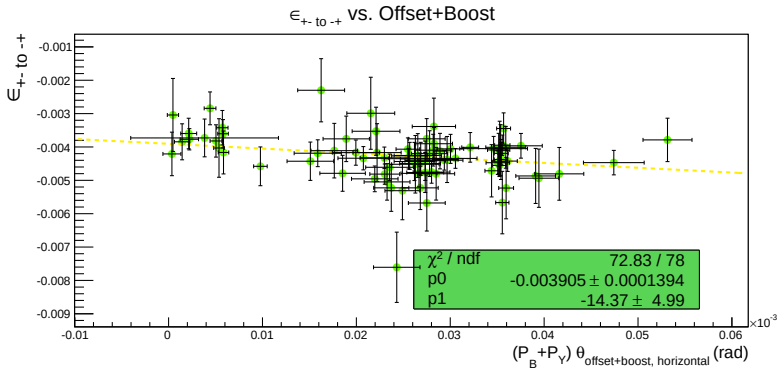

Figure 4.18: Raw "180 degree rotational" asymmetry plotted vs. the horizontal beam offset (normalized to the ZDC distance) plus the boost angle, polarization included.

to a true parity violating asymmetry at 60% transverse polarization, it would result in

$$A_{\text{PV}} = 3.9 \times 10^{-3}, \tag{4.33}$$

a significant violation of parity invariance in the strong interaction, which would deal a serious blow to the credibility of the experiment. Instead, we can satisfactorily explain it with our beam geometry plus transverse single spin asymmetry effect.

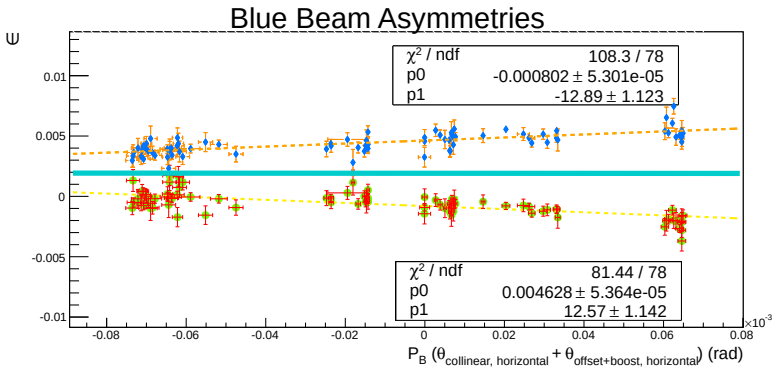

Figure 4.19: Blue beam asymmetries ($--$ to $+-$ and $++$ to $-+$). The slopes are equal and opposite as predicted by the model, but not the y-intercepts.

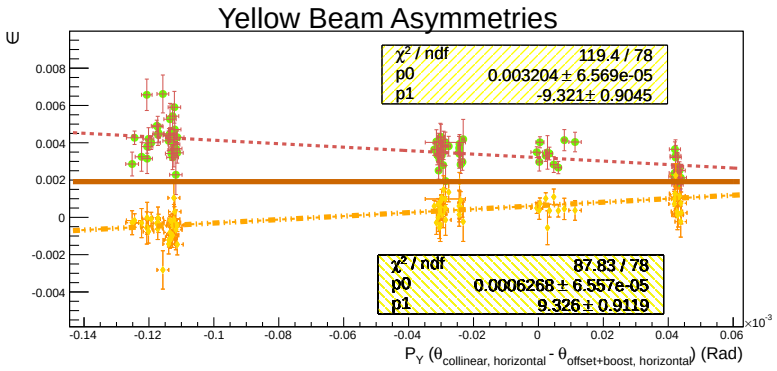

Figure 4.20: Blue beam asymmetries ($++$ to $+-$ and $--$ to $-+$). The slopes are equal and opposite as predicted by the model, but not the y-intercepts.

4.4.5 Rate Safe Relative Luminosity from the 2012 $\sqrt{s} = 200$ GeV Transversely Polarized Run

The remainder of the 2012 $\sqrt{s} = 200$ GeV transversly polarized run is useful for measuring the double spin ZDC to BBC asymmetry with a very high transverse component to the polarization. These raw asymmetries calculated with the $\epsilon_N\epsilon_S\lambda$ method are shown in Fig. 4.21, for which there are four additional spin patterns, added late in the run. This run indeed produced a much higher raw

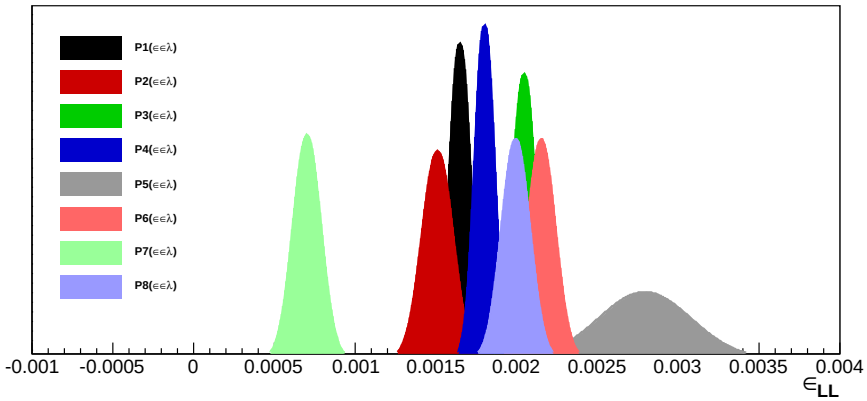

Figure 4.21: Results for the raw ZDC to BBC asymmetry in the 2012 $\sqrt{s} = 200$ GeV transversely polarized run with the $\epsilon_N\epsilon_S\lambda$ method. Four additional spin patterns (P5-P8) were added towards the end of the run. P1, P4, P5 and P8 are all equivalent for a double spin asymmetry, as are P2, P3, P6 and P7.

asymmetry (now labeled ϵ_{TT} to reflect the transverse polarization):

$$\epsilon_{TT} = 1.74 \pm 0.23 \times 10^{-3}, \tag{4.34}$$

where the value is calculated as the error weighted average of the spin pattern results in Fig. 4.21 and the standard deviation of the spin patterns about the mean has been added linearly to the uncertainty. Scaled by the online polarization values (no final values are available at this time) $P_B = 0.61$ and $P_Y = 0.55$, this translates to a whopping

$$A_{TT} = 5.17 \pm 0.67 \times 10^{-3}, \tag{4.35}$$

lending credence to the idea that the transverse polarization may be playing some role in the ZDC to BBC asymmetry. We can also plot ϵ_{TT} throughout the $\sqrt{s} = 200$ GeV runs vs. various combinations of the transverse polarization

component in those runs, as in Fig. 4.22. If ϵ_{TT} were produced via a single spin effect, we would expect it to scale as the average transverse polarization of the two beams, or if it were a double spin effect, with the product of the polarizations. The results, however, are unclear, and although the asymmetry increases with the transverse polarization component, there is no evidence of a linear relationship.

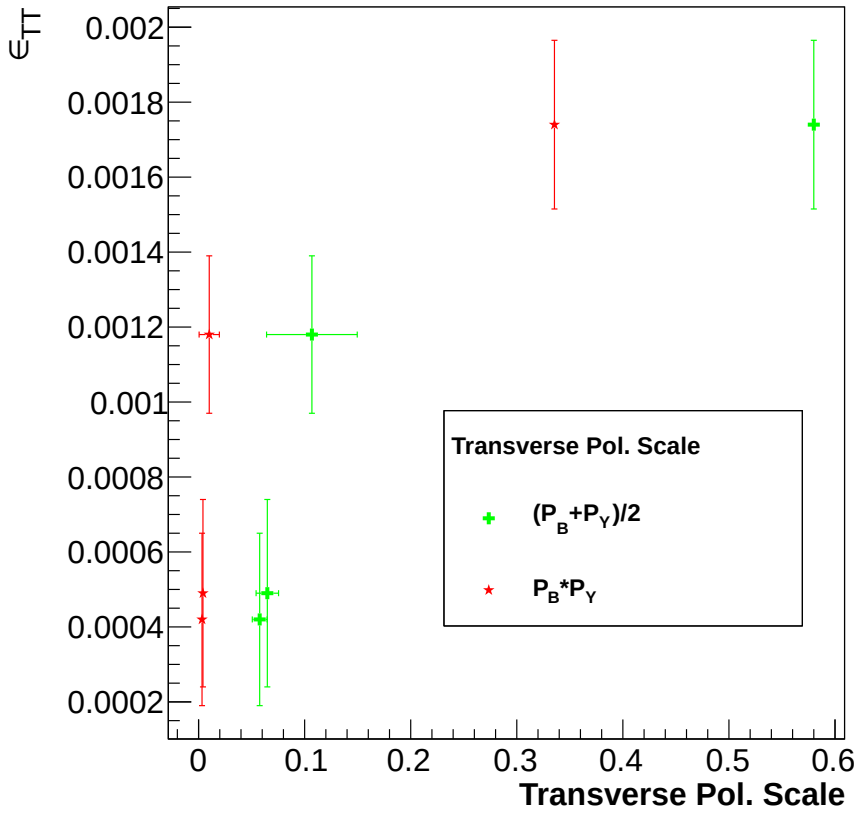

Figure 4.22: The raw double spin ZDC to BBC asymmetry from the 2005, 2006, 2009, and 2012 runs plotted vs. functions of the transverse polarization component in those runs. All but the 2012 data are from Table 4.1, and for the 2012 transverse run no final polarizations or errors are yet available. The ϵ_{TT} of the 2012 data points is the average of the spin patterns in Fig. 4.21, with the standard deviation of the pattern means added linearly to the total uncertainty on ϵ_{TT}.

As a final note, Fig. 4.23 shows ϵ_{TT} plotted vs. runnumber. A clear reduction in the scatter of the fill-by-fill values is seen around run 360500,

which happens to correspond to the time at which the Collider Accelerator Department turned off automatic orbit corrections to the beams. Also, the average value of the raw asymmetry increases at this point. This suggests beam orbit or geometry may also play a role in generating an ϵ_{TT}.

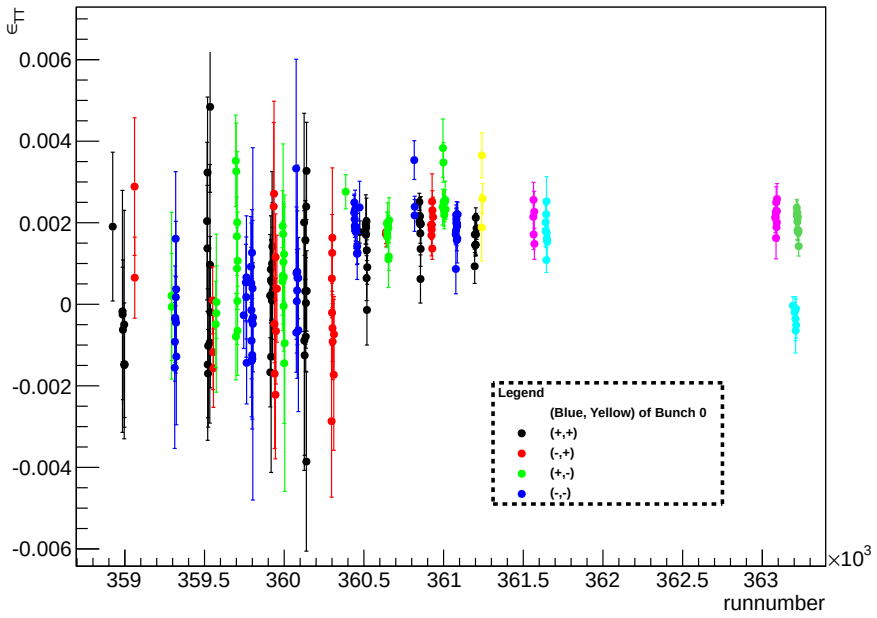

Figure 4.23: Results for the raw ZDC to BBC asymmetry in the 2012 $\sqrt{s} =$ 200 GeV transversely polarized run with the $\epsilon_N \epsilon_S \lambda$ method versus runnumber. The sudden change in the scatter of the points around Run 360500 corresponds to the time at which the Collider Accelerator Department turned off automatic orbit corrections.

4.5 Bunch Fitting Wall Current Monitor Data

Bunch fitting can also be used "un-normalized," that is, without uncertainties, to look for pattern dependent deviations from some average quantity. Fitting to the formula $r_i^{\pm} = c(1 \pm \epsilon)$, as in 4.1, the raw asymmetry ϵ returned is interpretable as the pattern dependent deviation from the average, normalized to the average itself. Figure 4.24 shows the results of this procedure applied to the standard deviations within certain z-vertex ranges of the 2009 wall current monitor data. An example of these standard deviations plotted vs. crossing is given in Fig. 4.25, normalized to crossing zero. To produce these plots, the beam separated wall current monitor data introduced in 2.1.2 was convoluted to produce a plot of of the collision distribution versus z, as in Fig 4.26. β^* effects from the focusing of the beam at the IP were included. Then the $z = 0$ position was calibrated to offline BBC z-vertex measurements, after which the standard deviation of the WCM distributions within certain z ranges could be bunch-fit.

The results of the bunch fitting are quite interesting, showing that there is no significant double spin dependence in the WCM measured bunch width within 50 cm, but there is when calculated within 100 cm, although since the average of of the spin pattern separated results is about 0, it can be attributed to a coincidental alignment of the bunch structure with the bunches selected for a double spin asymmetry analysis (think Fig. 2.3 of 2.1.1), an effect similar to the EMCal previous crossing memory effect of 3.5.1. Since the effect is negligible in 50 cm, it could not affect our 2009 π^0 result, but it could cause some of the bifurcation in the relative luminosity results and in any analysis with a loose z-vertex cut.

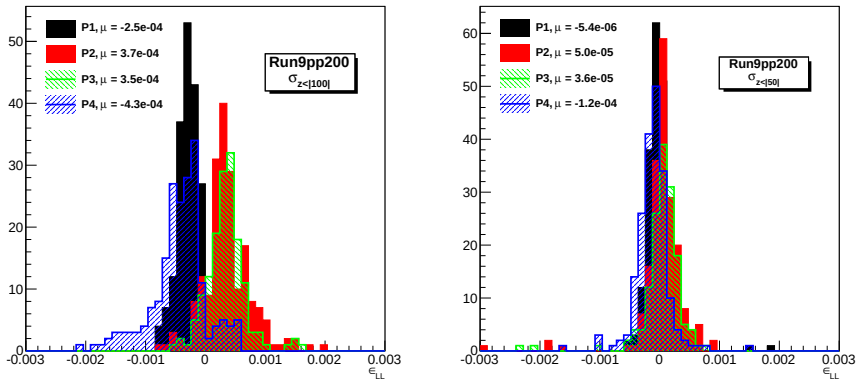

Figure 4.24: Unnormalized bunch fitting applied to the standard deviation of the convoluted WCM distributions within the z-vertex ranges given in the plots.

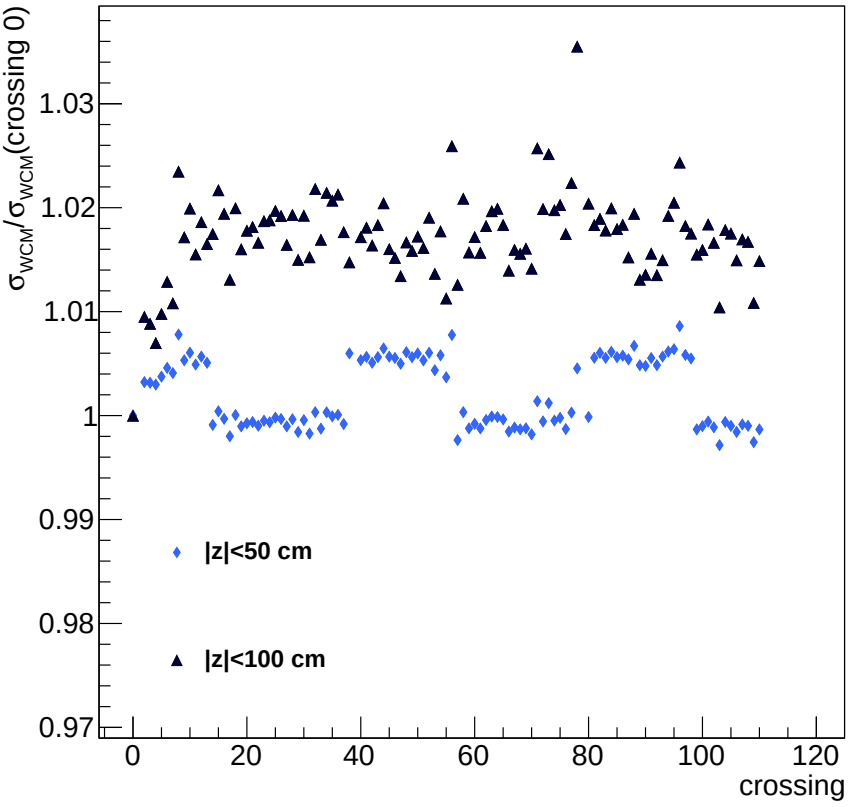

Figure 4.25: The standard deviation of the convoluted WCM distributions within two different z-vertex ranges plotted vs. crossing, normalized to crossing 0.

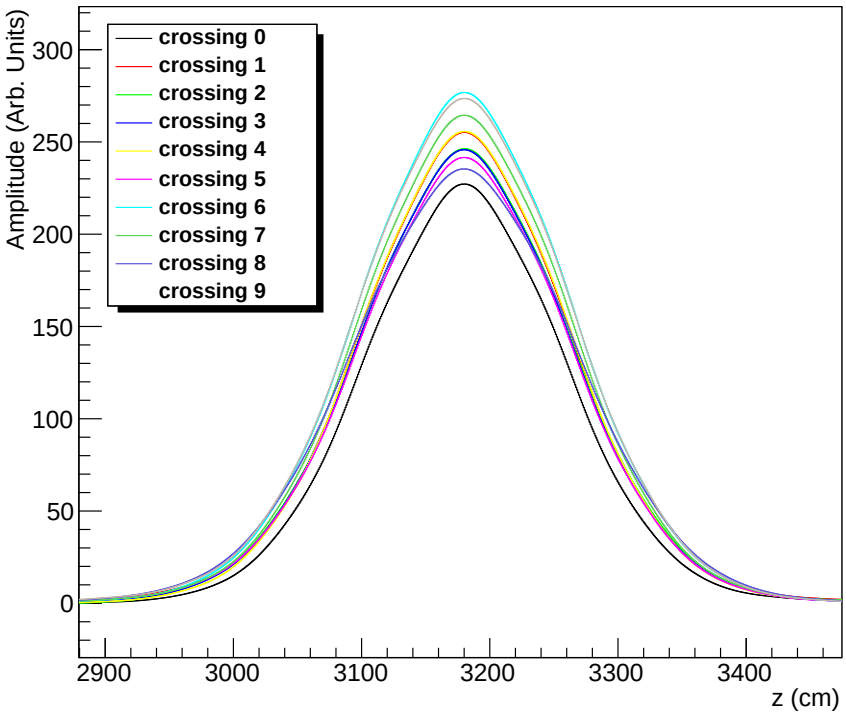

Figure 4.26: Example WCM convolution of the first 10 bunches in each ring, without the $z = 0$ offset applied.

Chapter 5

Final $A_{LL}^{\pi^0}$ Results and Discussion

	2005			2006			2009		
$p_T^{\pi^0}$ bin (GeV/c)	$\langle p_T^{\pi^0} \rangle$ (GeV/c)	$A_{LL}^{\pi^0}$ (10^{-3})	$\Delta A_{LL}^{\pi^0}$ (10^{-3})	$\langle p_T^{\pi^0} \rangle$ (GeV/c)	$A_{LL}^{\pi^0}$ (10^{-3})	$\Delta A_{LL}^{\pi^0}$ (10^{-3})	$\langle p_T^{\pi^0} \rangle$ (GeV/c)	$A_{LL}^{\pi^0}$ (10^{-3})	$\Delta A_{LL}^{\pi^0}$ (10^{-3})
1-1.5	1.29	0.3	1.9	1.30	1.2	1.3	1.30	-0.4	1.3
1.5-2	1.75	1.0	1.3	1.75	1.46	0.82	1.75	-0.19	0.82
2-2.5	2.22	-0.4	1.5	2.23	0.70	0.84	2.23	0.33	0.81
2.5-3	2.72	-1.5	2.0	2.72	0.0	1.1	2.72	0.1	1.0
3-3.5	3.21	5.3	3.0	3.22	-0.6	1.6	3.22	0.5	1.5
3.5-4	3.72	12.9	4.5	3.72	-1.3	2.3	3.72	-1.7	2.2
4-5	4.38	-1.2	5.6	4.38	-0.5	2.9	4.40	3.5	2.5
5-6	5.40	0	11	5.40	9.9	5.7	5.40	-2.1	4.7
6-7	6.41	20	20	6.41	-15	10	6.41	-0.4	8.3
7-9	7.79	23	28	7.74	26	14	7.72	-4	12
9-12	N/A	N/A	N/A	10.0	3	29	10.0	12	23
12-15	N/A	N/A	N/A	N/A	N/A	N/A	13.1	61	69

Table 5.1: π^0 A_{LL} measurements at $\sqrt{s} = 200$ GeV from the 2005, 2006, and 2009 RHIC runs, along with statistical uncertainties. The systematic uncertainties for the three years are:
Relative Luminosity (shift uncertainty): 2.5×10^{-4}, 7.5×10^{-4}, and 13.0×10^{-4}
Polarization (scale uncertainty): 9.4%, 8.3%, and $^{+7.0\%}_{-7.7\%}$.

π^0 A_{LL} values as a function of p_T for the 2009 data set are shown in Figure 5.1 and the values are given in Table 5.1. These results are now published in [7]. The results are compared with previously published results from 2005 [2] and 2006 [4], with which they are consistent. The relative luminosity systematic uncertainty for the 2009 data set is shown only in the inset of Fig. 5.1 but applies to all of the points. The polarization uncertainties discussed above are not shown on the data points but are listed in the legend. The results are consistent in all cases.

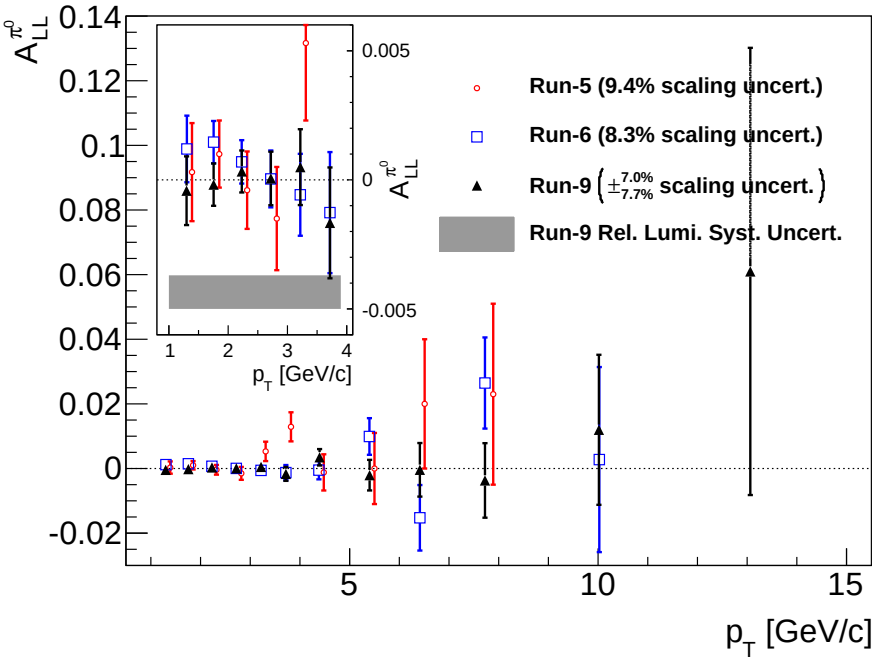

Figure 5.1: A_{LL} vs. p_T for π^0 mesons for the 2005 (red circle), 2006 (blue square) and 2009 (black triangle) PHENIX data sets.

In Fig. 5.2, the 2005, 2006 and 2009 results have been combined for the π^0, taking into account the year-to-year uncorrelated polarization uncertainties and assuming that the relative luminosity uncertainty year-to-year correlation is the maximal overlap in A_{LL}^R across years, 0.42×10^{-3}. The year-to-year correlated part of the polarization uncertainty is given in the legend.

The π^0 asymmetries are consistent with the best fit of a global analysis of DIS data that allows at the input scale only quark contributions to A_{LL}: the GRSV-zero scenario, which assumes $\Delta g(x, \mu^2) = 0$ at an NLO input scale $\mu^2 = 0.40$ GeV^2 [37]. This consistency can be quantified relative to the related

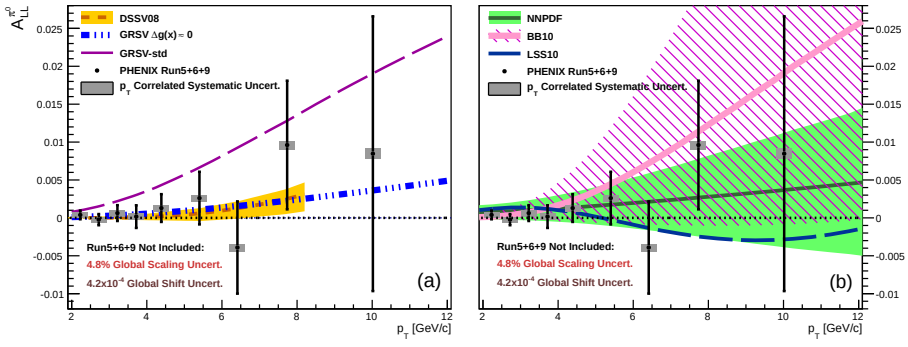

Figure 5.2: Points are the combined A_{LL} vs. p_T for π^0 mesons from 2005 through 2009 with the statistical uncertainty. The p_T correlated systematic uncertainty given by the gray bands is the result of combining the year-to-year uncorrelated parts of the systematic uncertainties on relative luminosity and polarization. The year-to-year correlated parts are given in the legend. Plotted for comparison are several expectations based on fits to polarized scattering data, with uncertainties where available.

GRSV-std scenario, in which the gluon polarization is not fixed (nor is it well constrained). The difference between these two scenarios in a statistical-uncertainty-only comparison to the combined π^0 data in the 2–9 GeV/c p_T range is $(\Delta\chi^2)_{\text{GRSV}}/\text{N.D.F} \equiv ((\chi^2)_{\text{GRSV-std}} - (\chi^2)_{\text{GRSV-zero}})/\text{N.D.F} = 18.9/8$, a 4.3-sigma change. If all of the points are increased by the total systematic uncertainty to move them closer to the GRSV-std curve, the change is 3.3/8 or 1.8 sigma, indicating that the PHENIX π^0 data still prefer the GRSV-zero scenario.

More recent NLO global analyses of DIS-only data by Blümlein and Böttcher (BB10) [21] and Ball et. al. (NNPDF) [17, 18], and of DIS+SIDIS data by Leader et. al. (LSS10) [47] also allow the gluon polarization to be fit by the data, but the analyses vary in ways that affect determination of $\Delta g(x, \mu^2)$. The most significant of these differences is the BB10 assumption of a flavor-symmetric sea versus the separation of flavor-specific distributions made possible in LSS10 by the SIDIS data. This affects the gluon determination not only because of the constraint on the total polarization, but also because the analyses use functional forms for the initial pPDFs such as

$$x\Delta f_i(x, \mu^2) = N_i x^{\alpha_i}(1-x)^{\beta_i}(1 + \gamma_i\sqrt{x} + \eta_i x) \tag{5.1}$$

and consequentially must relate parameters between the sea and gluon distributions to enforce positivity ($|\Delta f_i(x, \mu^2)| \leq f_i(x, \mu^2)$) and to fix poorly-

constrained parameters.

Another issue with making a choice of functional form for $\Delta g(x, \mu^2)$ is that, even with inclusion of present $\vec{p}+\vec{p}$ data, there are no existing measurements that can test the validity of the functional form in the low-x region. For analyses like BB10 and LSS10 that do not include $\vec{p}+\vec{p}$ data, this problem extends to determination of Δg in the medium and large-x regions as well. The NNPDF analysis of DIS data avoids bias introduced in choosing a functional form for the PDFs by using neural networks to control interpolation between different x values. For example, $\Delta g(x, \mu^2)$ is parameterized as

$$\Delta g(x, \mu^2) = (1-x)^m x^{-n} NN_{\Delta g}(x), \tag{5.2}$$

with $NN_{\Delta g}(x)$ a neural network parameterization determined by scanning functional space for agreement with 1000 randomly distributed replicas of the experimental data. The low- and high-x terms are included for efficiency, and in order to ensure that they do not bias the fit, m and n are chosen from a random interval for each experimental data replica such that this interval is wider than the range of effective exponents for the limiting low and high-x behavior after the neural network terms have been included.

Fig. 5.2(b) includes $A_{LL}^{\pi^0}$ predictions based on the BB10, LSS10, and NNPDF polarized PDF determinations. For BB10 and LSS10, we evolved their published polarized PDFs to various μ^2 using the QCD-PEGASUS package [59] and used these to calculate the p_T dependent polarized cross-section for inclusive π^0 production with code based on [43] that uses the DSS NLO fragmentation functions [28]. The unpolarized cross-section for the denominator was calculated via the same two-step process starting from the CTEQ-6 PDFs [54]. The BB10 uncertainty band was calculated using the Heissian method with a set of polarized PDFs obtained from the parameter covariance matrix in the BB10 publication. The NNPDF prediction was provided by that group, using their polarized PDFs supplemented by preliminary W boson asymmetry measurements from the STAR experiment [50, 57]. Neither the BB10 nor NNPDF prediction accounts for uncertainties in the determination of the π^0 fragmentation functions.

One feature of the predictions is that the BB10 uncertainty band is smaller than the NNPDF band at $p_T \approx 3$ GeV/c but quickly exceeds it as p_T increases. Likewise, as can be seen in Ref. [18], at an input scale of 4 GeV^2, the uncertainty on the BB10 prediction for Δg, which neglects bias from the choice of functional form, is smaller than that for NNPDF at low-x but exceeds it as x increases. Future inclusion of the PHENIX $A_{LL}^{\pi^0}$ into the NNPDF analysis may provide some insight into whether or not this is due to a bias in the choice of functional form at medium-x, particularly in the RHIC range of $[0.05, 0.2]$.

The DSSV08 global analysis [29], which is also based on the pPDF parameterizations of Eq. 5.1, includes, in addition to DIS and SIDIS data, preliminary versions of the RHIC data presented in [1, 3, 4]. The results of that analysis, which yields a much more accurate determination of $\Delta g(x)$, are compared with $A_{LL}^{\pi^0}$ in Fig. 5.2(a). An updated version of the DSSV08 analysis was also run to include final versions of the RHIC data through 2006 [1, 3, 4] along with the final $A_{LL}^{\pi^0}$ results presented here. The updated fit obtained $\Delta G^{[0.05,0.2]}_{\rm DSSV08} = 0.06^{+0.04}_{-0.06}(\Delta\chi^2 = 1)^{+0.11}_{-0.15}(\Delta\chi^2 = 9)$, where the $\Delta\chi^2 = 9$ uncertainties roughly correspond to the 2% change in $\Delta\chi^2/\chi^2_{min}$ used to determine the uncertainties in the DSSV08 global analysis. The full $\Delta\chi^2$ curve from our updated analysis is shown as the central curve in Fig. 5.3(b). Fig. 5.3(a) shows the contribution from PHENIX data to that curve, and that data prefers $\Delta G^{[0.05,0.2]}_{\rm PHENIX} = 0.07^{+0.05}_{-0.08}(\Delta\chi^2 = 1)$.

$p_T^{\pi^0}$ bin (GeV/c)	$\langle p_T^{\pi^0} \rangle$ (GeV/c)	$A_{LL}^{\pi^0}$ (10^{-4})	$\Delta A_{LL}^{\pi^0}$(Stat) (10^{-4})	$\Delta A_{LL}^{\pi^0}$(RL Syst) (10^{-4})	$\Delta A_{LL}^{\pi^0}$(Pol. Syst) ($\times A_{LL}^{\pi^0}$)	$\Delta A_{LL}^{\pi^0}$(Tot. Syst) (10^{-4})
1-1.5	1.30	5.1	8.5	3.5	3.4%	3.6
1.5-2	1.75	9.6	5.5	3.3	3.5%	3.3
2-2.5	2.23	3.9	5.8	3.4	3.5%	3.4
2.5-3	2.72	-2.3	7.4	3.6	3.4%	3.7
3-3.5	3.22	6	11	4.0	3.2%	4.0
3.5-4	3.72	2	15	4.1	3.1%	4.1
4-5	4.39	13	18	4.3	3.1%	4.3
5-6	5.40	26	35	4.5	3.0%	4.5
6-7	6.41	-39	61	4.5	2.9%	4.6
7-9	7.74	96	85	4.5	2.9%	5.3
9-12	10.0	80	180	5.8	3.3%	6.5
12-15	13.1	610	690	10	3.0%	21

Table 5.2: Combined π^0 A_{LL} values from the PHENIX datasets at $\sqrt{s} = 200$ GeV. Fully pT correlated systematic uncertainties that are considered uncorrelated by run-year are given in the table. The run-year correlated parts of the polarization scale uncertainty, 4.8%, and the relative luminosity shift uncertainty, 4.2×10^{-4}, are not included.

5.1 Theory Fits

5.1.1 Plotting Theory Fits vs. $A_{LL}^{\pi^0}$

Most groups performing extractions of polarized PDFs from polarized SIDIS, DIS, and/or $p+p$ data, such as [21], quote in their publications polarized PDF parameters and associated uncertainties. If the pPDFs can be cast in one of the forms

$$\begin{aligned} x\Delta f_i(x,\mu_0^2) &= N_i p_{i,1} x^{p_{i,2}}(1-x)^{p_{i,3}}\left[1+p_{i,5}x^{p_{i,4}}+p_{i,6}x\right] \\ x\Delta f_i(x,\mu_0^2) &= N_i p_{i,1} x^{p_{i,2}}(1-x)^{p_{i,3}}\left[1+p_{i,4}\sqrt{x}+p_{i,5}x+p_{i,6}x^{3/2}\right] \end{aligned} \tag{5.3}$$

and the covariance matrix for the parameters is provided, the results can be converted to an $A_{LL}^{\pi^0}$ (or A_{LL} for some other final state if fragmentation functions are available) vs. p_T curve with an uncertainty band using pPDF evolution code from [59] and parton cross-section plus fragmentation function calculation code from [43]. The procedure starts with decorrelating the pPDF parameters.

In order to find an independent set of parameters $\mathbf{x}$, i.e. ones with zero covariance, we need to diagonalize the covariance matrix $\mathbf{C} \equiv E(\mathbf{x}\mathbf{x}^T)$:

$$\mathbf{D} = \mathbf{P}^{-1}\mathbf{C}\mathbf{P}, \tag{5.4}$$

where the columns of P are the linearly independent eigenvectors of C and D is a diagonal matrix made up of the associated eigenvalues. Since the covariance matrix C is by definition symmetric, the matrix P is orthogonal and $P^{-1} = P^T$. The equivalent transformation for a set of pPDF parameters is then

$$\mathbf{y} = \mathbf{P}^T\mathbf{x}. \tag{5.5}$$

We can apply this transformation to the best-fit parameters μ as $\lambda \equiv \mathbf{P}^T\mu$. Assuming the data $\mathbf{y}$ are normally distributed, we can then produce an uncertainty band for A_{LL}. There are two commonly used methods for doing so:

- Monte-Carlo Method:

  Simulate a large sample by distributing each element of $\mathbf{y}$ from a normal distribution with mean from λ and variance from $\mathbf{D}$. This sample can transformed back to the original basis by multiplying by $\mathbf{P}$, after which it can be fed through the evolution and cross-section/fragmentation function codes to produce a distribution of A_{LL} values at various p_T points.

The variance of these A_{LL} distributions can then be extracted and used to draw a p_T dependent uncertainty band. This is essentially the method used by the NNPDF collaboration [18].

- Hessian Method:

  This method requires the creation of n "+" sets and n "−" sets, where n is the number of free parameters in the global analysis. For each $+(-)$ set, one element of $\mathbf{y}$ is fixed at one standard deviation above(below) its mean value, while the remainder are set equal to their mean value. Each of the $2n$ sets is then run through the evolution and cross-section/fragmentation function code to produce sets of A_{LL}^{+} and A_{LL}^{-} curves. The positive and negative uncertainty bands are then computed as

$$\Delta A_{LL}^{+} = \sqrt{\sum_{i=1}^{n} \left[max\left(A_{LL}^{+}(i) - A_{LL}^{central}, A_{LL}^{-}(i) - A_{LL}^{central}, 0 \right) \right]^2}$$
$$\Delta A_{LL}^{-} = \sqrt{\sum_{i=1}^{n} \left[max\left(A_{LL}^{central} - A_{LL}^{+}(i), A_{LL}^{central} - A_{LL}^{-}(i), 0 \right) \right]^2}, \quad (5.6)$$

  where $A_{LL}^{central}$ is determined from the published best-fit parameters. This procedure was applied to the results of [21] to produce the "BB10" curve in Figure 5.2.

5.1.2 Systematics in Global Analysis

Systematic uncertainties for the RHIC dataset were not included in the DSSV08 analysis. However, the PHENIX relative luminosity systematic uncertainty now exceeds the statistical uncertainty on $A_{LL}^{\pi^0}$ in the lowest p_T bins. To understand the impact of this on the fit result, we shifted the PHENIX $\sqrt{s} =$ 200 GeV data up and down by the systematic uncertainties given in the final column of Table 5.2, while ignoring the systematic uncertainties of all other datasets. As demonstrated in Fig. 5.3, this changes the global best-fit value to 0.12 or 0.02, with the value preferred by the PHENIX data changing to 0.17 or −0.03. It is therefore necessary to include this uncertainty in future global analyses in order to get accurate determinations of ΔG.

The relative luminosity systematic uncertainty is even more impactful when the preliminary 2009 $\sqrt{s} = 200$ GeV STAR jet asymmetry results [31] are

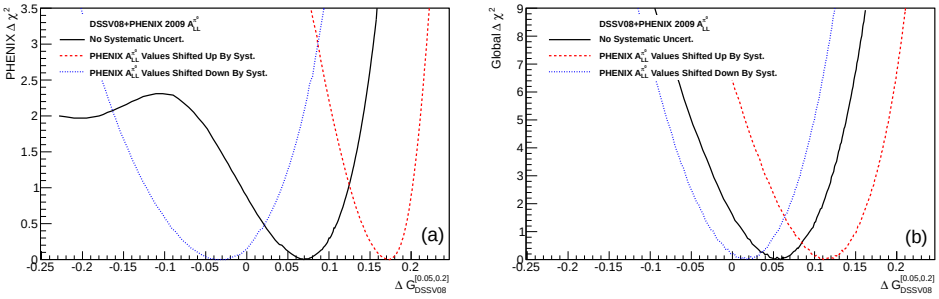

Figure 5.3: (a) Contribution of the combined PHENIX data at $\sqrt{s} = 200$ GeV to the global χ^2 of the DSSV08 analysis using only statistical uncertainties. The different curves show the effect of shifting only the PHENIX data points up or down by their total systematic uncertainty, which is p_T correlated. (b) The effect of shifting only the PHENIX $\sqrt{s} = 200$ GeV data points on the DSSV08 global χ^2.

added to the global analysis. With no relative luminosity systematic uncertainty included, the fit would seem to indicate a significantly non-zero ΔG in the RHIC Bjorken-x range. However, when the values are shifted down by the relative luminosity systematic uncertainty, zero lies within a statistical uncertainty $\Delta\chi^2 = 1$.

5.1.3 Conclusions

Three years worth of $A_{LL}^{\pi^0}$ measurements by PHENIX have put significant constraints on the gluon's contribution to the proton spin. When including other RHIC data, as in the upcoming DSSV global analysis [30], statistical-uncertainty-only analysis points to a significantly non-zero ΔG in the measured range. However, it has been demonstrated herein that this conclusion is incorrect, and that the relative luminosity uncertainty needs to be included in any global analysis, to say nothing about theoretical uncertainties that may have been missed or ignored. Ultimately, to get a truly satisfactory answer on ΔG, measurements need to be made at lower Bjorken-x, such as with an Electron Ion Collider. Nonetheless, the current answer provided by RHIC data could be greatly improved by understanding and eliminating the relative luminosity systematic uncertainty on the existing data. The studies herein have gone part way down that path, but there are many unanswered questions that need additional data or insight to answer.

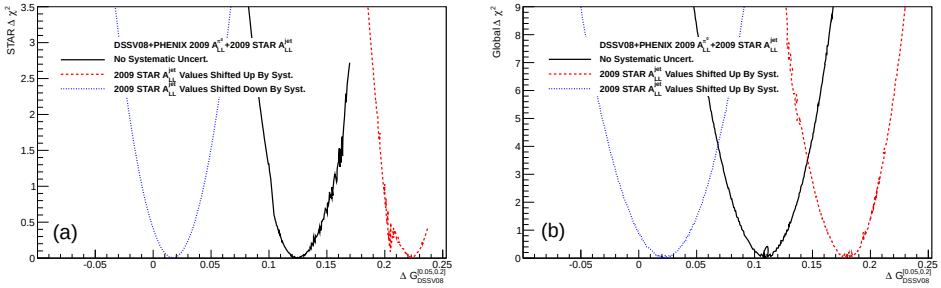

Figure 5.4: (a) Contribution of the STAR data at $\sqrt{s} = 200$ GeV to the global χ^2 of the DSSV08 analysis using only statistical uncertainties. The different curves show the effect of shifting only the 2009 STAR data points up or down by their (preliminary) relative luminosity systematic uncertainty of 2.9×10^{-3}, which is p_T correlated. (b) The effect of shifting only the 2009 STAR data points on the DSSV08 global χ^2.

Appendices

Appendix A

Appendices

A.1 Alternative Approach to k-Factors

Suppose we measure $N_{\gamma\gamma}$ di-photon pairs in N_{ev} events (In this case we do not require a di-photon for the trigger. Think, for example, di-photon pairs in minimum bias events). The joint probability distribution for these quantities is

$$P(N_{\gamma\gamma} = k \text{ and } N_{ev} = n) = P(N_{\gamma\gamma} = k | N_{ev} = n) P(N_{ev} = n). \tag{A.1}$$

$P(N_{ev} = n)$ is a simple Poisson distribution. $P(N_{\gamma\gamma} = k | N_{ev} = n)$ can be derived from the fact that number of di-photon pairs in each single event follows a Poisson distribution, and thus $P(N_{\gamma\gamma} = k | N_{ev} = n)$ is that of a sum of Poisson variables. So we have

$$P(N_{\gamma\gamma} = k \text{ and } N_{ev} = n) = \frac{(n\lambda_{\gamma\gamma/ev})^k e^{-(n\lambda_{\gamma\gamma/ev})}}{k!} \frac{\lambda_{ev}^n e^{-\lambda_{ev}}}{n!}. \tag{A.2}$$

where $\lambda_{\gamma\gamma/ev}$ is the expected number of di-photon pairs per event, and λ_{ev} is the expected number of events. If we want the distribution for $N_{\gamma\gamma}$ regardless of N_{ev}, we sum the joint probability distribution over n.

$$\begin{aligned} P(N_{\gamma\gamma} = k) &= \frac{\lambda_{\gamma\gamma/ev}^k}{k!} e^{-\lambda_{ev}} \sum_{n=0}^{\infty} \frac{n^k \lambda_{ev}^n \left(e^{-\lambda_{\gamma\gamma/ev}}\right)^n}{n!} \\ &= \frac{\lambda_{\gamma\gamma/ev}^k}{k!} e^{-\lambda_{ev}} \frac{T_k(\lambda_{ev} e^{-\lambda_{\gamma\gamma/ev}})}{e^{-(\lambda_{ev} e^{-\lambda_{\gamma\gamma/ev}})}}, \end{aligned} \tag{A.3}$$

where $T_k(x)$ is a Touchard polynomial, defined as

$$T_k(x) = e^{-x} \sum_{n=0}^{\infty} \frac{x^n n^k}{n!}. \tag{A.4}$$

We can use this result to calculate the variance for $N_{\gamma\gamma}$. First we need $E(N_{\gamma\gamma})$.

$$\begin{aligned} E(N_{\gamma\gamma}) &= \sum_{k=0}^{\infty} k \frac{\lambda_{\gamma\gamma/ev}^k}{k!} e^{-\lambda_{ev}} \frac{T_k(\lambda_{ev} e^{-\lambda_{\gamma\gamma/ev}})}{e^{-(\lambda_{ev} e^{-\lambda_{\gamma\gamma/ev}})}} \\ &= \frac{\lambda_{\gamma\gamma/ev} e^{-\lambda_{ev}}}{e^{-(\lambda_{ev} e^{-\lambda_{\gamma\gamma/ev}})}} \sum_{k=1}^{\infty} \frac{\lambda_{\gamma\gamma/ev}^{(k-1)}}{(k-1)!} T_k(\lambda_{ev} e^{-\lambda_{\gamma\gamma/ev}}) \\ &= \frac{\lambda_{\gamma\gamma/ev} e^{-\lambda_{ev}}}{e^{-(\lambda_{ev} e^{-\lambda_{\gamma\gamma/ev}})}} \sum_{k=0}^{\infty} \frac{\lambda_{\gamma\gamma/ev}^k}{k!} T_{k+1}(\lambda_{ev} e^{-\lambda_{\gamma\gamma/ev}}) \end{aligned} \tag{A.5}$$

To reduce this formula, we will need the following identity:

$$\sum_{k=0}^{\infty} \frac{t^k}{k!} T_{k+1}(x) = x e^{-x} e^t e^{x e^t}, \tag{A.6}$$

which can be derived by re-inserting the definition for T and explicity carrying out the summation. Using this identity with the above, we arrive at

$$\begin{aligned} E(N_{\gamma\gamma}) &= \frac{\lambda_{\gamma\gamma/ev} e^{-\lambda_{ev}}}{e^{-(\lambda_{ev} e^{-\lambda_{\gamma\gamma/ev}})}} \\ &* \left(\lambda_{ev} e^{-\lambda_{\gamma\gamma/ev}} e^{-(\lambda_{ev} e^{-\lambda_{\gamma\gamma/ev}})} e^{\lambda_{\gamma\gamma/ev}} e^{(\lambda_{ev} e^{-\lambda_{\gamma\gamma/ev}}) e^{\lambda_{\gamma\gamma/ev}}} \right) \\ &= \lambda_{\gamma\gamma/ev} \lambda_{ev}, \end{aligned} \tag{A.7}$$

as expected. Now we calculate $E(N_{\gamma\gamma}^2)$. Following the steps in Equation A.7, we can reduce it to

$$E(N_{\gamma\gamma}^2) = \frac{\lambda_{\gamma\gamma/ev} e^{-\lambda_{ev}}}{e^{-(\lambda_{ev} e^{-\lambda_{\gamma\gamma/ev}})}} \sum_{k=0}^{\infty} \frac{(k+1)\lambda_{\gamma\gamma/ev}^k}{k!} T_{k+1}(\lambda_{ev} e^{-\lambda_{\gamma\gamma/ev}}) \tag{A.8}$$

From here we break apart $(k+1)$. The 1 gives us the same result as before $(\lambda_{\gamma\gamma/ev}\lambda_{ev})$, and for the k term we pull out another factor of $\lambda_{\gamma\gamma/ev}$ and re-index,

resulting in

$$E(N_{\gamma\gamma}^2) = \lambda_{\gamma\gamma/ev}\lambda_{ev} + \frac{\lambda_{\gamma\gamma/ev}^2 e^{-\lambda_{ev}}}{e^{-(\lambda_{ev}e^{-\lambda_{\gamma\gamma/ev}})}} \sum_{k=0}^{\infty} \frac{\lambda_{\gamma\gamma/ev}^k}{k!} T_{k+2}(\lambda_{ev}e^{-\lambda_{\gamma\gamma/ev}}) \tag{A.9}$$

To sum, we use a result similar to Equation:

$$\sum_{k=0}^{\infty} \frac{t^k}{k!} T_{k+2}(x) = (1 + xe^t)xe^{-x}e^t e^{xe^t} \tag{A.10}$$

Plugging this into the above, we again get massive cancellations like before. The factor $(1 + xe^t) = 1 + \lambda_{ev}$, and so

$$E(N_{\gamma\gamma}^2) = \lambda_{\gamma\gamma/ev}\lambda_{ev} + \lambda_{\gamma\gamma/ev}^2\lambda_{ev}(1 + \lambda_{ev}) \tag{A.11}$$

The variance is then

$$E(N_{\gamma\gamma}^2) - E(N_{\gamma\gamma})^2 = \lambda_{\gamma\gamma/ev}\lambda_{ev} + \lambda_{\gamma\gamma/ev}^2\lambda_{ev}, \tag{A.12}$$

or, estimated from the measurement,

$$\sigma_{N_{\gamma\gamma}}^2 = N_{\gamma\gamma} + \frac{N_{\gamma\gamma}^2}{N_{ev}}. \tag{A.13}$$

Since the measured $N_{\gamma\gamma}$ would be the same if a di-photon trigger requirement were added in addition to the minimum bias trigger for an event (as long as all di-photons were required to meet the same requirement as the trigger), $\sigma_{N_{\gamma\gamma}}$ must also be numerically equal in this case. So, for example, in the $\pi^0 A_{LL}$ analysis where we require a minbias trigger in coincidence with an ERT trigger for our event sample, and also require (essentially) that all di-photon pairs contain a photon that triggered the ERT, we should calculate $\sigma_{N_{\gamma\gamma}}$ in this way.

A.2 Systematics in Global Analysis

In general, for fits to data where each point is not describable as a normally distributed random variable independent from the other points (e.g., the measurement follows the product distribution, or there is a correlated systematic uncertainty), the method of minimizing χ^2, which is based on this assumption, can not be expected to lead to accurate, unbiased determination of the fit uncertainties. Therefore, some other procedure, such as a maximum likelihood

estimation, should be used.

Nonetheless, some global analyses still use the χ^2 method, perhaps because their first incarnations ignored systematic uncertainties and thus the analysis code was written around the acceptable χ^2 treatment of the statistical errors.

It has been noted [S. Baker and R. D. Cousins, 'Clarification of the Use of Chi-Square and Likelihood Functions in Fits to Histograms' Nucl. Instrum. Meth. A221 437 (1984)] that for a set of n independent normal random variables $\{x_i\}$ with expectation values given by a set of functions $\{y_i(\theta)\}$ with parameters θ, the χ^2 function is related to the log likelihood function by

$$\chi^2 = -2ln(L(\theta|\{x_i\})/L_0), \tag{A.14}$$

where L_0 is essentially a normalization term, found by setting the $\{x_i\}$ equal to the $y_i(\theta)\}$. The full derivation is as follows:

$$\begin{aligned} L(\theta|\{x_i\}) &= \frac{1}{(2\pi)^{n/2}\prod_i \sigma_i} e^{-\sum_i \frac{(x_i - y_i(\theta))^2}{2\sigma_i^2}} \\ &\Rightarrow \quad L_0 = \frac{1}{(2\pi)^{n/2}\prod_i \sigma_i} \\ &\Rightarrow \quad ln(L(\theta|\{x_i\})/L_0) = ln(e^{-\sum_i \frac{(x_i - y_i(\theta))^2}{2\sigma_i^2}}) \\ &= -\sum_i \frac{(x_i - y_i(\theta))^2}{2\sigma_i^2} = -\frac{1}{2}\chi^2 \end{aligned} \tag{A.15}$$

One can use this relation to construct a χ^2 function for any likelihood function, however, there is no guarantee that the resultant χ^2 will follow the χ^2 distribution.

Consider the case of a normalization factor that applies across all data points with expected value 1 and uncertainty ϵ. This can be achieved in practice by multiplying each datapoint by the expectation value of the normalization, in which case ϵ corresponds to the relative uncertainty on the unfactored normalization. We can use the following likelihood function:

$$L(\theta|\{x_i\}) = P(\alpha)P(\{x_i\}|\alpha, \theta), \tag{A.16}$$

where α encapsulates deviation of the normalization factor from 1. If we assume both probability distributions are normal, this function becomes

$$
\begin{aligned}
L(\theta|\{x_i\}) &= \left[\frac{1}{\sqrt{2\pi}\epsilon}e^{-\frac{(1-\alpha)^2}{2\epsilon^2}}\right]\left[\frac{1}{(2\pi)^{n/2}\prod_i \sigma_i}e^{-\sum_i \frac{(x_i-\alpha y_i(\theta))^2}{2\sigma_i^2}}\right], \\
L_0 &= \left[\frac{1}{\sqrt{2\pi}\epsilon}\right]\left[\frac{1}{(2\pi)^{n/2}\prod_i \sigma_i}\right] \qquad \text{(A.17)}
\end{aligned}
$$

where, again, ϵ is equal to the fractional normalization uncertainty $\sigma_N/\langle N\rangle$ since we pulled out a factor $\langle N\rangle$ to make $\langle\alpha\rangle = 1$. The corresponding χ^2 function is then

$$
\chi^2 = \frac{(1-\alpha)^2}{\epsilon^2} + \sum_i \frac{(x_i - \alpha y_i(\theta))^2}{\sigma_i^2}. \qquad \text{(A.18)}
$$

To handle a correlated systematic shift across all data values, assumed to be uniformly distributed with expected value 0 and standard deviation $2\delta/\sqrt{12}$, one would use the likelihood function

$$
\begin{aligned}
L(\theta|\{x_i\}) &= [\mathcal{U}(-\delta,\delta)]\left[\frac{1}{(2\pi)^{n/2}\prod_i \sigma_i}e^{-\sum_i \frac{(x_i-\alpha y_i(\theta))^2}{2\sigma_i^2}}\right], \\
L_0 &= \left[\frac{1}{2\delta}\right]\left[\frac{1}{(2\pi)^{n/2}\prod_i \sigma_i}\right] \qquad \text{(A.19)}
\end{aligned}
$$

and a corresponding χ^2 function

$$
\chi^2 = \begin{cases} \sum_i \frac{(x_i-(y_i(\theta)-\beta))^2}{\sigma_i^2} & |\beta| < \delta \\ \infty & |\beta| > \delta \end{cases} \qquad \text{(A.20)}
$$

If the shift uncertainty is instead distributed normally with standard deviation δ, the corresponding χ^2 function would be

$$
\chi^2 = \frac{\beta^2}{\delta^2} + \sum_i \frac{(x_i - (y_i(\theta)-\beta))^2}{\sigma_i^2}. \qquad \text{(A.21)}
$$

PHENIX A_{LL} measurements have multiple sources of normalization and shift uncertainties, which can be categorized as follows:

- (A, ϵ_A) Year-to-year fully correlated part of the normalization uncertainty. To the extent that non-linear effects can be ignored, ϵ_A is equal to the fractional uncertainty on the polarization, since $\Delta\frac{1}{P_B P_Y} \approx \frac{\Delta P_B P_Y}{(P_B P_Y)^2}$ from linear error propagation.

- $(\alpha_y, \epsilon_{\alpha,y})$ Year-to-year uncorrelated part of the normalization uncertainty.
- $(B, \delta B)$ Year-to-year fully correlated part of the relative luminosity shift uncertainty, considered uniformly distributed according to $\mathcal{U}(-\delta B, \delta B)$. δB is set to the maximal overlap of each years measurement, neglecting correlation between δB and $\{\epsilon_{\alpha,y}\}$.
- $(\beta_{\mathcal{U},y}, \delta\beta_{\mathcal{U},y})$ Remaining part of each year y's relative luminosity shift uncertainty after subtraction of the correlated part. Considered uniformly distributed.
- $(\beta_{\mathcal{N},y}, \sigma\beta_{\mathcal{N},y})$ Shift due to the statistical uncertainty on each years relative luminosity systematic uncertainty measurement, which is normally distributed.

One should note that normalization uncertainties also apply to the shift uncertainties, multiplying both the parameters, $B, \beta_{\mathcal{U},y}, \beta_{\mathcal{N},y}$, and the uncertainties, $\delta B, \delta\beta_{\mathcal{U},y}, \delta\beta_{\mathcal{N},y}$ so that any explicit dependence is canceled. The likelihood function for including all of these uncertainties is of the form

$$P(A)P(\{\alpha_y\})P(B|A)P(\{\beta_{\mathcal{U},y}\}|A,\{\alpha_y\})P(\{\beta_{\mathcal{N},y}\}|A,\{\alpha_y\})P(\{x_i\}|A,\{\alpha_y\},B,\{\beta_{\mathcal{U},y}\},\{\beta_{\mathcal{N},y}\}). \tag{A.22}$$

The corresponding χ^2 function is

$$\frac{(A-1)^2}{\epsilon_A^2}+\sum_y \frac{(\alpha_y - A)^2}{\epsilon_{\alpha,y}^2}+\sum_y \frac{\beta_{\mathcal{N},y}^2}{\sigma\beta_{\mathcal{N},y}^2}+\sum_y \sum_{i\in\{p_T\}} \frac{(x_i - A\alpha_y(y_i(\theta)-\beta_{\mathcal{U},y}-\beta_{\mathcal{N},y})+AB)^2}{\sigma_i^2} \tag{A.23}$$

for $|B| < \delta B$, where, again, we have neglected the correlation between δB and $\{\epsilon_{\alpha,y}\}$, which would only be explicit in the last term. The treatment of the normalization uncertainties as a product $A\alpha_y$ is justified by noting that for a product of independent normally distributed random variables with means 1, the variance is $\epsilon_A^2+\epsilon_\alpha^2+\epsilon_A^2\epsilon_\alpha^2$, for which $\epsilon_A^2+\epsilon_\alpha^2$, the total quoted normalization uncertainty in each year, is a close approximation.

A.3 Di-photon Yields and Background Fractions

Below are tables giving the di-photon yields in the signal and sideband regions, as well as the background fraction in the peak region.

A.4 Single Spin Asymmetries

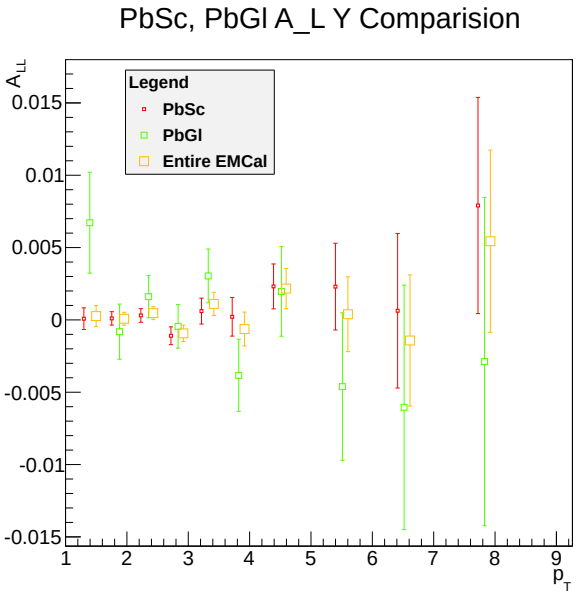

Figure A.1: A_L Yellow calculated in PbSc and PbGl separately, along with in the full detector

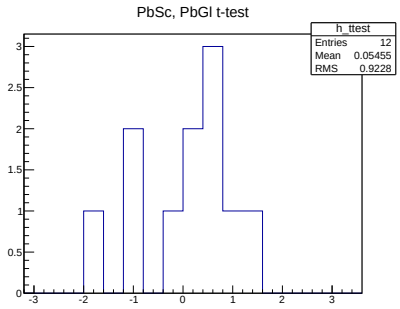

Figure A.2: Student T-scores between A_L Yellow calculated in PbSc and PbGl separately.

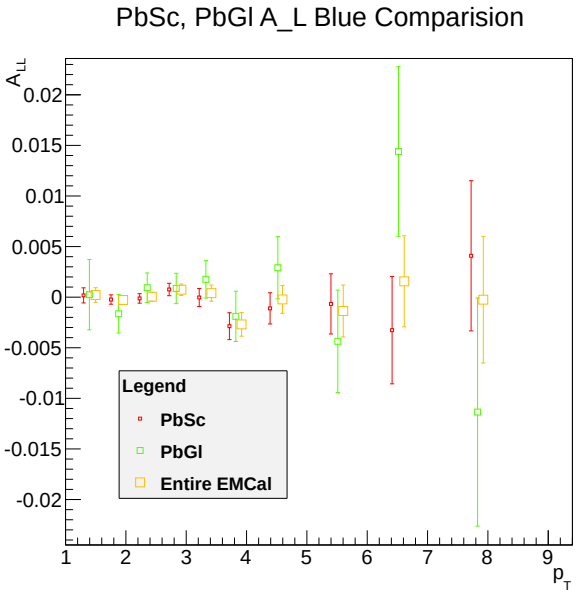

Figure A.3: A_L Blue calculated in PbSc and PbGl separately, along with in the full detector

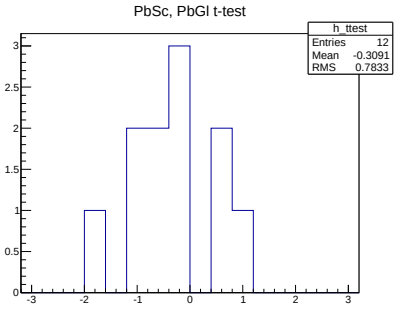

Figure A.4: Student T-scores between A_L Blue calculated in PbSc and PbGl separately.

p_T (GeV)	Fill Pat.	Peak Yield	SB Yield	% Background
1-1.5	P1	5797652	4930912	48.9559
	P2	5502569	4718944	49.2596
	P3	4375075	3727233	48.9348
	P4	5627497	4795432	48.8715
1.5-2	P1	8148556	4832443	33.7167
	P2	7800500	4654951	33.8748
	P3	6134114	3637125	33.7481
	P4	7828349	4625577	33.6399
2-2.5	P1	5628976	2240478	22.894
	P2	5420461	2169783	23.0129
	P3	4231147	1690131	22.8918
	P4	5385276	2141393	22.8433
2.5-3	P1	2798721	792482	16.498
	P2	2703051	769945	16.5963
	P3	2104619	597493	16.5879
	P4	2676033	756543	16.5094
3-3.5	P1	1255717	282611	13.3338
	P2	1215351	274097	13.3415
	P3	945997	212117	13.2013
	P4	1199321	269042	13.2846
3.5-4	P1	558260	109093	11.4973
	P2	539371	106252	11.699
	P3	418297	82335	11.6615
	P4	531294	104174	11.6208
4-5	P1	326942	62718	11.4589
	P2	316236	61510	11.401
	P3	245537	46897	11.27
	P4	311385	60379	11.4876
5-6	P1	91144	15807	10.5607
	P2	88322	15366	10.4602
	P3	68484	11725	10.3526
	P4	86983	15159	10.5733
6-7	P1	29156	4668	9.87413
	P2	28454	4636	10.341
	P3	22039	3519	9.81363
	P4	27878	4681	10.2087
7-9	P1	15325	2389	9.70437
	P2	14557	2432	10.4375
	P3	11336	1768	9.7381
	P4	14699	2432	10.4218
9-12	P1	14003	1982	9.19464
	P2	12412	1777	9.00282
	P3	12412	1777	9.00282
	P4	14003	1982	9.19464
12-15	P1	1437	200	5.85028
	P2	1079	206	5.09793
	P3	1079	206	5.09793

p_T (GeV)	Fill Pat.	Peak Yield	SB Yield	% Background
1-1.5	P1	5559198	4731529	48.8578
	P2	5249344	4506614	49.2795
	P3	4412889	3761371	48.9953
	P4	5558672	4713832	48.8218
1.5-2	P1	7781353	4603277	33.5954
	P2	7510003	4477320	33.8278
	P3	6140818	3636843	33.6993
	P4	7745274	4576277	33.603
2-2.5	P1	5367614	2134592	22.9129
	P2	5229458	2094799	23.0265
	P3	4219662	1683983	22.9518
	P4	5332466	2117408	22.8398
2.5-3	P1	2670465	756873	16.5296
	P2	2609588	742183	16.6142
	P3	2091641	591908	16.5295
	P4	2645575	748587	16.5296
3-3.5	P1	1199359	269671	13.2612
	P2	1172322	264236	13.3266
	P3	936355	210078	13.3062
	P4	1186368	265108	13.2271
3.5-4	P1	530093	103710	11.617
	P2	520880	102180	11.6295
	P3	414343	81441	11.6665
	P4	526235	102720	11.6552
4-5	P1	311466	59936	11.457
	P2	305196	58660	11.3703
	P3	243569	47141	11.3327
	P4	308590	59735	11.3851
5-6	P1	87102	15100	10.6201
	P2	85676	14775	10.6227
	P3	67817	11926	10.6923
	P4	85750	14922	10.5702
6-7	P1	27815	4709	10.3118
	P2	27167	4537	9.94944
	P3	21579	3579	10.3567
	P4	27756	4476	10.1391
7-9	P1	14444	2318	10.168
	P2	14145	2208	9.76079
	P3	11337	1811	10.0488
	P4	14540	2331	10.0433
9-12	P1	14003	1982	9.19464
	P2	12412	1777	9.00282
	P3	12412	1777	9.00282
	P4	14003	1982	9.19464
12-15	P1	1437	200	5.85028
	P2	1079	206	5.09793
	P3	1079	206	5.09793

A.5 Plots of Background Asymmetry vs. Invariant Mass

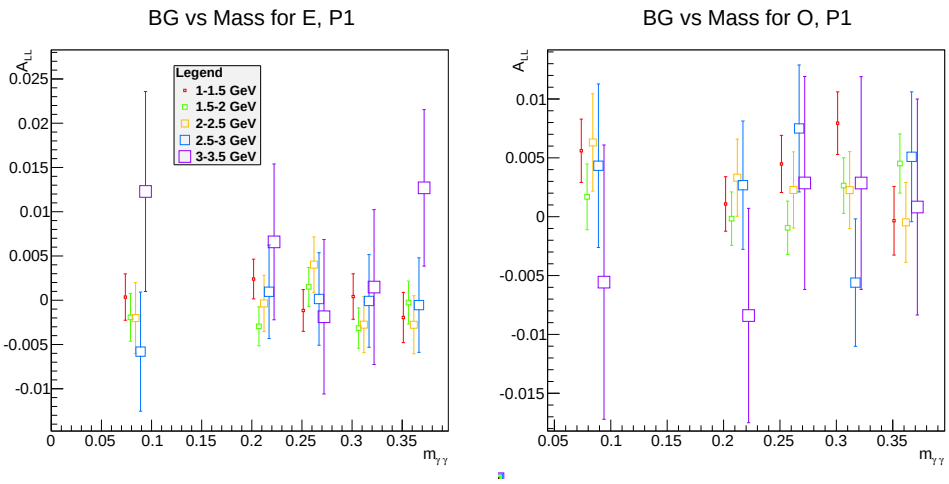

Figure A.5: BG A_{LL}'s mass for fill pattern 1 in *even* crossings (left) and *odd* crossings (right)

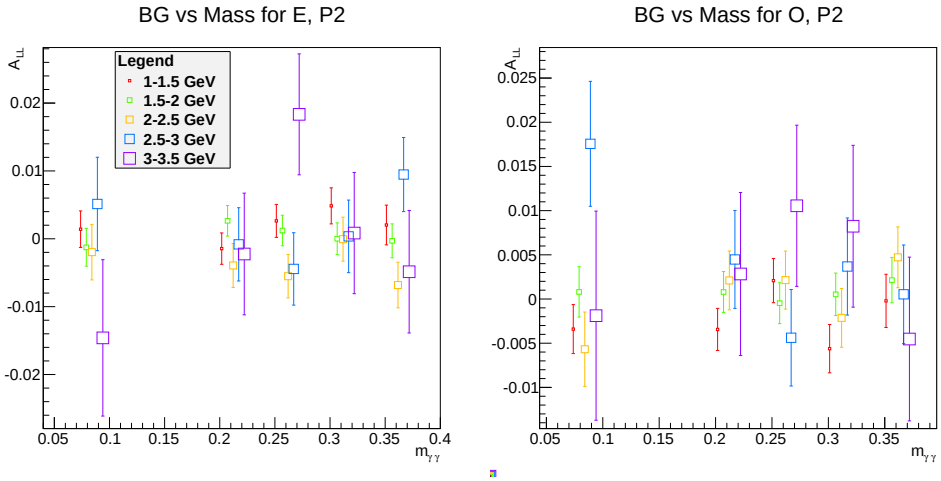

Figure A.6: BG A_{LL}'s mass for fill pattern 2 in *even* crossings (left) and *odd* crossings (right)

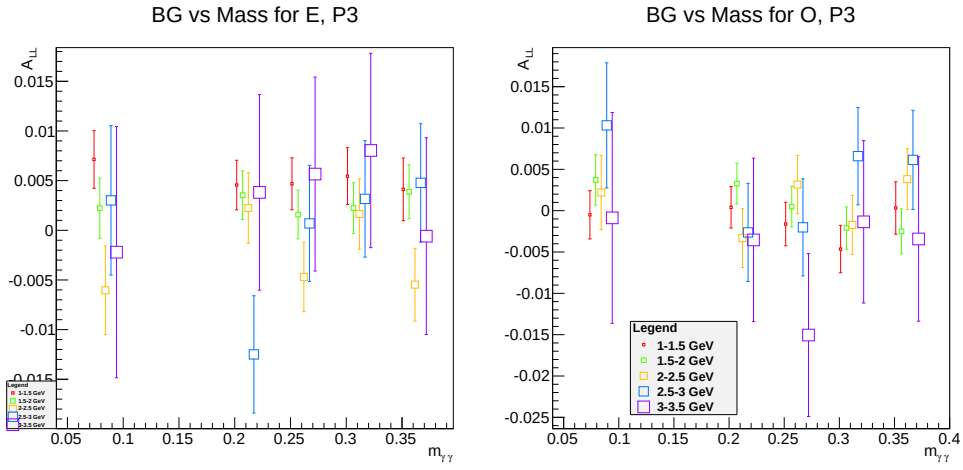

Figure A.7: BG A_{LL}'s mass for fill pattern 3 in *even* crossings (left) and *odd* crossings (right)

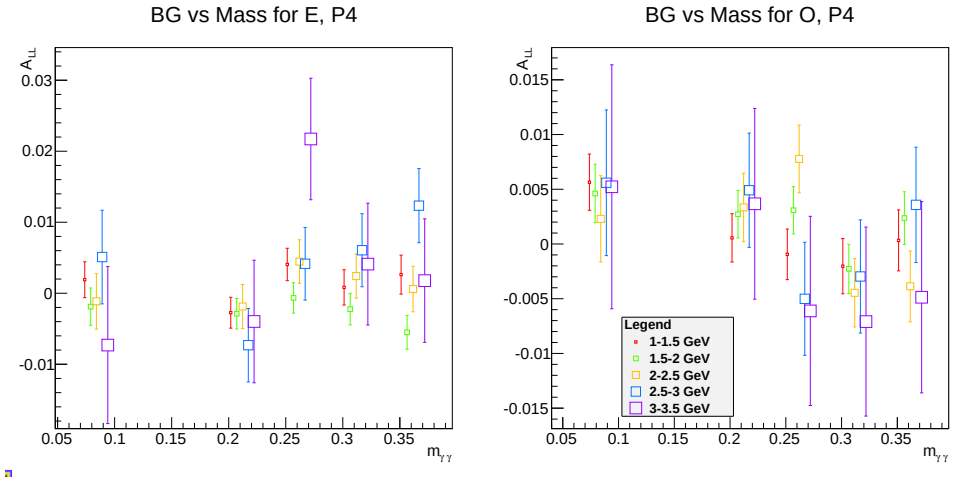

Figure A.8: BG A_{LL}'s mass for fill pattern 4 in *even* crossings (left) and *odd* crossings (right)

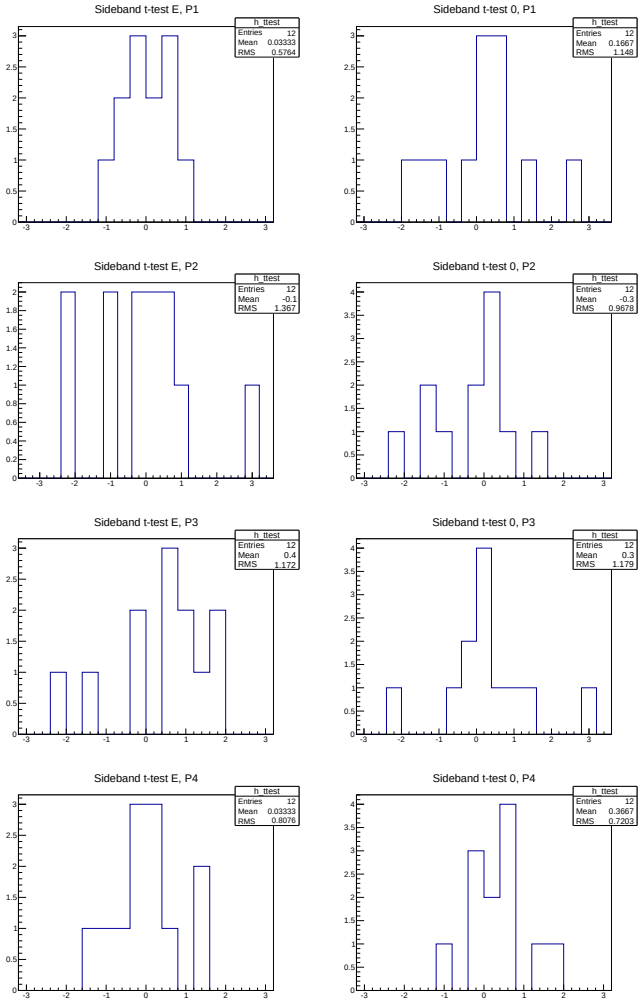

Figure A.9: Histograms of Student T-scores between background sidebands. There is one score for each p_T bin.

A.6 Plots of Background Asymmetry vs. p_T

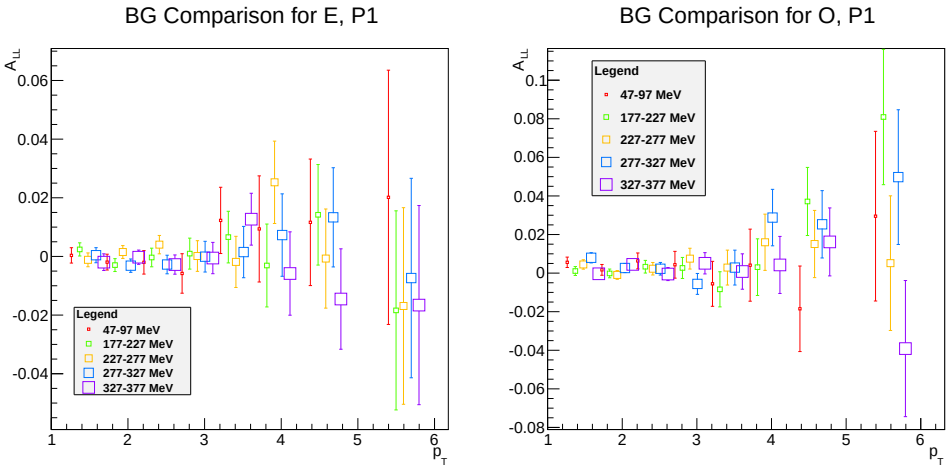

Figure A.10: BG A_{LL} p_T for fill pattern 1 in *even* crossings (left) and *odd* crossings (right)

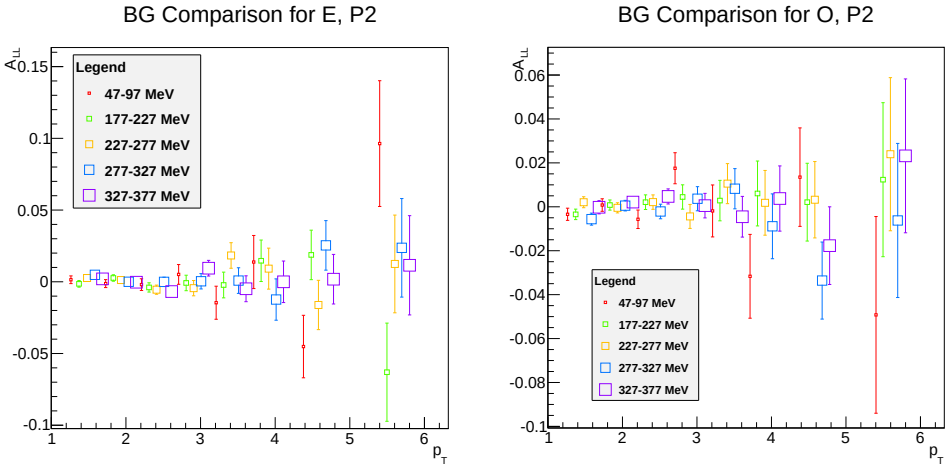

Figure A.11: BG A_{LL}'s p_T for fill pattern 2 in *even* crossings (left) and *odd* crossings (right)

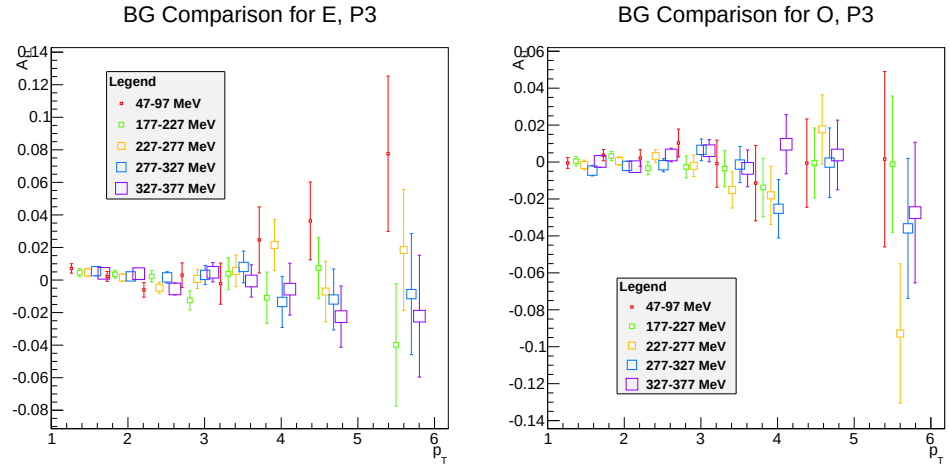

Figure A.12: BG A_{LL}'s p_T for fill pattern 3 in *even* crossings (left) and *odd* crossings (right)

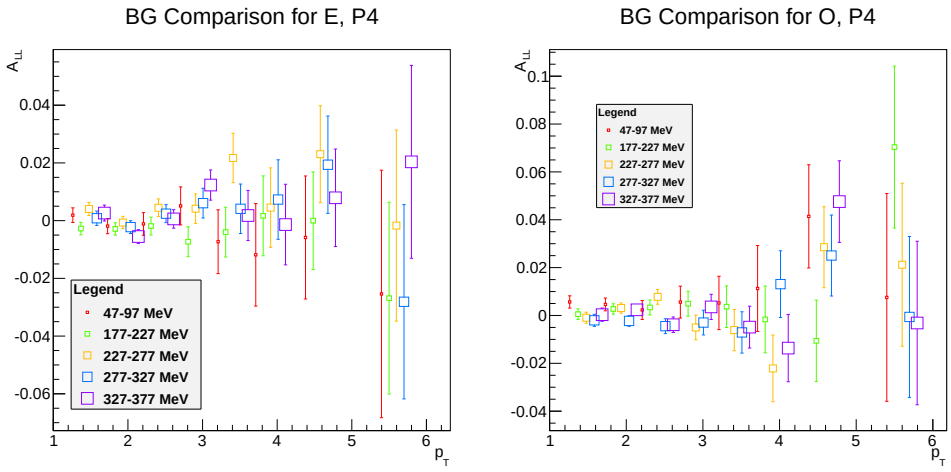

Figure A.13: BG A_{LL}'s p_T for fill pattern 4 in *even* crossings (left) and *odd* crossings (right)

Bibliography

[1] Adamczyk, L. et al. (2012). Phys. Rev. D, **86**, 032006.

[2] Adare, A. et al. (2007). Inclusive cross section and double helicity asymmetry for π^0 production in $p+p$ collisions at $\sqrt{s} = 200$ GeV: Implications for the polarized gluon distribution in the proton. Phys. Rev. D, **76**, 051106.

[3] Adare, A. et al. (2009a). Inclusive cross section and double helicity asymmetry for π^0 production in $p+p$ collisions at $\sqrt{s} = 62.4$ GeV. Phys. Rev. D, **79**, 012003.

[4] Adare, A. et al. (2009b). The Polarized gluon contribution to the proton spin from the double helicity asymmetry in inclusive pi0 production in polarized p + p collisions at s**(1/2) = 200-GeV. Phys.Rev.Lett., **103**, 012003.

[5] Adare, A. et al. (2011). Cross section and double helicity asymmetry for

$$\eta$$

$mesons and their comparison to \pi^0$ production in $p+p$ collisions at $\sqrt{s} = 200$ GeV. Phys. Rev. D, **83**, 032001.

[6] Adare, A. et al. (2012). Inclusive cross section and single-transverse-spin asymmetry for very forward neutron production in polarized $p+p$ collisions at $\sqrt{s} = 200$ GeV.

[7] Adare, A. et al. (2014). Inclusive double-helicity asymmetries in neutral pion and eta meson production in $\vec{p}+\vec{p}$ collisions at $\sqrt{s} = 200$ GeV.

[8] Adcox, K. et al. (2003). Phenix detector overview. Nucl. Instr. and Meth. Sec. A, **499**(23), 469 – 479.

[9] Adler, C. et al. (2003). The {RHIC} zero-degree calorimeters. Nuclear Instruments and Methods in Physics Research Section A: Accelerators,

Spectrometers, Detectors and Associated Equipment, **499**(23), 433 – 436. The Relativistic Heavy Ion Collider Project: {RHIC} and its Detectors.

[10] Adler, S. S. et al. (2007). Measurement of direct photon production in $p + p$ collisions at $\sqrt{s} = 200$ GeV. Phys. Rev. Lett., **98**, 012002.

[11] Alekseev, I. et al. (2006). Configuration manual, polarized proton collider at rhic.

[12] Allen, M. et al. (2003). {PHENIX} inner detectors. Nuclear Instruments and Methods in Physics Research Section A: Accelerators, Spectrometers, Detectors and Associated Equipment, **499**(23), 549 – 559. The Relativistic Heavy Ion Collider Project: {RHIC} and its Detectors.

[13] Anderson, W. et al. (2011). Design, construction, operation and performance of a hadron blind detector for the phenix experiment. Nucl. Instr. and Meth. Sec. A, **646**(1), 35 – 58.

[14] Antognini, A. et al. (2013). Proton structure from the measurement of 2s-2p transition frequencies of muonic hydrogen. Science, **339**(6118), 417–420.

[15] Aphecetche, L. et al. (2003). Phenix calorimeter. Nucl. Instr. and Meth. Sec. A, **499**(23), 521 – 536.

[16] Ashman, J. et al. (1989). An investigation of the spin structure of the proton in deep inelastic scattering of polarized muons on polarized protons. Nucl. Phys., **B328**, 1.

[17] Ball, R. D. et al. (2013a). Parton distributions with LHC data. Nucl.Phys., **B867**, 244–289.

[18] Ball, R. D. et al. (2013b). Unbiased determination of polarized parton distributions and their uncertainties. Nucl.Phys., **B874**, 36–84.

[19] Bargmann, V., Michel, L., and Telegdi, V. L. (1959). Precession of the polarization of particles moving in a homogeneous electromagnetic field. Phys. Rev. Lett., **2**, 435–436.

[20] Bazilevsky, A. et al. (2003). Results on double longitudinal spin asymmetry in π^0 production in polarized proton-proton collisions at $\sqrt{s} = 200$ gev from run-3. PHENIX analysis note, (AN277).

[21] Blümlein, J. and Böttcher, H. (2010). {QCD} analysis of polarized deep inelastic scattering data. Nuclear Physics B, **841**(12), 205 – 230.

[22] Bunce, G., Saito, N., Soffer, J., and Vogelsang, W. (2000). Prospects for spin physics at RHIC. Ann.Rev.Nucl.Part.Sci., **50**, 525–575.

[23] Buttimore, N. H. et al. (1999). Spin dependence of high energy proton scattering. Phys. Rev. D, **59**, 114010.

[24] Cameron, P. et al. (1995). Rhic beam position monitor characterization. In Particle Accelerator Conference, 1995., Proceedings of the 1995, volume 4, pages 2458–2460 vol.4.

[25] Cameron, P. et al. (1999). The rhic wall current monitor system. In Particle Accelerator Conference, 1999. Proceedings of the 1999, volume 3, pages 2146–2148 vol.3.

[26] Crawford, H. J. et al. (2004). The star scaler board, a 10 mhz 24-bit vme memory module.

[27] de Florian, D. et al. (2005). Sea quark and gluon polarization in the nucleon at nlo accuracy. Phys. Rev. D, **71**, 094018.

[28] de Florian, D., Sassot, R., and Stratmann, M. (2007). Global analysis of fragmentation functions for pions and kaons and their uncertainties. Phys. Rev. D, **75**, 114010.

[29] de Florian, D., Sassot, R., Stratmann, M., and Vogelsang, W. (2009). Extraction of spin-dependent parton densities and their uncertainties. Phys. Rev. D, **80**, 034030.

[30] de Florian, D., Sassot, R., Stratmann, M., and Vogelsang, W. (2014). Evidence for polarization of gluons in the proton.

[31] Djawotho, P. (2013). Gluon polarization and jet production at STAR.

[32] Drees, A. (2003). Cross Section Measurements using the Vernier Scan Technique during the RHIC d-Au Run. In APS Division of Nuclear Physics Meeting Abstracts, page H1.

[33] Ellis, J. R. and Jaffe, R. L. (1974). A sum rule for deep inelastic electroproduction from polarized protons. Phys. Rev., **D9**, 1444. Erratum-ibid.D10:1669,1974.

[34] Flauger, W. and Mönnig, F. (1976). Measurement of inclusive zero-angle neutron spectra at the {CERN} {ISR}. Nuclear Physics B, **109**(2), 347 – 356.

[35] Forck, P. et al. (2007). Beam position monitors.

[36] Gaillard, M. K. and Stora, R., editors (1983). Gauge theories in high energy physics. USMG NATO ASI Les Houches Session XXXVII 1981. C

[37] Glück, M. et al. (2001). Models for the polarized parton distributions of the nucleon. Phys. Rev. D, **63**, 094005.

[38] Group, R. P. (2012). Rhic polarizations for runs 9-12.

[39] Guidal, M. (2010). Generalized parton distributions from deep virtual compton scattering at {CLAS}. Physics Letters B, **689**(45), 156 – 162.

[40] Hirai, M. and Kumano, S. (2009). Determination of gluon polarization from deep inelastic scattering and collider data. Nuclear Physics B, **813**(12), 106 – 122.

[41] Huang, H. et al. (1999). A p-carbon cni polarimeter for rhic. In Particle Accelerator Conference, 1999. Proceedings of the 1999, volume 1, pages 471–473 vol.1.

[42] Jaffe, R. and Manohar, A. (1990). The g1 problem: Deep inelastic electron scattering and the spin of the proton. Nuclear Physics B, **337**(3), 509 – 546.

[43] Jäger, B., Schäfer, A., Stratmann, M., and Vogelsang, W. (2003). Next-to-leading order qcd corrections to high-p_T pion production in longitudinally polarized pp collisions. Phys. Rev. D, **67**, 054005.

[44] K., A. et al. (2003). Phenix central arm tracking detectors. Nucl. Instr. and Meth. Sec. A, **499**(23), 489–507.

[45] Kline, P. et al. (2009). Relative luminosity in run9 longitudinally polarized p+p at $\sqrt{s} = 200$ gev. PHENIX analysis note, (AN881).

[46] Kumerički, K. and Müller, D. (2010). Deeply virtual compton scattering at small and the access to the {GPD} h. Nuclear Physics B, **841**(12), 1 – 58.

[47] Leader, E. et al. (2010). Determination of polarized parton densities from a qcd analysis of inclusive and semi-inclusive deep inelastic scattering data. Phys. Rev. D, **82**, 114018.

[48] Moore, C. et al. (1989). Single bunch intensity monitoring system using an improved wall current monitor. In Particle Accelerator Conference, 1989. Accelerator Science and Technology., Proceedings of the 1989 IEEE, pages 1513–1515 vol.3.

[49] Nilsson, P. (2001). Pad chamber hit reconstruction.

[50] Nocera, E. R. (2013). Constraints on polarized parton distributions from open charm and W production data.

[51] Okada, H. (2006). Measurement of the Analyzing Power A_N in pp Elastic Scattering in the CNI Region with a Polarized Atomic Hydrogen Gas Jet Target. Ph.D. thesis, Kyoto University.

[52] Owens, J. F., Accardi, A., and Melnitchouk, W. (2013). Global parton distributions with nuclear and finite-¡span class="aps-inline-formula"¿¡math display="inline"¿¡msup¿¡mi¿q¡/mi¿¡mn¿2¡/mn¿¡/msup¿¡/math¿¡/span¿ corrections. Phys. Rev. D, **87**, 094012.

[53] Poblaguev, A. (2013). The polarized hydrogen jet target measurements at rhic.

[54] Pumplin, J. et al. (2002). New generation of parton distributions with uncertainties from global QCD analysis. JHEP, **0207**, 012.

[55] Roser, T. et al. (2002q). Accelerating and colliding polarized protons in rhic with siberian snakes. In Proceedings of EPAC 2002, Paris, France.

[56] Sehgal, L. M. (1974). Angular momentum composition of the proton in the quark parton model. Phys. Rev., **D10**, 1663.

[57] Stevens, J. R. (2013). The star w program at rhic. Il Nuovo Cimento C, **36**, 39.

[58] Togawa, M. (2008). Measurements of the leading neutron production in polarized pp collision at $\sqrt{s} = 200$ GeV. Ph.D. thesis, Kyoto Univ.

[59] Vogt, A. (2005). Efficient evolution of unpolarized and polarized parton distributions with qcd-pegasus. Comput.Phys.Commun., **170**, 65–92.

[60] Webber, R. C. (1990). Longitudinal emittance: An introduction to the concept and survey of measurement techniques including design of a wall current monitor. AIP Conference Proceedings, **212**(1), 85–126.

[61] Zelenski, A. et al. (2005). Absolute polarized h-jet polarimeter development, for {RHIC}. Nuclear Instruments and Methods in Physics Research Section A: Accelerators, Spectrometers, Detectors and Associated Equipment, **536**(3), 248 – 254. Polarized Sources and Targets for the 21st Century. Proceedings o f the 10th International Workshop on Polarized Sources and Targets.